Book of Abstracts

Advanced Properties and Processes in
Optoelectronic Materials and Systems
Apropos 17
30 September – 01 October, 2020
Vilnius, Lithuania

Lithuania-Poland Workshop
on Physics and Technology

Vilnius, 2020

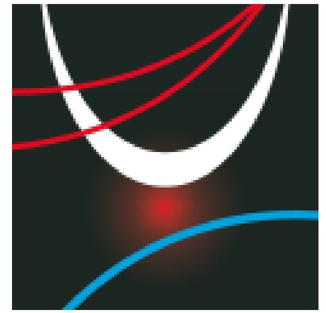

Apropos 17

Advanced Properties and Processes in
Optoelectronic Materials and Systems
30 September – 01 October, 2020
Vilnius, Lithuania

Sattelite Event

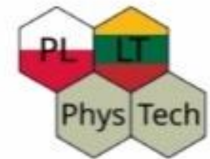

Lithuania-Poland Workshop

on Physics and Technology

ISBN 978-609-95511-7-3

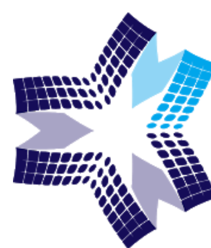

CENTER
FOR PHYSICAL SCIENCES
AND TECHNOLOGY

© Center for Physical Sciences and Technology, 2020

Savanorių ave. 231, LT-02300 Vilnius, Lithuania
http://apropos.ftmc.lt
apropos@ftmc.lt

Contents

Committees 4

Welcome Address 5

Programme 9

List of poster presentations 13

Oral presentations 14

Poster presentations 51

Author index 88

Committees

CHAIR

Gintaras Valušis, *Vilnius, Lithuania*

PROGRAMME COMMITTEE

Vidmantas Gulbinas, *Vilnius, Lithuania*
Saulius Juršėnas, *Vilnius, Lithuania*
Andriy Kadashchuk, *Kiev, Ukraine*
Jacek Kossut, *Warsaw, Poland*
Wojciech Knap, *Montpellier, France*
Arūnas Krotkus, *Vilnius, Lithuania*
Polina Kuzhir, *Minsk, Belarus*
Edmund H. Linfield, *Leeds, U.K.*
Valdas Pašiškevičius, *Stockholm, Sweden*
Carlito S. Ponseca *Linköping, Sweden*
Hartmut G. Roskos, *Frankfurt/M, Germany*
Chiko Otani, *Sendai, Japan*
Gediminas Račiukaitis, *Vilnius, Lithuania*
Roman Sobolewski *Rochester, NY, USA*
Sigitas Tamulevičius, *Kaunas, Lithuania*
Gintautas Tamulaitis, *Vilnius, Lithuania*

LOCAL ORGANIZING COMMITTEE

Renata Butkutė (Secretary)
Domas Jokubauskis
Renata Karpicz
Ramunė Kriaučionytė
Rimgaudas Žaliauskas
Evaldas Tornau
Marius Vinciūnas
Milda Tamošiūnaitė-Survilienė

Welcome Address

The Conference continues tradition to bring together scientists involved in research focused on solid state physics and photonics.

The conference has started as a symposium entitled “Plasma and instabilities” held every three years in Vilnius since 1971. The event was initiated and hosted by the Semiconductor Physics Institute. After Lithuania regained its Independence in 1990, the Symposium was transformed into “International Symposium on Ultrafast Phenomena in Semiconductors (UFPS), Vilnius, Lithuania”.

In 2010 the Semiconductor Physics Institute became a part of the Center for Physical Sciences and Technology. The year of 2016 highlighted particular changes in the Center – the institution moved to a new building located in Saulėtekis (Sunrise) avenue. Modern technological and scientific laboratories opened novel facilities for science and innovations. Therefore, the conference also gained new scientific dimension and new name – “**Advanced Properties and Processes in Optoelectronic Materials and Systems**”, **APROPOS**.

APROPOS 17 manifests optoelectronics and nanotechnology – based scope covering topics of

- Semiconductor nanostructures and advanced photonics systems,
- Organic materials for optoelectronics,
- Ultrafast and terahertz phenomena,
- Laser technologies & light emitting diodes,
- Nano- and biophotonics.

This year APROPOS conference will be coupled with the Jubilee Conference “10 years of scientific excellence and high-tech-innovations” dedicated to the first significant milestone – the 10 Year Anniversary of the Center for Physical Sciences and Technology (FTMC).

Prof.Dr. Hab. Gintaras Valušis

Chair of the APROPOS 17

Ladies and Gentelmen,

I am very happy to note that the Lithuania - Poland collaboration develops and this workshop is a clear signature of this fact. Thank to efforts of our governments, national and European financing we managed to establish world - class technological centers which serve countries on scientific, industrial and educational levels. We highly appreciate the idea of our national financing agencies to establish a common scientific program Daina which is developing well and brings common benefits. I think that the next good step would be lounching a scholarship program for students and young researchers who could travel between laboratories, exchange ideas, learn and make our efforts more complementary.

I wish you a fruitful and successfull conference and I hope that this meeting will bring you a great scientific satisfaction.

Prof.Dr. Hab. Jerzy Łusakowski
Chair from Poland of Lithuania-Poland Workshop on Physics and Technology

Gerbiamas Pirmininke, gerbiami profesoriai, mokslininkai, gerbiamieji svečiai,

Man garbė atidaryti dar vienas Lietuvos-Lenkijos fizikos ir technologijų dirbtuves. Kai prieš metus, kartu su Lietuvos užsienio reikalų viceministru Neriu Germanu, susitikome dirbtuvių atidarymo renginyje Valdovų rūmuose, nemanėme, kad po kelių mėnesių patirsime COVID-19 pandemiją, kuri pakeis mūsų bendravimo būdą. Tuo labiau džiugu, kad, nepaisant sunkumų, jums pavyko surengti tiek „Apropos“ konferenciją – padėkos žodžiai Fizinių ir technologijos mokslų centrui – tiek Lenkijos ir Lietuvos dirbtuves jos metu.

Šie keli žodžiai, kuriuos galiu jums pasakyti, tai taip pat yra proga priminti apie didžiulį socialinį mokslininkų vaidmenį ir atsakomybę, nes šiais laikais jie dažnai yra kviečiami prie lentos ir privalo viešai ginti mokslo pasiekimus nuo iracionalaus puolimo. COVID-19 pandemija buvo puiki galimybė skleisti dezinformaciją, o Jūs ir Jūsų kolegos dažnai stojote priešakyje kovoje su koronavirusu ir jo poveikiu sveikatai bei socialinėmis pasekmėmis.

Verta pabrėžti, kad Lenkijos ir Lietuvos santykiai pastaruoju metu klesti. Jūsų susitikimas yra vienas iš to įrodymų. Todėl džiaugiuosi, kad šiemet Jums pavyko įgyvendinti dar vieną Nacionalinio mokslo centro ir „Research Council of Lithuania DAINA 2“ programą, kurioje Lenkijos ir Lietuvos mokslininkai gali suvienyti jėgas bendroje mokslinėje veikloje. Programa buvo sutikta su dideliu susidomėjimu ir esu įsitikinusi, kad mūsų šalių bendradarbiavimas – tiek humanitarinių, tiek fizikos mokslų, tiek socialinių mokslų srityje – bus naudingas abiem pusėms ir sustiprins Lenkijos ir Lietuvos mokslininkų ryšių tinklą.

Dar kartą dėkoju už kvietimą ir linkiu įdomių bei naudingų diskusijų.

Urszula Doroszewska

Ambassador, Embassy of Poland

Szanowny Panie Przewodniczący, szanowni profesorowie, naukowcy, drodzy Państwo,

Mam zaszczyt otworzyć kolejne Polsko-Litewskie Warsztaty Fizyczne i Technologiczne. Kiedy rok temu spotkaliśmy się w Pałacu Wielkich Książąt na otwarciu poprzedniej edycji, wraz z wiceministrem spraw zagranicznych Litwy Nerisem Germanasem, nie sądziliśmy, że już za kilka miesięcy doświadczymy pandemii Covid-19, która zmieni nasz sposób komunikacji. Tym bardziej cieszy, że mimo przeciwności, udało się jednak zorganizować zarówno konferencję Apropos – za co należą się gratulacje Centrum Nauk Fizycznych i Technologii – jak i polsko-litewski panel w jej ramach.

Te kilka słów, które mogę skierować do Państwa to także okazja, aby przypomnieć o ogromnej roli społecznej i odpowiedzialności naukowców, którzy w dzisiejszych czasach nierzadko są wywoływani

do tablicy i muszą publicznie bronić osiągnięć nauki przed ofensywą irracjonalności. Pandemia Covid-19 była doskonałą okazją dla działań dezinformacyjnych i to właśnie Państwo i Państwa koleżanki i koledzy nierzadko stawali na pierwszej linii walki z koronawirusem i jego konsekwencjami zdrowotnymi i społecznymi.

Warto podkreślić, że stosunki polsko-litewskie przeżywają w ostatnich czasach duży rozkwit. Państwa spotkanie jest na to jednym z dowodów. Dlatego niezmiernie cieszy mnie, że w tym roku udało się uruchomić kolejną edycję programu Narodowego Centrum Nauki i Research Council of Lithuania DAINA 2, w którym polscy i litewscy naukowcy mogą połączyć siły we wspólnych przedsięwzięciach naukowych. Program cieszy się dużym zainteresowaniem i jestem przekonana, że współpraca między naszymi krajami – czy to w naukach humanistycznych czy fizycznych, czy o życiu, przyniesie korzyści obu stronom i umocni sieci kontaktów między naukowcami Polski i Litwy.

Dziękuję raz jeszcze za zaproszenie i życzę Państwu owocnych obrad.

CONFERENCE PROGRAMME

Center for Physical Sciences and Technology (FTMC), Vilnius, Lithuania
Venue: FTMC at Sunrise Valley, Saulėtekio Ave. 3, Vilnius, Lithuania

30 September		
8:00-9:00		REGISTRATION
9:00-9:15		**CONFERENCE OPENING CEREMONY** **Gintaras Valušis** Director of Center for Physical Sciences and Technology Chair of Apropos 17 conference
9:15-10:35		**Section 1: Semiconductor nanostructures and advanced photonics systems** **Chair Prof.** ***Carlito Jr.Salonga Ponseca***
9:15-9:45	**Inv 1**	**Linas Minkevičius** *(Center for Physical Sciences and Technology, Vilnius, Lithuania)* Review of innovative diffractive elements for Terahertz imaging applications
9:45-10:15	**Inv2**	**Ramūnas Aleksiejūnas** *(Vilnius University, Lithuania)* Impact of alloy disorder induced localization on hole diffusion in highly excited c-plane and m-plane InGaN quantum wells
10:15-10:35	O1	Janusz Sadowski (*University of Warsaw, Institute of Physics, Warsaw, Poland, Linnaeus University, Sweden)* MoTe2 transition metal dichalcogenide grown by molecular beam epitaxy – polytypes, structural and electrical properties
10:35-11:00		**Coffee break**
11:00-13:00		**Section 2: Nano and Biophotonics** **Chair Dr.** ***Kaibo Zheng***
11:00-11:30	**Inv3**	**Šarūnas Meškinis** *(Kaunas University of Technology, Lithuania)* Direct synthesis of the graphene on Si(100) substrate for solar cell applications
11:30-12:00	**Inv4**	**Dovydas Banevičius** *(Vilnius University, Lithuania)* Naphthyridine-based deep-blue TADF OLEDs with low efficiency roll-off
12:00-12:20	O2	Rusnė Ivaškevičiūtė-Povilauskienė *(Center for Physical Sciences and Technology, Vilnius, Lithuania)* All-optical modulation of graphene layers
12:20-12:40	O3	Lena Golubewa *(Center for Physical Sciences and Technology, Vilnius, Lithuania)* Raman spectroscopic investigation of multi-walled carbon nanotubes mediated neutrophil activation
12:40-13:00	O4	Adil Rehman (*Institute of High Pressure Physics, Warsaw, Poland*) Modulation of electrical and noise characteristics of carbon nanotubes based devices
13:00-14:00		**Lunch**
14:00-15:50		***Special session:*** **Ultrafast THz techniques** **Chair Dr.** ***Ignas Grigelionis***

14:00-14:30	**Inv5**	**Carlito S. Ponseca, Jr.** (*Linköping University, Sweden*) - Ultrafast transient spectroscopy of organic and hybrid solar cells
14:30-14:50	O5	Kaibo Zheng (*Lund University, Sweden, Technical University of Denmark, Danmark)* Ultrafast spectroscopy of Quantum dot solar cells
14:50-15:10	O6	Ričardas Norkus *(Center for Physical Sciences and Technology, Vilnius, Lithuania)* Terahertz emission from a bulk GaSe crystal excited by above-bandgap photons
15:10-15:30	O7	Daniil Pashnev *(Center for Physical Sciences and Technology, Vilnius, Lithuania)* Investigation of two-dimensional plasma resonances in grating-gated AlGaN/GaN heterostructures by terahertz time domain spectroscopy
15:30-15:50	O8	Marek Maciaszek (*University of Warsaw, Poland)* On the origin of the 4.1 eV luminescence in hexagonal boron nitride
15:50-16:15		**Coffee break**
16:15-18:20		**Section 1: Semiconductor nanostructures and advanced photonics systems** **Chair Prof. *Šarūnas Meškinis***
16:15-16:45	**Inv6**	**Tadas Malinauskas** *(Vilnius University, Lithuania)* Remote epitaxy of GaN via Graphene
16:45-17:05	O9	Ivan Yahniuk (*Institute of High Pressure Physics, Warsaw, Poland*) Temperature-& Pressure-induced transitions in HgTe QWs
17:05-17:20	O10	Roman M. Balagula *(Center for Physical Sciences and Technology, Vilnius, Lithuania)* Annealing-induced reduction of strain in GaAs/GaNAs core-shell nanowires
17:20-17:40	O11	Andrea Zelioli *(University of Modena, Italia)* GaInAs/GaAs Quantum Structures For Near Infrared Vertical-External-Cavity Surface-Emitting Lasers
17:40-18:00	O12	Simona Pūkienė *(Center for Physical Sciences and Technology, Vilnius, Lithuania)* A3-B5 QW structures for IR range optoelectronic devices
18:00-19:30		**Poster session (18 posters)** **Coffee and Snaps**

1 October		
9:00-11:00		***Satellite Event:* Lithuanian Polish Workshop** **Chair Prof. *Janusz Sadowski***
9:00-9:10		**WORKSHOP OPENING CEREMONY** Ambassador Urszula Doroszewska, Embassy of Poland Jerzy Łusakowski (Chair from Poland)
9:10-9:35	**Inv7**	**Nerija Žurauskienė** *(Center for Physical Sciences and Technology, Vilnius, Lithuania)* Magnetoresistance Relaxation Phenomena in Nanostructured Lanthanum Manganite Films
9:35-10:00	**Inv8**	**Wojciech Pacuski** (*University of Warsaw, Poland)* Narrow excitonic lines and large-scale homogeneity of transition metal dichalcogenides grown by MBE on hBN
10:00-10:20	O13	Maksym Dub (*Institute of High Pressure Physics, Warsaw, Poland*) Graphene gate GaN/AlGaN field effects transistors for THz detection
10:20-10:40	O14	Maria Szoła (*Institute of High Pressure Physics, Warsaw, Poland*) THz magnetospectroscopy of HgCdTe bulk crystals with different Cd content
10:40-11:00	O15	Paweł Komorowski (*Warsaw University of Technology, Poland*) Machine learning enhanced design of diffractive optical elements
11:00-11:25		**Coffee break**
11:25-13:05		**Section 3: Ultrafast and THz phenomena** **Chair Dr. *Linas Minkevičius***
11:25-11:55	**Inv9**	**Alvydas Lisauskas** (*Vilnius University and Institute of High Pressure Physics, Warsaw, Poland)* THz detectors and sources fabricated with CMOS technologies
11:55-12:25	**Inv10**	**Guillaume Ducournau** *(Université Lille, France)* THz communications and advanced RF characterization enabled by THz photonics
12:25-12:45	O16	Dmytro B. But (*Institute of High Pressure Physics, Warsaw, Poland*) Antenna Characterization of Monolithically Integrated Detectors for 0.62 THz
12:45-13:05	O17	Domas Jokubauskis *(Center for Physical Sciences and Technology, Vilnius, Lithuania)* Phase contrast sub THz imaging and applications
13:05-14:00		**Lunch**
14:00-15:50		**Section 3: Ultrafast and THz phenomena** **Chair Prof. *Alvydas Lisauskas***
14:00-14:30	Inv11	**Vincas Tamošiūnas** *(Center for Physical Sciences and Technology, Vilnius, Vilnius University, Lithuania)* Reflectance spectra of selective emitter solar cells in terahertz and sub-terahertz ranges
14:30-14:50	O18	Dmitri V. Lioubtchenko (*KTH Royal Institute of Technology, Stockholm, Sweden)* Effect of lengths, diameters, and density of silver nanowire layers on terahertz conductivity

14:50-15:10	O19	Ieva Žičkienė *(Center for Physical Sciences and Technology, Vilnius, Lithuania)* Terahertz radiation induced by surface ballistic photogalvanic effect in GaAs LIPSS structures
15:10-15:30	O20	Pavlo Sai (*Institute of High Pressure Physics, Warsaw, Warsaw University of Technology, Poland*) AlGaN/GaN dual grating gate structures investigated in high magnetic field
15:30-15:50	O21	Vladislovas Čižas *(Center for Physical Sciences and Technology, Vilnius, Lithuania)* Fractional frequencies in microwave response of GaAs/AlGaAs superlattices
15:50-16:15		**Coffee break**
16:15-17:35		**Section 4: Organics for Optoelectronics** **Chair Dr. Prof. *Nerija Žurauskienė***
16:15-16:35	O22	**Yuri Svirko** *(University of Eastern Finland, Joensuu, Finland)* Light-induced currents and THz emission from graphene
16:35-16:55	O23	Ernesta Poceviciute *(Center for Physical Sciences and Technology, Vilnius, Lithuania)* Studies of Receptor and Its Ligand Interaction Using FRET and TIRF Microscopy
16:55-17:15	O24	Edvinas Navakauskas *(Center for Physical Sciences and Technology, Vilnius, Lithuania)* Structure determination of HEWL protein aggregates at liquid interfaces
17:15-17:35	O25	Wanessa Melo *(Center for Physical Sciences and Technology, Vilnius, Lithuania)* Antimicrobial photodynamic therapy: an alternative to overcome the biofilm resistance
17:40		**Closing Remarks**

List of posters

P1 Algirdas Jasinskas Optically pumped semiconductor lasers based on InGaAs/GaAs and GaAsBi/GaAs quantum wells

P2 Jonas Gradauskas Three components of photovoltage simultaneously induced across GaAs p-n junction

P3 Karolis Stašys Bismide-based Intersubband devices for Mid-Infrared Applications

P4 Linas Ardaravičius Determination of electron drift velocity from hot-electron effect in ZnO epilayers and AlGaN/GaN heterostructures

P5 Roman Balagula Optical properties of GeSi/Si quantum dots in mid- and far-IR range

P6 Agnė Zdaniauskienė In-situ SHINERS analysis of SAM from thiols with imidazole ring and intrachain amide groups

P7 Karolina Maleckaitė Polarity sensors based on thiophene-substituted BODIPY molecular rotors

P8 Rokas Gegevičius Energy Barriers in MAPbI3 Perovskite Films

P9 Rokas Jasiunas Benefits of MAPbI3 perovskite doping by Sr2+

P10 Rugilė Lukaševičiūtė Activity measurements of GMC superfamily flavoenzymes using Amplex Red assay

P11 Šarūnas Jankauskas Structural defect behavior of thermally annealed graphene, directly synthesized on Si(100) substrate using MW-PECVD

P12 Vaidas Pudžaitis In-situ probing of SAM and tBLM layer formation on nanostructured gold by ATR-SEIRAS

P13 Andrius Kamarauskas Impact of thin low specific conductivity layer on Fano resonance amplitude in an array of split ring resonators

P14 Ieva Matulaitienė Black silicon based substrates for surface enhanced Raman spectroscopy

P15 Ivan Yahniuk Terahertz detection and noise properties of (Cd1-xZnx)3As2

P16 Juozas Vyšniauskas Enhanced sensitivity AlGaN/GaN HEMT terahertz detector without ungated regions

P17 Liang Qi Performance of Titanium-based Microbolometers for Monitoring of Spatial Beam Profile in Terahertz Time-Domain Systems

P18 Paulius Mackonis Laser system for pumping THz and coherent X-ray sources of secondary radiation

Oral presentations

Inv1

Review of innovative diffractive elements for Terahertz imaging applications

Linas Minkevičius[1], Domas Jokubauskis[1], Simonas Indrišiūnas[1], Vincas Tamošiūnas[1, 2], Sergej Orlov[1], Irmantas Kašalynas[1], Gediminas Račiukaitis[1] and Gintaras Valušis[1]

[1] Department of Optoelectronics, Center for Physical Sciences and Technology, Saulėtekio av. 3, LT-10257 Vilnius, Lithuania
[2] Institute of Photonics and Nanotechnology, Vilnius University, Saulėtekio av. 3, LT-10257 Vilnius, Lithuania.
Email: linas.minkevicius@ftmc.lt

Miniaturization of terahertz (THz) imaging systems is a key-factor for increasing applicability in mobile unattended package inspection systems in airports or public places [1]. Practical potential of THz imaging systems for non-destructive testing encourage a search for a compact and practically convenient solutions. One of the most lucrative solutions is the development of compact diffractive optics for the THz frequency range in order to boost the evolution of practical hand-held terahertz imaging systems applications in real time.

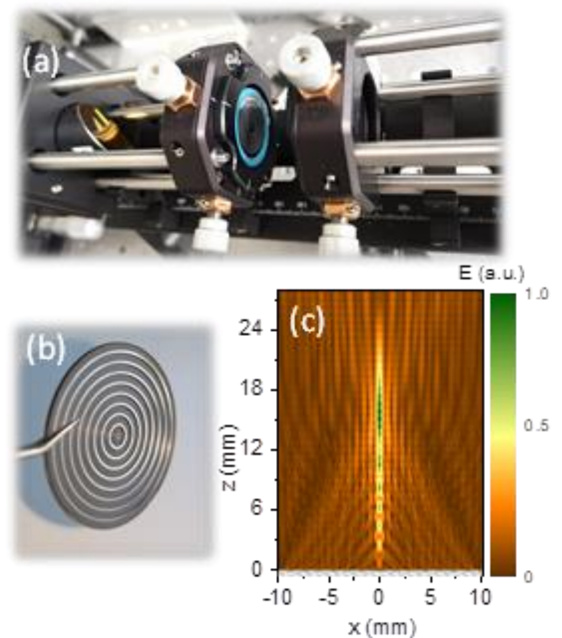

Fig. 1 The photo of innovative terahertz imaging system (a) containing thin silicon-based Bessel zone plates (b) for the 0.6 THz. Bessel beam electric field reconstruction at 0.6 THz along the beam propagation path.

In a given communication, variety solutions of compact diffractive optics, produced with laser direct writing technology [2] are considered. Molybdenum film-based THz zone plates with integrated band-pass filters [3], high efficiency multilevel silicon phase Fresnel zone plates [4] for advanced THz optics up to 4.7 THz [5], are discussed. Focusing performance of these elements are investigated both, theoretically and experimentally. Routes of thick objects THz imaging with inconvenience of precise positioning of the sample using silicon-based Fibonacci [6] and Bessel diffractive elements [7] providing a 2×λ spatial resolution will be also discussed (Fig. 1).

REFERENCES

[1].X. Yang et al. Signal Processing, **160** (2019) pp.202–214.
[2].B. Voisiat et al. *Proc. of SPIE*, (2017) **10091**(10 1117/12.2253634) pp. 100910F
[3].L. Minkevičius et al. *J. Infrared, Millimeter, Terahertz Waves* **35**(9) (2014) pp. 699-702
[4] L. Minkevičius et al, *Optics Letters* **42**(10) (2017) pp. 1875-1878
[5].S. Indrisiunas et al. *Optics Letters* **44**(5) (2019) pp. 1210-1213
[6] D. Jokubauskis et al *Optics Letters* **43**(12) (2018) pp. 2795-2798
[7] L. Minkevičius et al. Optics. Express **27**(25) (2019) pp. 36358

Inv2

Impact of alloy disorder induced localization on hole diffusion in highly excited c-plane and m-plane InGaN quantum wells

Ramūnas Aleksiejūnas,[1] Kazimieras Nomeika,[1] Oleg Kravcov,[1] Saulius Nargelas,[1] Leah Kuritzky,[2] Cheyenne Lynsky,[2] Shuji Nakamura,[2] Claude Weisbuch,[2,3] and James S. Speck[2]

[1] *Vilnius University, Institute of Photonics and Nanotechnology, Saulėtekio Ave. 3, LT-10257, Vilnius, Lithuania*

[2] *Materials Department, University of California, Santa Barbara, California 93106, United States*

[3] *Laboratoire de Physique de la Matie`re Condense´e, Ecole Polytechnique, CNRS, IP Paris, 91128 Palaiseau Cedex, France*

Email: ramunas.aleksiejunas@ff.vu.lt

A mystery remains how internal quantum efficiency of InGaN can reach 90% despite a typical dislocation density exceeding 10^8 cm^{-2} [1]. It was proposed that this may be due to carrier localization [2]; however, the detailed mechanism of this phenomenon remains undisclosed. Since holes are strongly localized in InGaN [3], new knowledge may be attained by measuring their diffusion coefficient, *D*. Here, we investigate the dependence of *D* on direction and carrier density in c-plane and m-plane InGaN structures by employing the light-induced transient grating technique. We show that *D* is anisotropic in the m-plane structures due to hole effective mass anisotropy in biaxially strained layers. Also, *D* changes non-monotonously with photoexcitation (Fig. 1), this dependence being different in thick and thin layers. We argue that unexpectedly high diffusion coefficient at low carrier densities in thick QWs can be a signature of efficient hole transport via percolative paths occurring due to compositional disorder. In turn, a decrease of diffusivity with excitation can reflect the effect of Coulomb blockade of these paths. Finally, we demonstrate that disorder impacts carrier diffusivity even at carrier densities above 10^{19} cm^{-3}, where the overflow of localized states must be included to explain the observed increase of diffusion coefficient with carrier density.

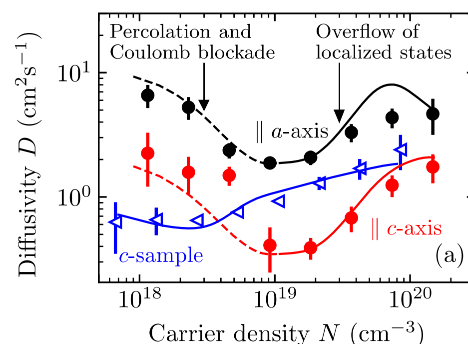

Fig. 1. The dependence of diffusion coefficient *D* on carrier density *N* in thick m-plane and thin c-plane MQW structures

REFERENCES

[1] C. Weisbuch, ECS J. Solid State Sci. Technol. 9, 016022 (2019).
[2] S. Chichibu, T. Azuhata, T. Sota, and S. Nakamura, Applied Physics Letters 69, 4188 (1996).
[3] S. Schulz, M. A. Caro, C. Coughlan, and E. P. O'Reilly, Physical Review B 91, 035439 (2015).

O1

$MoTe_2$ transition metal dichalcogenide grown by molecular beam epitaxy – polytypes, structural and electrical properties

Janusz Sadowski[1,2,3], Bartłomiej Seredyński[1], Zuzanna Ogorzałek[1], Sławomir Kret[2], Rafał Bożek[1], Marta Gryglas-Borysiewicz[1] and Wojciech Pacuski[1]

[1] *Faculty of Physics, University of Warsaw, Pasteura 5, 02-093 Warsaw, Poland.*
[2] *Institute of Physics, Polish Academy of Sciences, Aleja Lotników 32/46, 02-668 Warsaw, Poland.*
[3] *Department of Physics and Electrical Engineering, Linnaeus University, 391 82, Kalmar, Sweden.*
Email: Janusz.sadowski@fuw.edu.pl

$MoTe_2$ belongs to layered transition metal dichalcogenides (TMD) which, due to their unique optoelectronic properties, gained a tremendous attention of condensed matter research community over the last few years [1]. Excellent optical properties of single molecular layers of semiconducting TMDs, makes them suitable for applications in flexible optoelectronics. The high sensitivity of electric properties of ultra-thin layers of semiconducting and metallic TMDs to external factors such as electrical gating, pressure, chemical environment enables their use for numerous applications. Constantly new TMD materials are synthesized and extensively investigated [2].

Fig.1. Cross-sectional transmission electron microscopy images of AlO_x capped $MoTe_2$ bilayer grown by MBE on GaAs(111B) substrate.

Here we report on the growth of $MoTe_2$ - a representative of semiconducting, (metallic) TMD (depending on the crystallographic phase). We have grown thin MoTe2 layers by molecular beam epitaxy (MBE) - a technique, widely used both for research purposes and in the optoelectronic industry. MBE enables growth on large area substrates – up to 3-inches in our case. The growth proceeds in ultra-clean ultrahigh vacuum environment and is controlled in-situ with reflection high energy electron diffraction (RHEED). In contrast to other TMD materials $MoTe_2$ is quite sensitive to oxidation on exposure to ambient conditions. We show how to protect very thin $MoTe_2$ films (bilayers) against degradation by in-situ deposition of thin capping layers. Using this method we obtain large area ultrathin $MoTe_2$ layers (monolayers, bilayers) stable in air [3]. We have investigated structural and electrical properties of $MoTe_2$ bilayers MBE-grown on GaAs(111)B substrates and capped with thin (~5 nm) AlO_x (see Fig.1).

REFERENCES

[1] W. Choi, N. Choudhary, G. H. Han, J. Park, D. Akinwande and Y. H. Lee; *Mat. Today* **20** (2017) p. 116.
[2] Xiao Zhang, Zhuangchai Lai, Qinglang Ma and Hua Zhang; *Chem. Soc. Rev.* **47** (2018) pp. 3301-3338.
[3] Z. Ogorzałek, B. Seredyński, S. Kret, A. Kwiatkowski, K. P. Korona, M. Grzeszczyk, J. Mierzejewski, D. Wasik, W. Pacuski, J. Sadowski and M. Gryglas-Borysiewicz. *Nanoscale* **12**, (2020) pp.16535-16542.

Inv3

Direct synthesis of the graphene on Si(100) substrate for solar cell applications

Rimantas Gudaitis, Andrius Vasiliauskas, Asta Guobienė, Šarūnas Jankauskas, Šarūnas Meškinis

[1] *Institute of Materials Science of Kaunas University of Technology, Baršausko 59, Kaunas, Lithuania*

Email: sarunas.meskinis@ktu.lt

2D nanomaterial graphene is at the top of the considerable interest due to the giant electron and hole mobility, charge carrier multiplication, flexibility, optical transparency, chemical inertness. Graphene is already considered as a new transparent conductor, monolayer alternative to the Schottky contact metals and even as an active layer of the semiconductor devices. Particularly graphene is intensively explored as a new photovoltaic material for the fabrication of the various solar cells. The list is pretty long: monocrystalline silicon, inorganic chalcogenide thin film, organic, perovskite, dye sensitized solar cells can be mentioned.

One of the main limitations stopping the wider application of the graphene in semiconductor device technology is a complex graphene transfer procedure. In this case, graphene is synthesized on the catalytic Cu or Ni foils. Afterward, follows the long process of the graphene transfer onto the targeted semiconductor or dielectric substrates. During that process, graphene can be contaminated by different adsorbents. Transfer causes wrinkles or ripples to form on graphene. In such a case control of the graphene layer or graphene-semiconductor contact properties is complicated. Recently there were shown that direct synthesis of the graphene on semiconducting or dielectric substrates is possible. However, the development of this technology is the very beginning.

In the present research graphene layers were directly synthesized by microwave plasma enhanced chemical vapor deposition on the semiconducting monocrystalline Si(100) substrates. The structure of the films was investigated by Raman scattering spectroscopy and atomic force microscopy. A number of the graphene layers was evaluated by using Raman scattering spectroscopy and optical reflectance spectra. Graphene/Si(100) Schottky diodes were fabricated.

The effects of the deposition conditions on the structure of the graphene layers were studied. The influence of the nitrogen and fluorene doping was considered. There were revealed that both vertical graphene flakes and planar graphene layers can be synthesized by setting appropriate deposition conditions. Graphene grown on textured silicon surface was studied. Current-voltage characteristics, as well as photovoltaic and photoelectric properties of the different graphene/Si(100) diodes and solar cells, were investigated.

Inv4

Naphthyridine-based deep-blue TADF OLEDs with low efficiency roll-off

Dovydas Banevičius[1], Gediminas Kreiza[1], Justina Jovaišaitė[1], Saulius Juršėnas[1], Tomas Javorskis[2], Vytenis Vaitkevičius[2], Edvinas Orentas[2] and Karolis Kazlauskas[1]

[1]Institute od Photonics and Nanotechnology, Vilnius University, Sauletekio av. 3, Vilnius, Lithuania

[2]Department of Organic Chemistry, Vilnius University, Naugarduko 24, Vilnius, Lithuania

Email: dovydas.banevicius@ff.vu.lt

Thermally activated delayed fluorescent (TADF) emitters are extremely attractive due to their potential to harvest all triplet excitons via reverse intersystem crossing (rISC) process into the singlet manifold thereby ensuring 100% internal quantum efficiency [1]. However, due to pronounced charge-transfer character of TADF compounds, there are difficulties in achieving deep blue emission. Additionally, TADF-OLEDs suffer from early efficiency roll-off associated with high long-lived triplet exciton population. Therefore, TADF emitters with large rISC rate facilitating triplet up-conversion are required.

To this end, we designed new TADF emitters based on 1,8-naphthyridine acceptor (A) and differently substituted carbazole donor (D) groups [2]. Photophysical characterization of the compounds revealed high photoluminescence quantum yield (up to 86%) in mCP host with large rISC rates (up to $1.1{\times}10^{6}$ s^{-1}). We fabricated vacuum and solution processed TADF-OLEDs employing 7% naphthyridine-doped emissive layer. Devices exhibited deep blue emission with CIE colour coordinates (0.14, 0.16), external quantum efficiency of up to 17.6% and high brightness (up to 23000 cd/m^2). Most importantly, due to the large rISC rates TADF OLEDs demonstrated weak efficiency roll-off. The demonstrated emitters are among the best-performing conventional D–A-type blue/deep-blue TADF emitters in terms of EQE and efficiency roll-off properties of their devices.

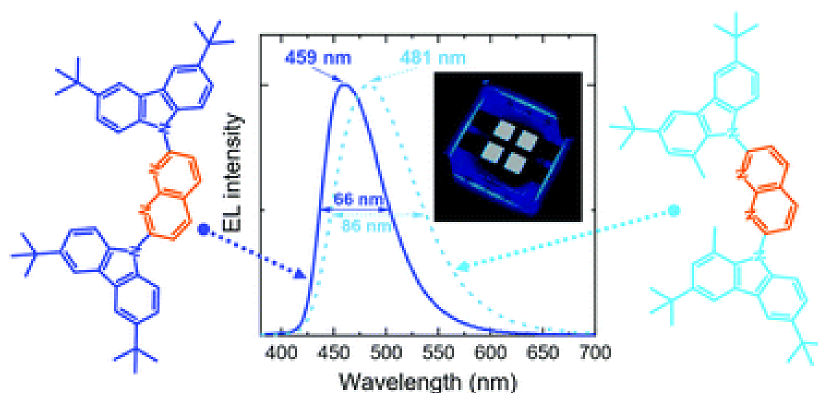

Fig. 1 Electroluminescence spectra of deep-blue and sky-blue TADF OLEDs produced utilizing naphthyridine-based emitters. Inset: picture of such working

REFERENCES

[1] H. Uoyama, K. Goushi, K. Shizu, H. Nomura, and C. Adachi, *Nature* **492**, 234. (2012).

[2] G. Kreiza, D. Banevičius, J. Jovaišaitė et al, *J. Mater. Chem. C* ***8***, 8560-8566. (2020).

O2

All-optical modulation of graphene layers

Rusnė Ivaškevičiūtė-Povilauskienė[1], Dalius Seliuta[1], Domas Jokubauskis[1], Linas Minkevičius[1], Ieva Matulaitienė[2], Žilvinas Andrius Kancleris[3], Natalia Alexeeva[1], Gintaras Valušis[1]

[1]Department of Optoelectronics, Center for Physical Sciences and Technology, Saulėtekio ave. 3 Vilnius, Lithuania

[2] Department of Organic Chemistry, Center for Physical Sciences and Technology, Saulėtekio ave. 3 Vilnius, Lithuania

[3] Department of Physical Technologies, Center for Physical Sciences and Technology, Saulėtekio ave. 3 Vilnius, Lithuania

Email: rusne.ivaskeviciute@ftmc.lt

Attractive graphene optical properties make it a desirable material for terahertz (THz) range optics. Since it is almost completely transparent in this frequency region, it has to be modulated in order to make it suitable for a functional optical element. It is known that graphene transmittance can be controlled by using electrical, chemical, thermal or optical doping [1].

In this work all-optical modulation is chosen as contactless approach.

In order to investigate the optical modulation of graphene, three types of samples are fabricated. The first one is a high resistive silicon (Si) wafer, which serves as a reference. The second sample is a single graphene layer on top of Si substrate. Since the first layer strongly interacts with a wafer, it's characteristics worsen [2]. Because of this reason, the third sample is made with two graphene layers on Si.

Using THz frequency-domain spectrometer, transmittance spectra is measured, an example of which is depicted in Fig. 1. Results show that after photoexcitation modulation maximum depth for the sample with two graphene layers goes up to 42%. It is showen that application of the second graphene layer can increase the depth of optical modulation.

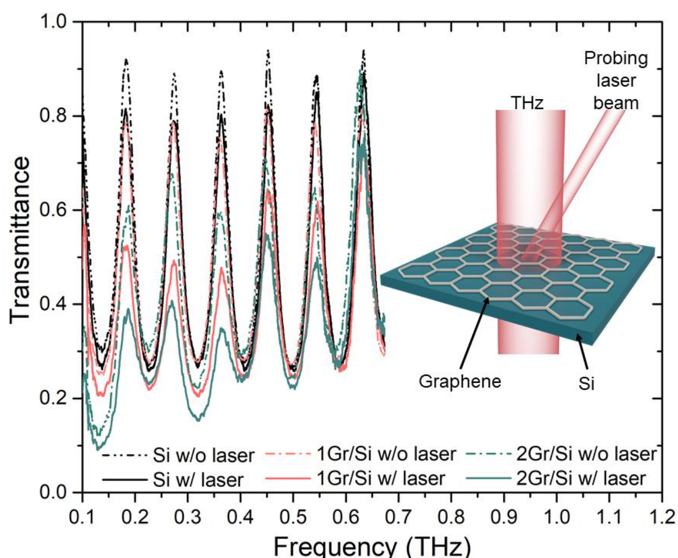

Fig. 1 Transmittance spectra of samples. Inset depicts the principal experiment scheme

Photomodulation features of graphene-on-silicon prepared using different technological approaches will be discussed.

REFERENCES

[1] R. Binder; *Optical properties of graphene*, University of Arizona, USA (2017).

[2] M. Aliiofkhazraei, N. Ali, W. I. Milne, C. S. Ozkan, S. Mitura, J. L. Gervasoni; *Graphene science book. Mechanical and chemical properties*, CRC Press (2016).

O3

Raman spectroscopic investigation of multi-walled carbon nanotubes mediated neutrophil activation

Lena Golubewa[1], Tatsiana Kulahava[2], Renata Karpics[1], Mikhail Shuba[2] and Polina Kuzhir[2,3]

[1] *Center for Physical Sciences and Technology, Sauletekio Ave. 3, LT-10257 Vilnius, Lithuania.*

[2] *Institute for Nuclear Problems of BSU, Bobruiskaya 11, 220030 Minsk, Belarus.*

[3] *Institute of Photonics, University of Eastern Finland, Yliopistokatu 2, FI-80100 Joensuu, Finland.*

Email: lena.golubewa@ftmc.lt.

Neutrophils are key players in phagocytosis, during which foreign objects are encapsulated by cells and destroyed in phagolysosomes with the help of reactive oxygen and chlorine species, and cytotoxic, proteolytic enzymes of granules. Multi-walled carbon nanotubes (MWCNT) are promising nanomaterials for nanotheranostics. MWCNTs administration may lead to the immune system response and cause inflammation. Using Raman spectroscopy, we demonstrate the neutrophil activation after exposure to MWCNTs. Fig. 1a shows the Raman spectrum of a neutrophil adhered to the glass. The lines at 1465 cm^{-1} and 1669 cm^{-1} correspond to myeloperoxidase (MPO) with an oxidized redox center of the enzyme, and lines 1167 cm^{-1} and 1399 cm^{-1} correspond to cytochrome b_{558} with an oxidized redox center. As a result of the neutrophil interaction with MWCNTs, a shift of characteristic lines in the spectra occurred, indicating the reduction of the redox center of both MPO and cytochrome b_{558} (Fig. 1b). Near to the neutrophils adhered to the glass, structures of smaller sizes are registered, the Raman spectrum of which is shown in Fig. 1c. In addition to the characteristic lines of CNTs, the 1632 cm^{-1} line indicating the presence of MPO with a reduced redox center in these structures, and the lines indicating the presence of other structural components of neutrophils (proteins: 1133 cm^{-1}, 1165 cm^{-1}, 1244 cm^{-1}, 2338 cm^{-1}; DNA: 1379 cm^{-1}; lipids: 2901 cm^{-1}) are determined. This designates, that interaction of MWCNTs with neutrophils initiates the formation of neutrophil extracellular traps, consisting of chromatin fibers, including the enzymes neutrophilic elastase and MPO [1].

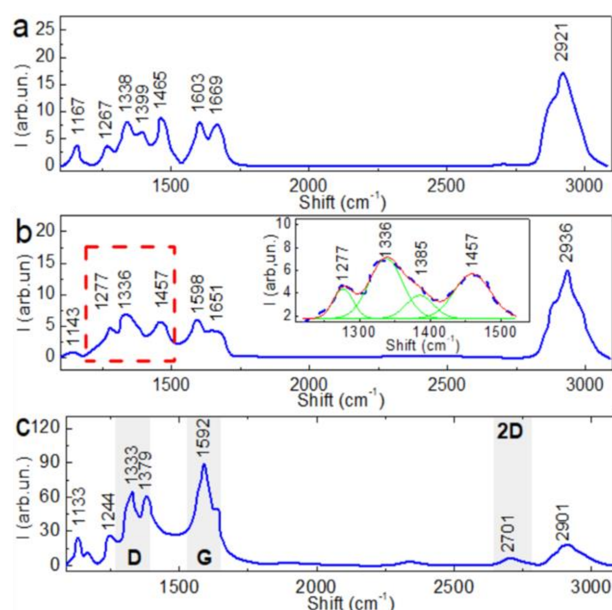

Fig. 1 Raman spectra of (a) – neutrophil, (b) – activated with MWCNTs neutrophil, (c) – NET with MWCNTs

REFERENCES

[1] G. Sollberger, D.O. Tilley, A. Zychlinsky, *Dev. Cell.* **44** (2018) pp. 542–553.

O4

Modulation of electrical and noise characteristics of carbon nanotubes based devices

A. Rehman[1], S. Smirnov[2], A. Krajewska[1], D. B. But[1,4], B. Stonio[4], M. Liszewska[3], B. Bartosewicz[3], K. Pavlov[4], G. Cywinski[1,4], D. Lioubtchenko[1,2], W. Knap[1,4,5], S. Rumyantsev[1]

[1]CENTERA Laboratories, Institute of High Pressure Physics PAS, Sokołowska 29/37, 01-142 Warsaw, Poland

[2]Department of Micro and Nanosystems, KTH Royal Institute of Technology, Malvinas Vag 10, SE-100 44 Stockholm, Sweden

[3]Institute of Optoelectronics, Military University of Technology, gen. Sylwestra Kaliskiego 2, 00-908 Warsaw, Poland

[4]Centre for Advanced Materials and Technologies CEZAMAT, Warsaw University of Technology, Poleczki 19, 02-822 Warsaw, POLAND

[5]Laboratoire Charles Coulomb, University of Montpellier and CNRS UMR 5221, 34950 Montpellier, France

Email: adilrehhman@gmail.com

Noise originating from electronic devices has significant importance and plays a vital role to understand the general physics behind the device operation. Here, we investigate the low-frequency noise characteristics of carbon nanotubes based devices. Raman, UV-Vis-NIR and scanning electron microscopes are employed for structural and optical characterization of nanotube networks. The noise amplitude (A) in most of our devices is smaller than predicted by Collins relation (i.e. $A \sim 10^{-11} x R$) [1]. Our results also reveal that quality of nanotube networks can significantly affect the noise amplitude of the devices. This implies that noise spectroscopy can be used to study the defects or distortion in nanotube networks.

The resistance and noise characteristics of carbon nanotubes devices are modulated via back-gate voltages and UV illumination. It is observed that UV illumination increases the device resistance and noise amplitude, while preserving the spectra shapes. The possible effect of temperature increase under UV illumination is excluded by measuring the resistance and noise spectra at elevated temperature. We propose an equation (1) to explain the change in the spectral noise density (S_I/I^2) of nanotube networks under UV illumination and at elevated temperature.

$$\frac{S_I}{I^2} = \frac{R_0}{(R_0+R_n)} \frac{S_{Rn}}{R_n^2} \quad \text{..} \quad (1)$$

Here, R_0 and R_n denote noiseless and fluctuating resistors, respectively whereas S_{Rn}/R_n^2 represents spectral noise density of the resistance R_n fluctuations. Our study conclude that there are at least two important components of the resistance that contribute into total resistance of nanotube networks rather than generally accepted only tube to tube interconnects [2, 3].

REFERENCES

[1] P. G. Collins, M. Fuhrer and A. Zettl, *Applied Physics Letters*, **76**, 894-896 (**2000)**.

[2] S. Soliveres, J. Gyani, C. Delseny, A. Hoffmann and F. Pascal, *Applied physics letters*, **90**, 082107 (**2007)**.

[3] G. Sassine, F. Martinez, M. El Khoury, F. Pascal and A. Hoffmann, *IEEE transactions on electron devices*, **59**, 2803-2808 (**2012)**.

Inv5

Understanding the Role of Vibronic Coherence in the Ultrafast Charge Carrier Dynamics of Photovoltaic Materials

Carlito S. Ponseca, Jr.

Divison of Biomolecular and Organic Electronics, IFM, Linköping University, Sweden
Email: Carlito.ponseca@liu.se

Efforts in understating the ultrafast processes of charge carriers in photovoltaic materials have greatly contributed in the design of solar cell devices that led to higher power conversion efficiency. Early time dynamics such as charge generation, injection and recombination are now almost well-described in most photovoltaic devices. However, the interaction between lattice motion, or vibrational modes of molecules, with charge carriers has not been explored until recently. In this talk, the role of this interaction, i.e. vibronic coherence will be presented on two solar cell materials; ternary organic solar cells[1] and single crystal organo-metal halide perovskites.[2] We surmised that despite the short coherence time between charge carriers and phonons/vibrations, this ultrafast interaction is enough to influence the lifetime and/or charge separation processes.

REFERENCES

[1] Q. Bian, F. Ma, S. Chen, Q. Wei, X. Su, I. A. Buyanova, W. M. Chen, C. S. Ponseca, Jr., M. Linares, K. J. Karki, A. Yartsev, O. Inganäs, *Nature Communications* **11** (2020) pp. 617.

[2] Y. Lan, B. J. Dringoli, D. A. Chavez, C. S. Ponseca, Jr., M. Sutton, Y. He, M. G. Kanatzidis, D. G. Cooke, *Science Advances* **5** (2019) eaaw5558.

O5

Ultrafast excited state dynamics in low-dimensional perovskite nanostructures

Kaibo Zheng

Department of Chemical Physics and NanoLund Chemical Center, Lund University P.O. Box 124, 22100 Lund, Sweden.

Department of Chemistry, Technical University of Denmark, DK-2800 Kongens Lyngby, Denmark

Email: kzheng@kemi.dtu.dk

Lead halide perovskites (LHP) have been highly spotted as promising optoelectronic materials for one decade. Derived from their bulk counterparts, low-dimensional LHP nanostructures introduced new photophysical advances that may break the bottlenecks set by the conventional LHPs. For instance, two-dimensional Roddlesden-Popper LHPs are believed to provide high stability towards moisture that used to be the main issues for the solar cell application of LHPs. LHP nanoparticles, on the other hand, can achieve almost unity photoluminescence quantum yield with tunable emission wavelength. However, the low-dimensionality would also drastically change the electronic structures of the LHPs, and consequently modify the photophysics. There always remains a trade-off between the two sides. Therefore, obtaining a systematic picture on the excited state dynamics as well as its dependence on the structures of the low-dimensional LHPs become vital for their device application. We utilized a variety of time-resolved spectroscopic technics with wide range of time windows and probe wavelengths to investigate some crucial photophysical processes of low-dimensional LHPs including their charge carrier transport and recombination, defect trapping and de-trapping, hot electron cooling, polaron formation, inter-phase charge transfer or energy transfer, etc. These helps to rationalize the underlying mechanism when they are applied in specific devices. We also put special focus on the systematic comparison between low-dimensional LHPs and bulk LHPs. We expect this would provide new guidance for further material engineering and device optimization.

REFERENCES

[1] K. Zheng, Q. Zhu, M. Abdellah, M.E. Messing, W. Zhang, A. Generalov, Y. Niu, L. Ribaud, S.E. Canton, and T. Pullerits, *J. Phys. Chem. Lett.* **6** (2015), 2969.

[2] K. Zheng, M. Abdellah, Q. Zhu, Q. Kong, G. Jennings, C.A. Kurtz, M.E. Messing, Y. Niu, D.J. Gosztola, M.J. Al-Marri, X. Zhang, T. Pullerits, and S.E. Canton, *J. Phys. Chem. Lett.* **7** (2016) 4535.

[3] K. Zheng, K. Žídek, M. Abdellah, J. Chen, P. Chábera, W. Zhang, M.J. Al-Marri, and T. Pullerits, *ACS Energy Lett.* **1** (2016) 1154.

[4] Y. Chen, Y. Sun, J. Peng, W. Zhang, X. Su, K. Zheng, T. Pullerits, and Z. Liang, *Adv. Energy Mater.* **7** (2017) 1700162.

[5] K. Zheng, Y. Chen, Y. Sun, J. Chen, P. Chábera, R. Schaller, M.J. Al-Marri, S.E. Canton, Z. Liang, and T. Pullerits, *J. Mater. Chem. A* **6** (2018) 6244.

[6] J. Meng, Z. Lan, M. Abdellah, B. Yang, S. Mossin, M. Liang, M. Naumova, Q. Shi, S.L. Gutierrez Alvarez, Y. Liu, W. Lin, I.E. Castelli, S.E. Canton, T. Pullerits, and K. Zheng, *J. Phys. Chem. Lett.* **11** (2020).

O6

Terahertz emission from a bulk GaSe crystal excited by above-bandgap photons

Ričardas Norkus[1], Ignas Nevinskas[1] and Arūnas Krotkus[1]

[1]*Centre for Physical Sciences and Technology, 10222, Saulėtekio av. 3, Vilnius, Lithuania.*
Email: ricardas.norkus@ftmc.lt

Gallium selenide is a layered III-VI semiconductor crystal, and the layers are stacked together by a weak van der Waals force. GaSe is widely used as non-linear optical crystal for infrared and THz generation and electrooptic sampling [1]. Also recently it has attracted interest as it has potential application as photoelectric devices that operate in the visible range [2].

One of the methods to study band structure of a semiconductor is THz emission spectroscopy (TES). Technique was already used to determine band structure parameters such as subsidiary valley position [3] and heterojunction offset value. Many materials were already investigated most of them III-VI semiconductors.

Experiments were done using ~50 μm thick p-type GaSe sheets cleaved from the Bridgman grown crystal. TES spectras of these crystals were measured with different excitation polarizations (fig. 1). THz generation starts near the bandgap (~2eV) of GaSe, then generation efficiency increases up to ~ 2,3 eV, the later efficiency drop could be explained by scattering to subsidiary valleys. When excitation energy reaches ~3 eV THz pulse amplitude starts to increase again due to excitation from lower laying valence band. THz pulse amplitude dependence on azimuthal angle above band-gap shows emission due to effect related to the crystal anisotropy.

In this work GaSe subsidiary valley position was determined - 0,21 eV.

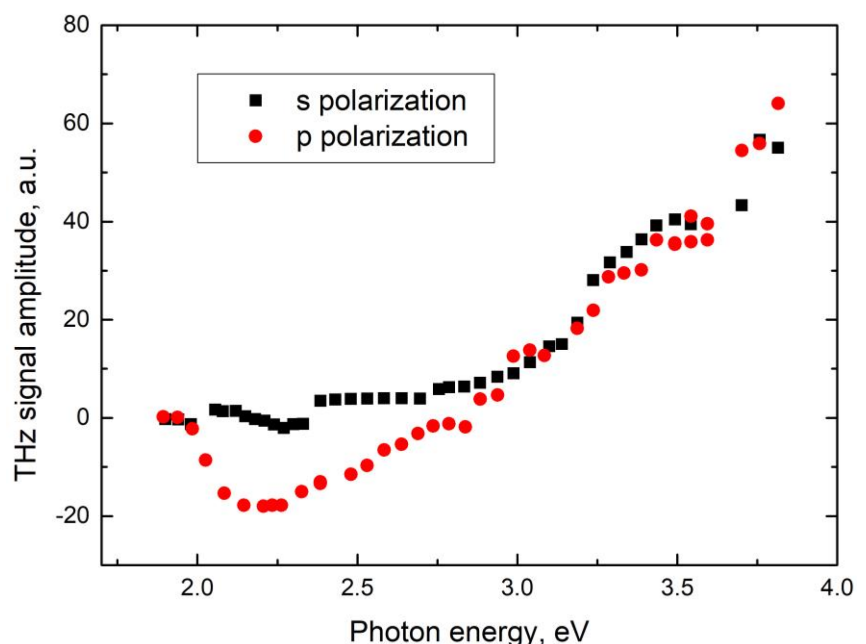

Fig. 1 TES spectra of p- type GaSe excited by 30 degrees angle to the surface normal

REFERENCES

[1] K. Liu, J. Xu, and X.-C. Zhang, “GaSe crystals for broadband terahertz wave detection”, Appl. Phys. Lett. 85, 863 (2004).

[2]S. Sorifi, M. Moun, S. Kaushik,and R. Singh, “High-Temperature Performance of a GaSe Nanosheet-Based Broadband Photodetector”, ACS Applied Electronic Materials, 2, 670-676 (2020).

[3] A. Arlauskas, A. Krotkus, “THz excitation spectra of AIIIBV semiconductors”, Semicond. Sc. Technol., 27, 115015 (2012)

O7

Investigation of two-dimensional plasma resonances in grating-gated AlGaN/GaN heterostructures by terahertz time domain spectroscopy

Daniil Pashnev*, Vadym Korotyeyev, Andrzej Urbanowicz, Irmantas Kašalynas
THz photonics laboratory, Department of Optoelectronics, Center for Physical Sciences and Technology, Vilnius, Lithuania
Email: daniil.pashnev@ftmc.lt.

Exclusive electrical robustness and relatively high electron mobility make III-nitride heterostructures an excellent candidate for the development of plasmonic terahertz (THz) devices [1, 2]. Excitation of 2D plasmons in grating-gated heterostructures has been studied by a Fourier transform infrared spectroscopy only [2, 3]. Meanwhile, THz time domain spectroscopy is a powerful technique used to investigate the material properties (complex dielectric constant and refractive index dispersion) measuring both signal amplitude (power) and phase spectra in transmission and reflection geometry [4].

In this work, the power and phase spectra of THz pulses transmitted through the 2D electron plasma in grating-gated AlGaN/GaN structures were investigated in the frequency range
0.1-4 THz by using the T-SPEC 800 spectrometer (from TeraVil). The samples were fabricated of standard AlGaN/GaN high electron mobility transistor (HEMT) structures grown on a 500 µm-thick semi-insulating SiC substrate. Periodic metal grating of 2x2 mm size and 50% filling factor was used for efficient radiation coupling with 2D plasmons. Samples with three different grating periods of 600, 800, and 1000 nm were investigated at 80K.

Resonant excitation of the 2D plasmons was experimentally observed for all samples in the frequency range of 1-3 THz. The features were perceived as the emergence of distinctive minimum and inflection point in the power and phase spectra, respectively. In the case of the samples with grating period of 1000 and 600 nm, the resonance position was found at 1.4 THz and 2.2 THz, respectively. The latest is the largest value of fundamental 2D plasmon mode that has been observed experimentally so far in AlGaN/GaN HEMT structures [5]. Due to resonant THz radiation coupling, the deviation from a nominal value of transmitted power and phase was found up to 30 % and 8 deg, respectively. The quality factor of 2D resonances was estimated to be up to 4. Comparative analysis of amplitude and phase spectra revealed that the phase signal was less sensitive to the defects of the grating-coupler. The resonant features were also simulated in the framework of the rigorous solution of the Maxwell equations [6, 7].

REFERENCES

[1] M. Bauer et. al., IEEE Trans. Terahertz Sci. Technol. 9, 430 (2019)
[2] V.A. Shalygin et. al., J. Appl. Phys. 126, 183104 (2019).
[3] A.V. Muravjov et. al., Appl.Phys.Lett. 96, 042105 (2010).
[4] I. Pupeza et. al., Opt. Express 15(7), 4335 (2007)
[5] D. A. Pashnev et. al., under submission Appl. Phys. Lett. (2020)
[6] S. A. Mikhailov, Physical Review B, 58(3), (1998)
[7] V.V. Korotyeyev et al, SPQEO 22(2), 237-251 (2019)

O8

On the origin of the 4.1 eV luminescence in hexagonal boron nitride

Marek Maciaszek[1], Mažena Mackoit-Sinkevičienė[2], Lukas Razinkovas[2] and Audrius Alkauskas[2]

[1]*University of Warsaw, Poland*
[2]*Center for Physical Sciences and Technology, Vilnius, Lithuania*
Email: marek.maciaszek@pw.edu.pl

The structured luminescence band with a zero-phonon line (ZPL) at 4.1 eV in hexagonal boron nitride is known for many decades. Recently observed single-photon emission associated with this band made its explanation even more important. In this contribution we show that the carbon dimer CB-CN accounts for all known facts about the 4.1 eV band: the involvement of carbon, the energy of ZPL, the Huang-Rhys factor (quantifying the strength of electron-phonon coupling), and the radiative lifetime.

Inv6

Remote epitaxy of GaN via Graphene

Kazimieras Badokas[1], Arūnas Kadys[1], Tomas Grinys[1], Marek Kolenda[1], Sandra Stanionytė[1,2], Martynas Skapas[1,2], Jūras Mickevičius[1], and Tadas Malinauskas[1]

[1] 1Institute of Photonics and Nanotechnology, Vilnius University, Vilnius LT-10257, Lithuania
2Center for Physical Sciences and Technology, Vilnius LT-10257, Lithuania
Email: tadas.malinauskas@ff.vu.lt

Group-III nitrides are promising materials for next generation optoelectronic devices. Extensive effort has been made to optimize group-III nitride heteroepitaxy for many years. However, inherent lattice mismatch and thermal expansion difference between nitrides and foreign substrates is still a limitation for GaN quality. On the other hand, homoepitaxy is still economically rarely viable. Remote epitaxy via two-dimensional (2D) materials such as graphene would enable facile layer release from 2D surfaces preserving expensive bulk nitride substrate[1, 2]. Growth via graphene on the foreign substrates could potentially solve inherent problems of heteroepitaxy allowing relaxation of epilayer.

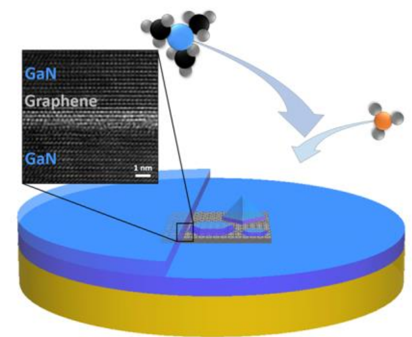

Fig. 1 The scheme of remote epitaxy of GaN via graphene on GaN/sapphire substrates. Inset shows TEM micrograph of GaN/graphene/GaN interface.

We investigated the MOCVD growth of GaN via graphene on different substrates GaN/sapphire and SiC substrates. We investigated wet and dry transfer of graphene onto GaN/sapphire substrate. The quality of transferred graphene was investigated by Raman spectroscopy using 535 nm laser, which confirmed the presence of monolayer graphene with low defect density.

Afterward, a close-coupled showerhead metalorganic chemical vapor deposition reactor (MOCVD) was used to grow GaN on graphene in several growth campaigns. Growth conditions such as temperature, pressure and V/III-ratio were varied in order to optimize GaN layer quality. The structural and optical properties of the grown epitaxial layers were investigated by X-ray diffraction, scanning and transmission electron microscopies, atomic force microscopy and photoluminescence techniques. Developed multi-step growth method ensured the successful growth of GaN films on GaN/sapphire templates with the presence of the graphene layer after all growth steps confirmed by Raman measurements.

REFERENCES

[1] Y. Kim et al., Remote epitaxy through graphene enables two-dimensional material-based layer transfer, Nature 544, 2017

[2]W. V. Lundin et al., Growth of III-N/graphene heterostructures in single vapor phase epitaxial process, J. Cryst. Growth 504, 2018

O9

Temperature-& Pressure-induced transitions in HgTe QWs

I. Yahniuk[1*], S. S. Krishtopenko[2,3], M. Majewicz[4], S. A. Dvoretsky[6], N. N. Mikhailov[6], F. Teppe[1,3], G. Cywiński[1], G. Grabecki[4], A. Kazakov[5],T. Dietl[4,5] and W. Knap[1,3]

[1] International Research Centre CENTERA, Institute of High Pressure Physics, Polish Academy of Sciences, 01-142 Warsaw, Poland
[2] Institute for Physics of Microstructures RAS, GSP-105, 603950, N. Novgorod, Russia
[3] Laboratoire Charles Coulomb (L2C), UMR CNRS 5221, University of Montpellier, F-34095 Montpellier, France
[4] Institute of Physics PAS, al. Lotników 32/46, PL 02-668 Warsaw, Poland
[5] International Research Centre MagTop, al. Lotników 32/46, PL 02-668 Warsaw, Poland
[6] Rzhanov Institute of Semiconductor Physics SB of RAS, 630090 Novosibirsk, Russia
Email: ivan.yahniuk@unipress.waw.pl

In HgTe quantum wells (QWs), band structure properties of depend on QW widths. For thin quantum wells, conduction band forms by s-orbitals functions resulting from deep penetration of the wave function from CdTe side. Valence band is formed by p-type functions. With increasing of d_{QW} , an energy gap decreases, and when QW width reach critical thickness d_c, conduction band and valence touch each other at k = 0, i.e. the energy gap is equal zero. In case of $d_{QW} > d_c$ sequence of the energy states is inverted, first heavy-hole like subband H1 placed above the first electron-like E1 subband. Such band inversion in HgTe QWs suggests the existence of nontrivial topological insulator phase [1].

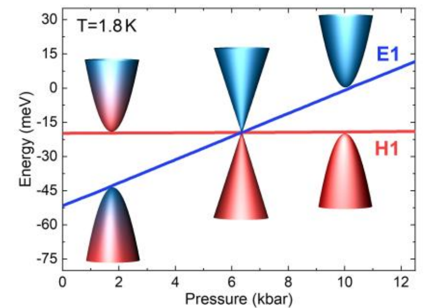

Fig. 1 The evolution of the both E1 and H1 sub-bands at k=0 against hydrostatic pressure for 8nm of HgTe QW grown in (031) crystallographic direction. Blue and red colors correspond to the electron-like E1, the light hole H1 subbands

For normal band ordering ($d < d_c$), an energy gap has tendency opens with applying of pressure [2]. The situation is distinguish in case of WQs with inverted band sequence. For example, in 8 nm of WQ, pressure increasing lead towards vanishing of E_g. At certain value of pressure, denoted as P_c, system is tuned to the band structure with massless Dirac fermions. Further pressure increasing yield to the band gap opening and system has the normal band sequence (see Fig.1). A temperature also can be regarded as external parameter that allow convert the band ordering.

In this work, we report on the clear observation of topological phase transition in HgTe QWs induced by temperature and hydrostatic pressure. Magnetotransport measurements allow us accurately extract critical magnetic fields B_c for various temperature and pressure values. By following the pressure (temperature) dependence of B_c, we define a critical points P_c, T_c, corresponding to the topological- trivial phase transitions.

REFERENCES

[1] M. König, S. et.al., Science 2007, 318, 766.
[2] S. S. Krishtopenko et al., Phys. Rev. B 2016, 94, 245402.

O10

Annealing-induced reduction of strain in GaAs/GaNAs core-shell nanowires

Roman M. Balagula[1,2], Mattias Jansson[2], Mitsuki Yukimune[3], Jan E. Stehr[2], Fumitaro Ishikawa[3], Weimin M. Chen[2], and Irina A. Buyanova[2]

[1]Optoelectronics Department, Center for Physical Sciences and Technology, Saulėtekio al. 3, LT-10257, Vilnius, Lithuania.

[2]Department of Physics, Chemistry and Biology, Linköping University, 581 83, Linköping, Sweden.

[3]Graduate School of Science and Engineering, Ehime University, 790-8577, Matsuyama, Japan

Email: roman.balagula@ftmc.lt.

Core-shell nanowires (NWs) attract research attention because of their peculiar properties such as flexibility in growth substrates and alloy contents, controllable density of states, large surface-to volume ratio, and in-built potential for strain engineering. III-V nanowires investigated in this work are chosen because of the possibility of efficient variation of the bandgap owing to the giant-bandgap bowing effect observed in the dilute nitrides [1].

GaAs/GaNAs core/shell nanowires MBE-grown on Si substrates were investigated by means of polarization-resolved micro-photoluminescence (μ-PL) measurements. Obtained photoluminescence spectra of NW ensembles demonstrated broad peaks corresponding to nitrogen content of 2% in GaNAs active shell with exponential tails at low temperatures attributed to the localized exciton emission. Post-growth annealing resulted in increase in PL intensity owing to annealing-out of non-radiative defects. A change in localization potential was also observed that was attributed to improvement of long-range uniformity of GaNAs alloy.

Core-shell structures experience global strain owing to the lattice mismatch of core and shell materials [2]. This strain results in the splitting of hole subbands of the active shell that can be probed by means of polarization-resolved μ-PL measurements of single NWs mechanically transferred onto another Si substrate. The value of strain in the studied structures was estimated theoretically and experimentally along with the effects of annealing. The resulting emission from single NWs was predominantly polarized orthogonally to NW growth axis. The decrease in heavy hole-light hole splitting was observed in PL spectra of annealed NWs at room temperature demonstrating the reduction of global core-shell strain in the NWs.

Low-temperature PL spectra of single NWs contained sharp emission lines attributed to QD-like areas in NWs forming due to the nitrogen clustering in the GaNAs shell. The changes in fine structure of these sharp lines with annealing demonstrated the reduction of local strain in these areas as well.

As post-growth annealing is a frequent method of treatment of the semiconductor structures the observed effects of annealing should be considered when attempting the strain engineering approach to the device fabrication.

REFERENCES

[1] W. G. Bi and C. W. Tu, *Appl. Phys. Lett.* **70** (1997) pp. 1608–1610.

[2] J. Grönqvist, *et al.*, *J. Appl. Phys.* **106** (2009) pp. 053508.

O11

GaInAs/GaAs QUANTUM STRUCTURES FOR NIR VECSEL

Andrea Zelioli[1], Algirdas Jasinskas[2], Simona Pūkienė[2], Lukas Jočionis[2], Bronislovas Čechavičius[2], Evelina Dudutienė[2] and Renata Butkutė[2, 3]

[1] *Department of Physics, University of Modena, Italia*

[2] *Center for Physical Sciences and Technology, Vilnius, Lithuania*

[3] *Institute of Photonics and Nanotechnology, Faculty of Physics, Vilnius University, Lithuania*

Email: 190558@studenti.unimore.it

Laser devices find many different application in various technologies, such as optical fiber communication, optical digital recording, material processing, spectroscopy analysis and many others. Since when in 1960 the first laser was build, many different types of lasers where developed each of them with some peculiarities that made them suitable for different application. Some of the parameters that define the possible applications of laser in different fields are emission wavelength, beam quality, operation temperature, output power, methods of excitation, power consumption, speed of modulation and device size and the range of tunability of all of this characteristics. Vertical external cavity surface emitting lasers (VECSEL) do combine many different interesting properties and were designed to overcome some of the key issues of conventional semiconductors lasers, mainly low power output, output beam profile with unusual shape and big beam divergence. VECSELs are able to produce high optical output power with circular beam quality.

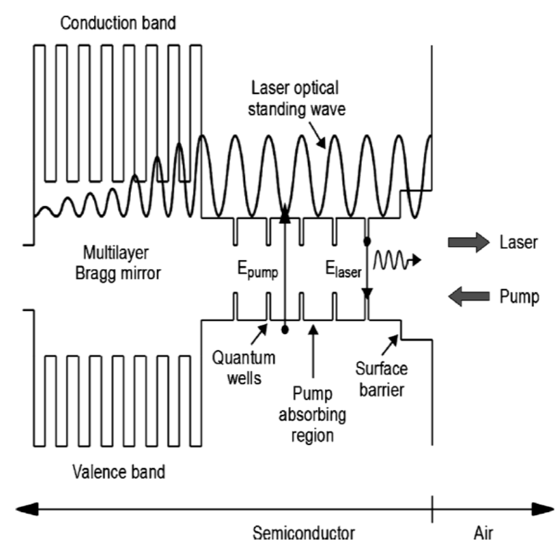

Fig. 1. Energy levels across the VECSEL structure [1].

In this work we investigated the growth parameter of VECSEL shown in figure 1 on a GaAs (001) substrate optimizing the structure for the emission at a wavelength of 976nm. Multiple InGaAs/GaAs quantum wells (MQWs) and AlAs/GaAs Distributed Bragg reflector (DBR) grown by solid MBE system were used for VECSEL architecture. During the optimization process In content, the width of QW and the width of barriers were changed. The reflectance of DBR was modelled for 25-30 GaAs and AlAs periods to obtain higher than 97% at central DBR wavelength of 976 nm. All grown layers and VECSEL structures were characterized by Atomic Force Microscopy, Reflectance and Photoluminescence measurements.

REFERENCES

[1] Mark Kuznetsov, VECSEL Semiconductor Lasers: A Path to High-Power, Quality Beam and UV to IR Wavelength by Design, Semiconductor Disk Lasers. Physics and Technology. Edited by Oleg G. Okhotnikov, 2010, WILEY-VCH Verlag GmbH & Co. KGaA, Weinheim.

O12

A3-B5 QW structures for IR range optoelectronic devices

Simona Pūkienė, Algirdas Jasinskas, Virginijus Bukauskas, Vladimir Agafonov, Mindaugas Kamarauskas, Algimantas Lukša, Andrius Bičiūnas, Bronislovas Čechavičius, Arūnas Šetkus and Renata Butkutė

Center for Physical Sciences and Technology, Saulėtekio av. 3, LT-10257, Vilnius, Lithuania
Email: simona.pukiene@ftmc.lt

A3-B5 family semiconductors, especially Bi containing GaAs compound, are currently under investigation because of important role in various optoelectronics devices, including lasers for optical fiber communications (1.3 µm and 1.55 µm), undersea, space, and high-data-rate applications (780 nm – 830 nm).

In this work, laser diode structures were grown by molecular beam epitaxy (MBE) using Veeco GENxplor R&D reactor on n-GaAs substrate. To optimize the multiple quantum well (MQW) structure for applications as an active area in infrared laser diodes, the complex investigation of influence of structure geometry (QW number, thickness, QW and barrier material) on LD parameters was performed. Since our previous work revealed that room temperature photoluminescence (RT-PL) can be increased by more than 50 times in the GaAsBi QWs using parabolic graded barriers, compared to standard rectangular quantum well (RQW) structures [1], two-design structures were epitaxially grown and characterized. Laser diodes were fabricated by a UV photolithography. The metal contacts were deposited by e-beam on top and bottom of laser crystal.

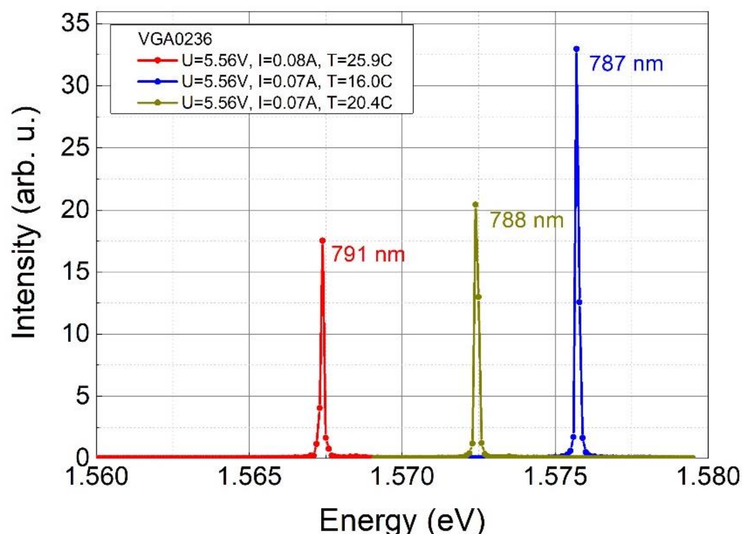

Fig. 1. EL spectra of laser diode containing GaAs QW with parabolic AlGaAs barriers measured at different temperatures

The comparative study of LDs containing PQW and RQW structures was performed to clarify the role of architecture and to establish the key parameters.

Laser diodes were characterized by measurements of RT-PL, current-voltage (I-V) and current-power (I-P) behaviors. The electroluminescence (EL) spectra measured in temperature range of 15 °C - 30 °C for laser diode with single PQW exhibiting lasing properties in near infrared region are presented in Fig. 1.

The authors gratefully acknow-ledge support from the Central Project Management Agency grant 01.2.2-CPVA-K-703-03-0019.

REFERENCES

[1] S Pūkienė, et al.Nanotechnology, Vol. **30**, 455001 (11pp) (2019).

Inv7

Magnetoresistance Relaxation Phenomena in Nanostructured Lanthanum Manganite Films

Nerija Žurauskienė[1,2], Vakaris Rudokas[1], Dainius Pavilonis[1], Voitech Stankevič[1,2], Valentina Plaušinaitienė[1,3]

[1]Department of Functional Materials and Electronics, Center for Physical Sciences and Technology, Sauletekio ave. 3, LT-10257 Vilnius, Lithuania.

[2]Faculty of Electronics, Vilnius Gediminas Technical University, Naugarduko 41, LT-03227 Vilnius, Lithuania.

[3]Institute of Chemistry, Faculty of Chemistry and Geosciences, Vilnius University, Naugarduko 24, LT- 03225 Vilnius, Lithuania

Email: nerija.zurauskiene@ftmc.lt.

Recently, it was demonstrated that nanostructured lanthanum manganite films which exhibit the colossal magnetoresistance effect (CMR) can be successfully used for the development of CMR-B-scalar sensors [1]. These are able to measure the magnitudes of high-pulsed magnetic fields of millisecond duration in very small volumes. Such sensors have been used at room temperatures to measure the magnetic diffusion processes during railgun operation and the distribution of transient magnetic fields in non-destructive pulsed-field magnets. However, for condensed matter physics and other special applications sensors operating at cryogenic temperatures and measuring magnetic fields in a wide range of amplitudes are required. In such cases, it is important to avoid or minimize the magnetic memory effects [2] which limit the speed of such sensors.

In this study, we present the results of an investigation of magnetoresistance (MR) and resistance relaxation in nanostructured lanthanum manganite films grown by the pulsed injection MOCVD technique onto polycrystalline substrates.

It was found that the dynamics of resistance relaxation in nanostructured manganite films upon removal of the external magnetic field has two components: 'fast' occurring in hundreds of microseconds and 'slow' which takes place longer than several milliseconds. It was demonstrated that the 'fast' process can be analyzed by the Kolmogorov–Avrami–Fatuzzo model [3], taking into account the reorientation of the magnetic domains into their equilibrium state, and the 'slow' process – by the Kohlrausch–Williams–Watts [4] model considering the short-range interaction of the magnetic moments in disordered grain boundaries as having spin-glass properties. The dependences of the time constants and remnant amplitudes of these processes on ambient temperature and magnetic field are presented and analyzed. The relation of relaxation processes with microstructure of manganite films will be demonstrated and discussed.

REFERENCES

[1] T. Stankevic et al., Rev. Sci. Instrum., 85, 044704 (2014).
[2] M. Sirena et al., Phys. Rev. B, 64, 104409 (2001).
[3] E. Fatuzzo, Phys. Rev., 127, 1999, (1962).
[4] G. Williams and D. C. Watts, Trans. Faraday Soc., 66, 80 (1970).

Inv8

Narrow excitonic lines and large-scale homogeneity of transition metal dichalcogenides grown by MBE on hBN

W. Pacuski[1], M. Grzeszczyk[1], K. Nogajewski[1], A. Bogucki[1], K. Oreszczuk[1], R. Rodek[1], J. Kucharek[1], K.E. Połczyńska[1], B. Seredyński[1], R. Bożek[1], S. Kret[2], T. Taniguchi[3], K. Watanabe[3], J. Sadowski[1,2,4], T. Kazimierczuk[1], M. Potemski[1,5], P. Kossacki[1]

[1] *Faculty of Physics, University of Warsaw, Pasteura St. 5, 02-093 Warsaw, Poland,*

[2] *Institute of Physics, Polish Academy of Sciences, al. Lotników 32/46, 02-668 Warsaw, Poland,*

[3] *National Institute for Materials Science, Tsukuba, 305-0047, Ibaraki, Japan,*

[4] *Department of Physics and Electrical Engineering, Linnaeus University, Kalmar, Sweden,*

[5] *Laboratoire National des Champs Magnétiques Intenses, CNRS-UJF-UPS-INSA, 25, avenue des Martyrs, 38042 Grenoble, France*

Email: Wojciech.Pacuski@fuw.edu.pl

Monolayer transition metal dichalcogenides (TMDs) are two-dimensional materials with exceptional optical properties such as high oscillator strength, valley related excitonic physics, efficient photoluminescence, and several narrow excitonic resonances. However, above effects have been so far explored only for structures produced by techniques involving mechanical exfoliation and encapsulation in hBN inevitably inducing considerable large-scale inhomogeneity. On the other hand, techniques which are essentially free from this disadvantage, such as molecular beam epitaxy (MBE), have to date yielded only structures characterized by considerable spectral broadening, which hinders most of interesting optical effects.

We report for the first time on the MBE-grown TMD exhibiting narrow and fully resolved spectral lines of neutral and charged exciton (see Fig. 1). Moreover, our MBE-grown TMD exhibits unprecedented high spatial homogeneity of optical properties, with variation of the exciton energy as small as 0.16 meV over a distance of tens of micrometers. Our recipe for MBE growth [1,2] is presented for $MoSe_2$ and includes extremely slow growth rate, the use of atomically flat hexagonal boron nitride (hBN) substrate and the annealing at very high temperature. Importantly, good optical properties are achieved for as-grown sample, without any post growth exfoliation and encapsulation in hBN. This novel recipe opens a possibility of MBE growth of TMD and their heterostructures with optical quality, dimensions and homogeneity required for optoelectronic applications.

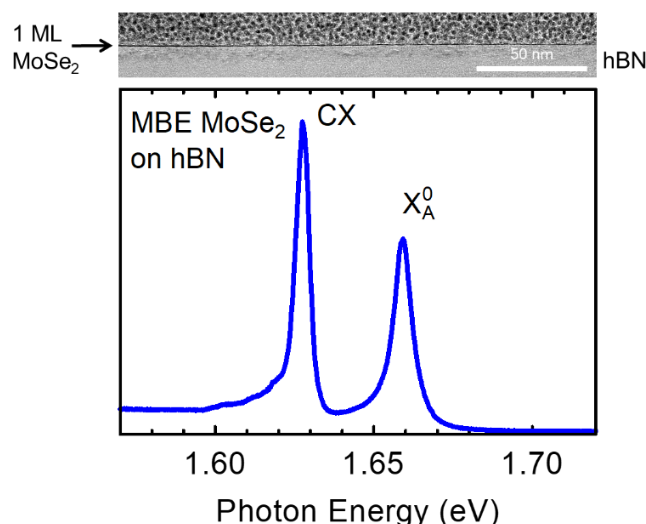

Fig. 1. Crossesciton and low temperature PL spectrum with excitonic resonances for $MoSe_2$ monolyaer grown by MBE on hBN.

REFERENCES

[1] W. Pacuski, et al; *Nano Letters* **20**, (2020) pp. 3058-3066.

[2] Z. Ogorzałek, et al; *Nanoscale* **12** (2020) pp. 16535-16542.

O13

Graphene gate GaN/AlGaN field effects transistors for THz detection

M. Dub,[1,4] P. Sai,[1,4] D. B. But,[1,2,4] A. Przewłoka,[1,6] A. Krajewska,[1] I. Pasternak,[5] G. Cywiński,[1,2] M. Sakowicz,[1] S. Rumyantsev,[1,2] W. Knap[1,2,3]

[1] *Center for Terahertz Research and Applications (CENTERA), Institute of HighPressure Physics PAS, ul. Sokołowska 29/37, 01-142, Warsaw, Poland*

[2] *CEZAMAT, Warsaw University of Technology , 02-822, Warsaw, Poland*

[3] *Laboratoire Charles Coulomb, University of Montpellier and CNRS UMR 5, Montpellier, France*

[4] *V. Ye. Lashkaryov Institute of Semiconductor Physics, NAS of Ukraine, 03680 Kyiv, Ukraine*

[5] *Faculty of Physics, Warsaw University of Technology , 00-662 Warsaw, Poland*

[6] *Institute of Optoelectronics, Military University of Technology, 00-908 Warsaw, Poland*

Email: mdub@unipress.waw.pl

Graphene (GR) is transparent for electromagnetic radiation in the very wide spectral range, including sub-terahertz and terahertz frequency ranges. Particularly, at frequency of 1 THz, graphene transmittance is ~ 96 percent [1]. This makes graphene very promising for such applications like opto-transistors and terahertz devices with transparent electrodes.

We report on GaN/AlGaN fin-shaped field-effect transistors (FinFETs) with GR gate. Small gate area and narrow channel make this transistors promising for terahertz applications. FinFETs structures were fabricated using the technology described in details in Ref. [2]. GR gates were formed by high-speed electrochemical delamination method (see insert in Fig. 1) on pre-deposited metal pads which were used as the contacts to GR. Barrier height and ideality factor of GR/AlGaN Schottky barrier found from current-voltage characteristics were φ_b = (1.0 - 1.26) eV and (1.7 - 2.5), respectively.

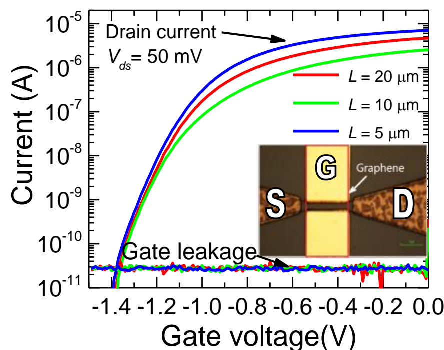

Fig. 1. Transfer characteristics of FinFETs with GR gate, channel width W = 4 μm and gate length L = 5, 10, 20 μm; photo of the device active area is present on insert.

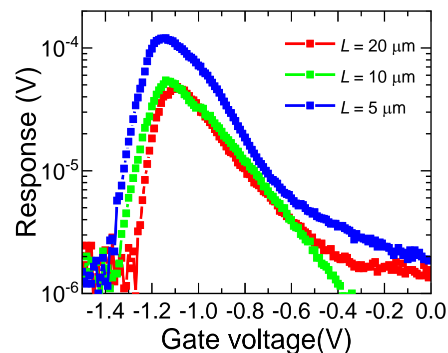

Fig. 2. Response of GR gate FinFETs with different gate length L = 5, 10, 20 μm and constant channel width W = 4 μm at the frequency f = 120 GHz and RT.

Characteristics of GaN/AlGaN FinFETs with GR gate are shown in Fig. 1. The devices were characterized by 6 order of magnitude on/off ratio and subthreshold slope ~ 1.1. Aging during 6 months did not indicate noticeable change in the current voltage characteristics. Measurements of the low frequency noise allowed us to extract the effective trap density responsible for noise, which was similar as for Ni/Au gate FinFETs. Results of detection at the frequency f = 120 GHz by FinFET with GR gate at room temperature are shown in Fig. 2. The signal peaks are located near the threshold voltage of investigated FinFETs.

To summarize, we have demonstrated GR gate GaN/AlGaN FinFETs. Combined properties of high transmittance in THz frequency range of GR, high sheet density of two-dimensional electron gas in GaN/AlGaN, and fin shape of these devices make them promising for plasmonic THz detection.

REFERENCES

[1] Choi, Hyun Joo, et al., Scientific Reports **7**, 42833 (2017)

[2] P. Sai, et al., Semicond. Sci. Technol. **34** 024002 (2019)

O14

THz magnetospectroscopy of HgCdTe bulk crystals with different Cd content

Maria Szoła[1], D. Yavorskiy[1,2], J. Łusakowski[2], D. But[1], I. Yahniuk[1], N.N Mikhailov[5], S. A. Dvoretsky[5], V. I. Gavrilenko[4] and W. Knap[1,3]

[1] *CENTERA Laboratories, Institute of High Pressure Physics, PAS, Sokołowska 29/37, 01-142 Warsaw, Poland*

[2] *Faculty of Physics, University of Warsaw, Pasteura 5, 02-093 Warsaw, Poland*

[3] *Laboratoire Charles Coulomb, UMR, CNRS 5221, 34095 Montpellier, France*

[4] *Institute for Physics of Microstructures, RAS, GSP-105, 603950, N. Novgorod, Russia*

[5] *Rzhanov Institute of Semiconductor Physics SB RAS, 630090, Novosibirsk, Russia*

Email: mszola@mail.unipress.waw.pl

The constant development of science and industry requires inventing novel methods and techniques of THz radiation detection, therefore the search for new detectors and research of new materials is still a vital part of THz studies. Additionally improvements in techniques of growning crystals such as HgCdTe have brought back the interest of the scientific world for these materials due to their Dirac properties.

Four HgCdTe samples were chosen for the experiments, each with different cadmium content: 15.1 % Cd, 15.2% Cd, 16.2% Cd and 17.5% Cd. Transmission experiments were carried out at pumped LHe at T=2 K and carbon bolometer was used as a THz radiation detector. As a THz radiation source FIR laser was used, with its six lines: 70.6 μm, 96.5 μm, 118.8 μm, 163 μm, 186 μm and 454 μm.

Performed measurements were used to extract the velocity $\tilde{c}$ and rest mass $\tilde{m}$ of carriers. Both of those values were obtained after fitting of the simplified Kane model described in [1]. The rest mass value increased with the cadmium content, while the velocity of carriers remained roughly the same throughout the measurements of various samples.

It has to be noted that the obtained values of velocity and rest mass were compared with values determined from the technological parameters of growth. Relationships of those values are $E_G = 2\tilde{m}\tilde{c}^2$ and due to the fact that obtained results are in agreement with expected values of E_G, it can be concluded that the simplified Kane model can be used to determine the pseudo-relativistic Kane fermion parameters of the velocity $\tilde{c}$ and rest mass $\tilde{m}$ of carriers as a function of cadmium content.

This research was partially supported by a Polish National Science Centre UMO-2017/27/N/ST7/01771 grants and the Foundation for Polish Science through a TEAM/2016-3/25 and the IRA Programme co-financed by EU within SG OP grants No. MAB/2018/9.

REFERENCES

[1] F. Teppe et al. Nature Comm. **7**, 12576 (2016).

O15

Machine learning enhanced design of diffractive optical elements

Paweł Komorowski[1], Mateusz Surma[2], Ryszard Piramidowicz[1] and Agnieszka Siemion[2]

[1]*Institute of Microelectronics and Optoelectronics, Warsaw University of Technology, Koszykowa 75, Warsaw, 00662 Poland*
[2]*Faculty of Physics, Warsaw University of Technology, Koszykowa 75, Warsaw, 00662 Poland*
Email: p.komorowski@imio.pw.edu.pl

Diffractive optical elements (DOEs) are capable of reshaping of incoming radiation within very thin structure (often referred as single surface). It results not only in much lighter, compact and cost-effective structures, but also gives opportunity of obtaining light distributions unattainable by refractive approach. So far, DOEs have most commonly been designed with utilization of numerically calculated diffraction integrals as discrete Fourier transforms or convolutions [1], which is usually time and memory consuming, especially for bigger matrices.

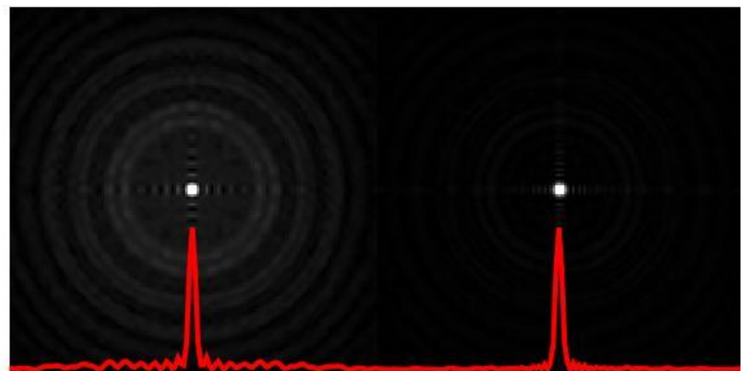

Fig. 1 Comparison of the focal spots obtained from the unoptimized (left) and optimized (right) Fresnel lenses.

Here, we propose application of convolutional neural network for emulation of light propagation, which can be utilized for optimization of DOEs, realizing focusing of light into arbitrary shapes. Learnable parameters of the net correspond to the phase distribution of designed element. Therefore, proper network training results in ready to use, optimized structure. This method is especially appealing for designing structures, working in the terahertz spectral range. It comes from the fact, that size of the smallest details of the structures depends linearly on the wavelength, which here is in order from hundreds of microns to single millimeters. Therefore, structures designed for sub-THz frequencies can be easily manufactured with 3D printing techniques and with proper production and design methods [2] also higher frequencies are attainable.

Results of the optimization of the structures for different applications as well as comparison with other methods will be presented during the conference. As an example, results of the optimization of the simple, convergent Fresnel lens are shown in Fig. 1.

REFERENCES

[1] Goodman, J. W. (2005). Introduction to Fourier optics. Roberts and Company Publishers.
[2] Siemion, A., Komorowski, P., Surma, M., Ducin, I., Sobotka, P., Walczakowski, M., & Czerwińska, E. (2020). Terahertz diffractive structures for compact in-reflection inspection setup. Optics Express, 28(1), 715-723.

O16

Antenna Characterization of Monolithically Integrated Detectors for 0.62 THz

Elham Javadi[1], Dmytro B. But[1,2], Aleksander Cherniadiev[1], Kestutis Ikamas[3,4], Alvydas Lisauskas[1,3]

[1]*CENTERA Laboratories, Institute of High Pressure Physics PAS, Warsaw, Poland*
[2]*CEZAMAT Warsaw Technical University, Warsaw 02-346, Poland*
[3]*Institute of Applied Electrodynamics and Telecommunications, Vilnius University, Vilnius, Lithuania*
[4]*General Jonas Žemaitis Military Academy of Lithuania, Vilnius, Lithuania*
Email: D.But@cezamat.eu

Here we report on comprehensive investigations of receiving antenna characteristics of monolithically integrated field-effect-transistor-based terahertz detectors with patch antennas which are often used for a variety of applications [1, 2]. Devices are implemented using a standard 65-nm CMOS process technology. Furthermore, we investigate a set of devices coupled to the antenna with same geometrical parameters but connected to a device with a different channel length thus allowing to vary the impedance of antenna load not only through the bias voltage.

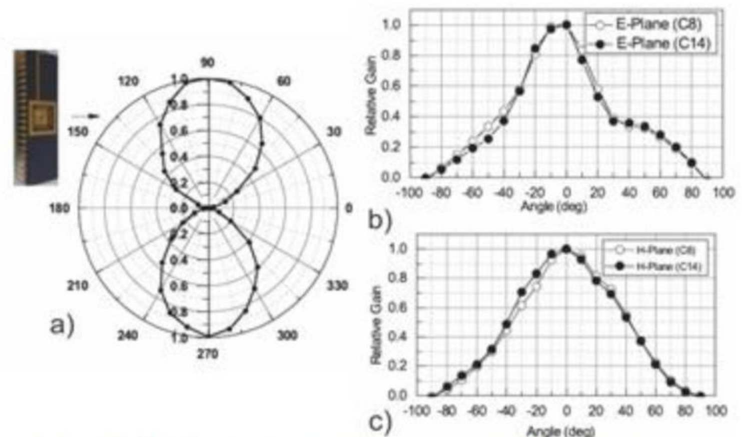

Fig. 1. Dependence of the response of the CMOS on its angular orientation relative to the polarization of the radiation: a) azimuthal, b) vertical or E-plane and c) horizontal or H-plane. Measurements are performed at 0.62 THz.

The directivity values of antennas were determined by measuring the angle dependence of rectified voltage as a function of the tilt in E- and H-planes which are presented in Fig. 1 and through the thorough comparison with the results of electromagnetic simulations using CST software. Considering the amount of input radiation power impinging to the determined effective area of the detector, we report a room-temperature cross-sectional noise-equivalent power of 17.1 pW/√Hz at the resonant frequency of 0.62 THz. This value represents the state of the art for electronic detectors operating at room temperature in this frequency range.

REFERENCES

[1] J. Zdanevicius et al., *IEEE Transactions on Terahertz Science and Technology* **8** .(2018) pp. 613–621.
[2] J. Zdanevičius et al., *Journal of Infrared, Millimeter, and Terahertz Waves* **36** (2015) pp. 986–997.

O17

Phase contrast sub THz imaging and applications

Domas Jokubauskis[1], Linas Minkevičius[1], Liang Qi[1], Agnieszka Siemion[2] and Gintaras Valušis[1]

[1] *Center for Physical Sciences and Technology, Saulėtekio Ave. 3, LT-10257 Vilnius, Lithuania.*

[2] *Faculty of Physics, Warsaw University of Technology, 75 Koszykowa, Warsaw, Poland.*

Email: domas.jokubauskis@ ftmc.lt

Terahertz (THz) imaging becomes a handy tool to identify the contents of various packages [1]. Additional attention is needed when objects have low absorption in THz frequencies. It induces a poor signal-to-noise ratio and small contrast images. To overcome those problems comprehensive imaging techniques is needed [2].

In this contribution, spatial filtering methods – phase contrast and dark field – will be demonstrated both experimentally and theoretically to resolve weakly absorbing objects in THz imaging at 0.3 THz. Imaging was performed using sensitive, working at room temperature, antenna-coupled titanium-based microbolometer [3]. Phase contrast techniques were implemented via employment of two different THz imaging setups – using focused and collimated beams. Figure 1 presents images recorded for 0.3 THz obtained by setup 1 (upper panel) and setup 2 (bottom panel), without and with different spatial filters. Application of phase filters improves the image contrast and allows to discriminate low-absorbing objects from the background and from each other. Also, filtered image enables to resolve nearly transparent objects, to enhance their edges resolution and thus reveal advantage in respect to direct imaging (bright field).

Introduced spatial filtering methods allowed to enhance image contrast up to 30 dB and to increase signal-to-noise ratio by an order of magnitude in detecting weakly absorbing objects. It extends THz imaging applications in biology and medicine, where mostly weakly absorbing objects are under the interest.

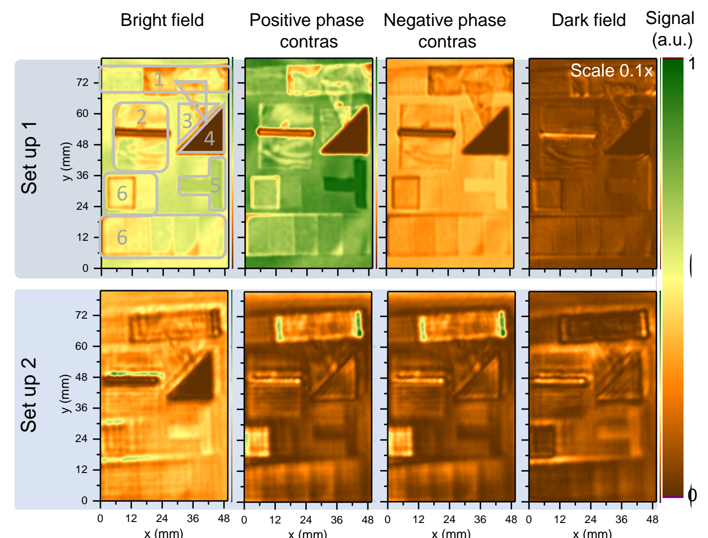

Fig. 1. THz images recorded at 0.3 THz by setup 1 (upper panel) and setup 2 (lower panel), without and with different filters. Contents of the sample are marked by gray squares: (1) - gauze cloth with different number of layers, (2) - a low density polyethylene bag, (3) - piece of a rubber glove, (4) - aluminum foil, (5) - a T-shaped aperture, (6) - paper sheets. THz image pixel size: 0.3 mm x 0.3 mm; images consist of 165 x 273 pixels.

REFERENCES

[1] I. Kašalynas, R. Venckevicius, and G. Valušis, IEEE Sensors J. 13 (2013), pp. 50-54.

[2] M. Wan, J. J. Healy, and J. T. Sheridan, Opt. Laser Technol.122, (2020) pp. 105859

[3] J. Trontelj, G. Valušis, R. Venckevičius, I. Kašalynas, A. Sešek and A. Švigelj; Terahertz Emit. Receiv. Appl. V 9199 (2014) pp. 91990K.

Inv11

Reflectance spectra of selective emitter solar cells in terahertz and sub-terahertz ranges

Mykolas Kiauleikis[1], Linas Minkevičius[2,1], Gintaras Valušis[2,1] and Vincas Tamošiūnas[1,2]

[1]*Institute of Photonics and Nanotechnology, Vilnius University, Saulėtekio av. 3, LT-10257 Vilnius, Lithuania.*
[2]*Department of Optoelectronics, Center for Physical Sciences and Technology, Saulėtekio av. 3, LT-10257 Vilnius, Lithuania*
Email: vincas.tamosiunas@ff.vu.lt.

One of multitude of terahertz (THz) range imaging applications is investigation of solar modules, solar cells and their structures. For example, THz imaging previously was successfully applied to study profiles of contacts on silicon solar cells [1], etched wafers, complete cells and encapsulation materials [2]. In these terahertz-time domain spectroscopy (THz-TDS) experiments, time-of-flight information was used to reveal precise positions of surfaces of interest with sub-wavelength resolution, approaching micron range precision. Simultaneously, small pyramid-like etched structures on the surfaces of silicon (Si) wafers were investigated by studying amplitude information of THz-TDS pulses. Combination of THz-TDS, successive etch-back and numerical calculations can even reveal doping profiles and carrier lifetime within highly doped Si layers of several hundred nm thickness, as it was recently demonstrated by M. Lenz *et. al.* [3].

Silicon solar cells industry also underwent both impressive quantitive and qualitive changes during last decade. These changes include both exponential growth of shipments and dramatic changes to dominating device structures [4]. Once dominating so-called back-surface field (BSF) design with uniform emitter doping is now rapidly being replaced with advanced novel structures based on selective doping technologies. Free carrier absorption and refractive index changes in doped layers are two of the most important mechanisms of interaction between THz radiation and solar cell structures. Therefore, possible novel applications have to be reassessed due to changing (sometimes by orders of magnitude) typical doping levels.

In this contribution, we present simulations of propagation of THz waves within silicon solar cell structures. Novel low-doped selective emitter structures were investigated in series of Finite-Difference Time-Domain (FTTD) simulations. Revealed new potential THz spectroscopy application limits will be discussed. Simulation results were supported by series of measurements.

REFERENCES

[1] L. Minkevičius, R. Suzanovičienė, S. Balakauskas, G. Molis, A. Krotkus, G. Valušis, and V. Tamošiūnas; *Electronics Letters* **48** (2012) pp. 932-934.

[2] V. Tamošiūnas, L. Minkevičius, A. Vaitkūnas, A. Urbanowicz, A. Maneikis, A. Šetkus, and G. Valušis; *Energy Procedia* **77** (2015), pp. 202-207.

[3] M. Lenz, C. Matheisen, M. Nagel, and J. Knoch; *Applied Physics Letters* **110** (2017), p. 072103.

[4] VDMA Photovoltaic Equipment, *International Technology Roadmap for Photovoltaic (ITRPV) – 2019 Results*, 11th ed. (2020).

O18

Effect of lengths, diameters, and density of silver nanowire layers on terahertz conductivity

Aleksandra Przewłoka[1,2], Serguei Smirnov[3], Irina Nefedova[4], Aleksandra Krajewska[1], Igor S. Nefedov[5], Petr S. Demchenko[6], Dmitry V. Zykov[6], Valentin S. Chebotarev[6], Dmytro But[1] Kamil Stelmaszczyk[1] Alvydas Lisauskas[1,7], Joachim Oberhammer[3], Mikhail K. Khodzitsky[6], Wojciech Knap[1], and Dmitri V. Lioubtchenko*

[1]*CENTERA Laboratories, Institute of High-Pressure Physics PAS, Warsaw, Poland.*
[2]*Institute of Optoelectronics, Military University of Technology, 00-908 Warsaw, Poland.*
[3]*Department of Micro and Nanosystems, KTH Royal Institute of Technology, Stockholm, Sweden.*
[4]*Department of Electronics and Nanoengineering, Aalto University, Finland.*
[5]*People's Friendship University of Russia, Moscow, 117198, Russian Federation.*
[6]*THz Biomedicine Laboratory, ITMO University, 197101 Saint Petersburg, Russian Federation.*
[7]*Institute of Applied Electrodynamics and Telecommunications, Vilnius University, Lithuania*
Email: dml@kth.se.

The high-frequency conductivity (0.1 THz to 1.1 THz) of composite nanomaterials is substantially impacted by the lengths, diameters, densities, and thickness of the constituent materials. We have fabricated and experimentally characterized thin layers of silver nanowires in the terahertz frequency range. In particular, the samples of different densities of nanowires and two different nanowire lengths were measured in a transmission geometry by terahertz spectroscopy, both in time and frequency domains. The results obtained in time and frequency domains are in a very good agreement and prove a high reflectance of the metallic nanowire layer. We extracted the conductance, reflectance, transmittance, and absorbance of the samples from the measurements. We have shown that all these characteristics can be tuned by varying the density and geometry of the nanowires. The experimentally observed dependencies were successfully described/fitted by the theory establishing the relation between the nanowire layer structure and the electromagnetic response of the composite. The relatively constant conductance of the nanowire layers in a broad frequency range is of particular interest, as tunable transparent coatings are distinctly demanded for high-frequency applications. Our results pave the way toward the application of silver nanowires as a perspective material for nanoelectronic circuits, transparent and conductive coatings and printable THz antennas, important for future 5G wireless communication systems and above.

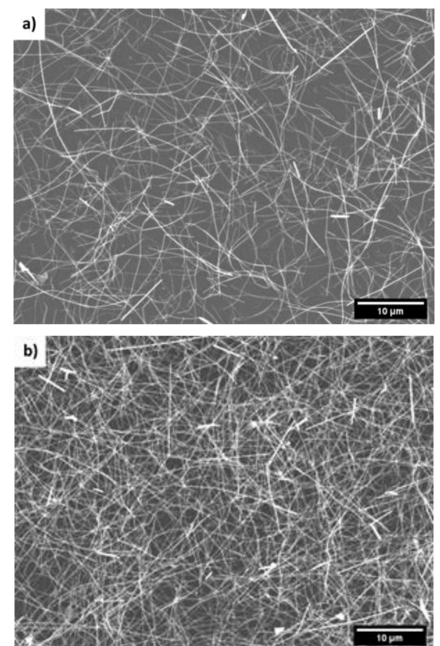

SEM images of AgNWs sample B (35 nm × 25 µm) with **a)** the lowest density – 67 mg/m^2 and **b)** the

O19

Terahertz radiation induced by surface ballistic photogalvanic effect in GaAs LIPSS structures

Ieva Žičkienė, Ramūnas Adomavičius, Arūnas Krotkus, Mindaugas Gedvilas, Mantas Gaidys and Gediminas Račiukaitis

Center for Physical Sciences and Technology, Saulėtekio av. 3, Vilnius, Lithuania.

Email: ieva.zickiene@ftmc.lt

As it is well-known, a transient photocurrent arising near the semiconductor surface, after its illumination with femtosecond laser pulses, can generate terahertz radiation. When analysing this effect, it is generally assumed that the transient photocurrent is directed perpendicular to the illuminated semiconductor surface, along the direction of the surface electric field that is built-in or can be induced by spatial separation of photoexcited electrons and holes. However, the optical alignment of electron momenta (the optical momentum alignment effect in semiconductors manifests itself in the anisotropic momentum distribution of photocarriers excited by linearly polarized light) can result in the appearance of a lateral (parallel to the illuminated semiconductor surface) component of the transient photocurrent.

Recently, we developed a technique for determining the direction of transient photocurrent in a semiconductor [1]. Using this methodology, it was found that upon excitation of p-polarization light, a transient photocurrent component parallel to the surface appears in the GaAs LIPSS structures. This lateral component is very small when exciting the semiconductor near the absorption edge. However, as the excitation photon energy continues to increase, the surface photocurrent grows very rapidly and becomes the dominant source of THz emission (Fig.1). These results suggest that the cause of lateral photocurrent is the ballistic photogalvanic effect [2]. The influence of this effect on THz radiation was mentioned in [3] work, but it has not been observed experimentally so far.

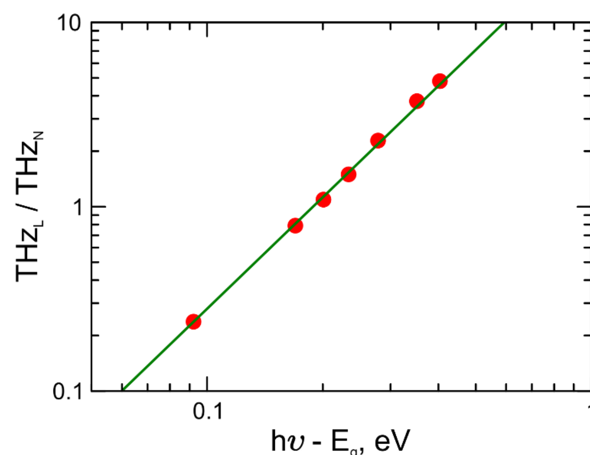

Fig.1 Relative contribution of lateral photocurrent to THz radiation generation. Red circles – experimental results, green line – quadratic dependence. THz_L and THz_N – amplitudes of THz pulses generated by lateral and normal transient photocurrents accordingly.

REFERENCES

[1] I. Beleckaitė and R.Adomavičius, J. Appl. Phys. 125, 225706 (2019)

[2] V. L. Al'perovich et al., Sov. Phys. JETP 53, 1201 (1981)

[3] V. L. Malevich et al., J. Appl. Phys. 112, 073115 (2012)

O20

AlGaN/GaN dual grating gate structures investigated in high magnetic field

P. Sai,[1,3] M. Szoła,[1] D. Yavorskiy,[1,2] D. B. But,[1,3] G. Cywiński,[1,3] M. Sakowicz,[1] M. Dub,[1] P. Prystawko,[1] S. Rumyantsev,[1] J. Łusakowski,[2] W. Knap[1,3,4]

[1]CENTERA Laboratories, Institute of High Pressure Physics PAS, 01-142 Warsaw, Poland
[2]Faculty of Physics, University of Warsaw, ul. Pasteura 5, 02-093 Warsaw, Poland
[3]CEZAMAT, Warsaw University of Technology, 02-822 Warsaw, Poland
[4]Laboratoire Charles Coulomb, University of Montpellier and CNRS UMR, 34950 Montpellier, France

The accurate evaluation of the two-dimensional electron gas (2DEG) parameters in AlGaN/GaN heterostructures is essential for the development of the device based on this materials system, such as high electron mobility transistors, Schottky diodes, THz plasmonic detectors, ultraviolet detectors, piezoelectric and pyroelectric sensors. Cyclotron resonance (CR) and magnetotransport measurements proved themselves as the powerful techniques for 2DEG study in AlGaN/GaN system [1, 2].

We report on high magnetic fields (up to 16 T) magnetotransport, Shubnikov-de-Haas (SdH), CR and photovoltage measurements in AlGaN/GaN high frequency transistors with a dual grating gate (DGG) of large squared area (2×2 mm^2). This kind of DGG device was developed for THz plasmonic detection. Ni/Au grating of symmetric and asymmetric structure was evaporated on AlGaN surface. The epilayer structure for the samples of this study consisted of 1µm-thick undopedGaN and a 25nm-thick undoped AlGaN barrier layer grown on 500µm-thick SiC and bulk GaN substrates using metalorganic chemical vapor deposition (MOCVD).

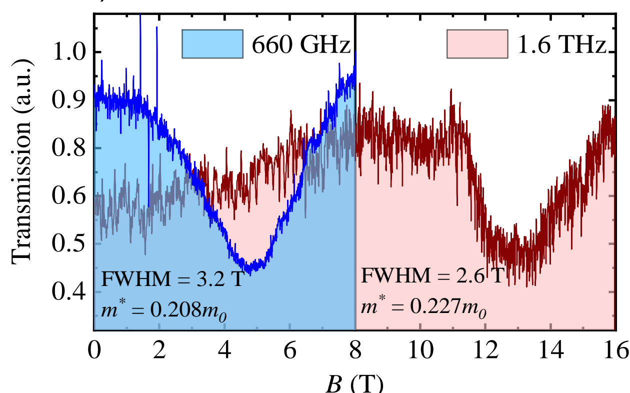

Fig. 1. CR measurements used a VDI source (660GHz) and CO_2 pumped far infrared laser (1.6THz)

The analysis of magnetotransport measurements and SdH oscillations yields information about the carrier concentration and mobility in this channel. Additionally, the transport lifetime (τ_t) was derived using the Drude model and the quantum scattering time (τ_q) was estimated based on the high-magnetic-field part (6-16T) of magnetoresistance longitudinal. The ratio ($\tau_t/\tau_q \approx 5$) indicates a long range character of a disordered potential or may be attributed to a weak inhomogeneity of the 2DEG density.

The CR measurements used a VDI source, CO_2 pumped far infrared laser and 18 T superconducting coil. The results of the experiments are shown in Fig. 1. In this case, two nicely resolved, interference-free lines were found in transmission for the 660 GHz and 1.6 THz incoming radiation frequency. CR measurements allow us to determine the in-plane effective mass of the free electrons.

REFERENCES

[1] Knap, W., et al., Applied Physics Letters. 70(16), 2123-2125 (1997).
[2] Lorenzini, P., et al., Applied Physics Letters. 87(23), 232107 (2005).

O21

Fractional frequencies in microwave response of GaAs/AlGaAs superlattices

Vladislovas Čižas, Liudvikas Subačius, Natalia V. Alexeeva, Dalius Seliuta, Kirill N. Alekseev and Gintaras Valušis

Department of Optoelectronics, Center for Physical Sciences and Technology, Saulėtekio al. 3, Vilnius, Lithuania

Email: vladislovas.cizas@ftmc.lt

Emerging versatile applications of sub-terahertz and terahertz electromagnetic waves stimulate development of miniature, solid-state sources and amplifiers which can operate at room temperature.

Since the pioneer work of Esaki and Tsu [1], semiconductor superlattices attract much attention as unique platform for the studies of various high-frequency effects related to an existence of the negative electron mobility in the band transport.

Parametric generation and amplification at harmonics and low-order sub-harmonics in superlattices, biased by DC and AC electric fields, and the physical processes behind the phenomenon have been rather well understood theoretically ([2,3] and references cited therein). Additionally, there exist a few publications that predict the parametric generation at fractional frequencies [4,5]. To the best of our knowledge neither generation at sub-harmonics nor at fractional frequencies was observed in experiments so far.

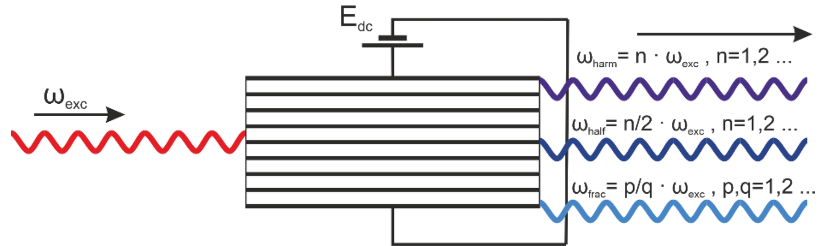

Fig. 1 Sketch of the superlattice frequency response

In this work, we present an analysis of experimental data on the spectral response of moderately doped GaAs/AlGaAs superlattices to a microwave pump (Fig 1). It is shown that the frequencies generated in the superlattice are linked to the pump frequency ω_{exc} by the relations:

$$n\omega_{exc} = \frac{p_1}{q_1}\omega_{exc} \pm \frac{p_2}{q_2}\omega_{exc}$$

where n, $p_{1,2}$ and $q_{1,2}$ are integers. The effects are explained by using the notion of Esaki-Tsu nonlinearities in the superlattice.

REFERENCES

[1] L. Esaki and R. Tsu; *IBM Journal of Research and Development* **14-1** (1970) pp. 61-65.
[2] T. Hyart, A.V. Shorokhov and K.N. Alekseev; *PRL* **98-22** (2007) p. 220404.
[3] T. Hyart, N.V. Alexeeva, A. Leppanen and K.N. Alexeev; *APL,* **89** (2006) p. 132105.
[4] Y.A. Romanov and J.Y. Romanova; *JETP* **91-5** (2000) p. 1033-1045.
[5] J. Isohätälä and K.N. Alexeev, arXiv:1201.6280; Jukka Isohätälä, PhD Thesis, University of Oulu (2012).

O22

All-optical injection and control of currents in carbon films

Petr Obraztsov[1], Yuri Svirko[1] and Kuniaki Konishi[2]

[1]*Institute of Photonics, University of Eastern Finland, PO Box 111, 80100 Joensuu, Finland*
[2]*Department of Physics, University of Tokyo, 7-3-1 Hongo, Bunkyo-ku, 1138656 Tokyo, Japan.*

Strong and broadband light absorption in graphene allows one to achieve high carrier densities essential for observation of nonlinear optical phenomena making graphene a unique playground for studying many-body effects. Being of strong fundamental importance, these effects also open a wide range of opportunities in photonics and optoelectronics. Here, we make use of strong photon-drag effect to generate and optically manipulate ultrafast photocurrents in graphene at room temperature. In contrast to the injection of photocurrents in graphene due to external or built-in electric field [1] and by quantum interference [2], we force the massless charge carriers to move via direct transfer of linear momentum from photons of incident laser beam to excited electrons in unbiased sample [3]. Direction and amplitude of the drag-current induced in graphene are determined by polarization, incidence angle and intensity of the obliquely incident laser beam. We also demonstrate that the irradiation of graphene with two laser beams of the same wavelength offers an opportunity to manipulate the photocurrents in time domain. At the femtosecond excitation, the interplay of the ultrafast photon drag currents enables control of the polarization and amplitude of the THz emission from graphene [4].

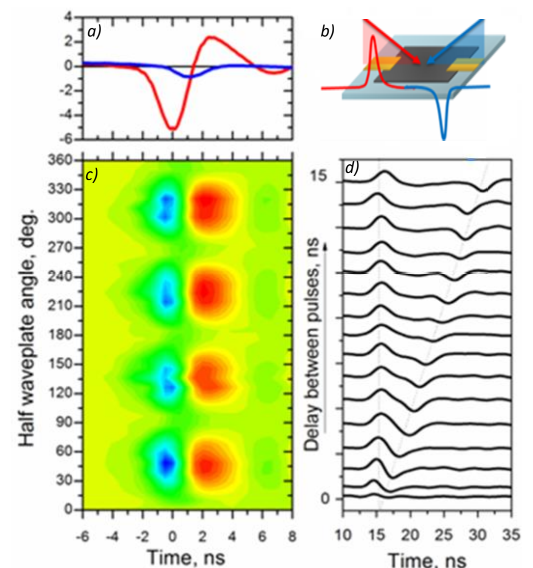

Fig. 1 The photocurrent (a) induced by two 10 ns pulses arriving at the graphene simultaneously at mirror-reflection angles (b) measured as a function of the polarization of the first pulse (c). Two pulses of the same intensity produce currents of opposite sign that cancel one another at zero time delay (d).

All-optical control of photocurrent was demonstrated in the two-beam experiment when sample was irradiated with two mirror-reflected beams (see Fig.1b). At a zero time delay between the excitation pulses of the same intensity, the photocurrents completely compensate each other resulting in a zero net current. Since the drag current strongly depends on the polarization of the excitation beam, the net current was tuned by rotating the polarization plane azimuth of the first beam. The net current signal waveforms as a function of the first beam polarization azimuth obtained at nanosecond excitation is presented in contour plot on Fig.1c.

REFERENCES

[1] L. Prechtel, et al, Nature Communications 3, 646 (2012)
[2] D. Sun et al, Nano Letters 10, 1293 (2010).
[3] P. A. Obarztsov, et al, Sci. Rep. 4, 4007 (2014).
[4] P.A. Obraztsov, Phys. Rev. B 90, 241416(R) (2014)

O23

Studies of Receptor and Its Ligand Interaction Using FRET and TIRF Microscopy

Ernesta Poceviciute[1], Neringa Bakute[1], Marijonas Tutkus[1] and Arunas Stirke[1]

[1] Center for Physical Sciences and Technology, Sauletekio ave. 3, 10257 Vilnius, Lithuania

Email: ernesta.poceviciute@ftmc.lt

An important area in medicine, pharmacy and biotechnology is the study of interacting molecules, which allow the knowledge gained to be used to develop more effective drugs for the treatment of diseases. Most of these studies are in artificial systems, and there is a huge need for models that enable studies of the interaction between biomolecules on the cell surface under natural conditions. The β2-adrenergic receptor (B2ADR) is a widely studied protein, with a particular focus on interactions with various ligands, which is often the starting point for other receptor interactions, but little is known about their interaction. The interaction of the granulocyte colony stimulating factor receptor (GCSFR) with the ligand has been much less studied. Physical methods such as Forster resonance energy transfer (FRET) and total internal reflection fluorescence (TIRF) microscopy enable the study of monomer interactions in the presence or absence of a ligand, changes in receptor monomer interactions following ligand binding in a cell. During the work, the effect of glass coating with poly-l-lysine, APTES, BSA, peptide containing RGD sequence or fibronectin on cell attachment and background signal was investigated. The lowest background signal was found to be achieved by coating the glass surface with fibronectin or 20% NHS-PEG-COOH and 80% NHS-PEG-O-CH_3 and immobilizing at 0,2 mg 44 a.a. length peptide with RGD sequence. Using the FRET method, it has been investigated that β2-adrenergic receptor interactions occur without ligand binding. Also, stimulation with agonist ISO increases the interactions between the receptors and the interacting receptors are internalized after 20 min. stimulation. Inhibition of cell endocytosis increases the number of interacting receptors on the cell membrane, even in the absence of an agonist. By the same method, ligand stimulation for 5 minutes resulted in a 10-fold increase in GCSFR interactions compared to ligand-unstimulated cells. Peak internalization of the complex was observed after 15 minutes of ligand stimulation. The results show similarity between receptors in the ability to interact without ligand binding, and the interaction is seen inside the cell after internalization during long-term incubation with the ligand.

O24
Structure determination of *HEWL* protein aggregates at liquid interfaces

Edvinas Navakauskas[1] and Simona Strazdaitė[1]

Department of Organic Chemistry, Center of Physical Sciences and Technology, Saulėtekis ave. 3, LT-10257 Vilnius
Edvinas.Navakauskas@ftmc.lt

Protein aggregation is associated with more than 30 different human diseases including Alzheimer's, Parkinson's, and others. Each of these diseases is caused by the aggregation of a particular protein and accumulation of aggregates at the cell's membrane. The most recent studies showed that the membrane has an immense effect on protein aggregation and adsorption. Thus, structure characterization at the liquid surfaces, especially at the model Lipid/Water interface, remains a major subject of the protein aggregation research.

Here, we use vibrational sum-frequency generation (VSFG) spectroscopy to understand and compare the structure and adsorption behavior of hen egg-white lysozyme (HEWL) and its aggregates at Air/Water and Lipid/Water interfaces. In addition, we applied Fourier transform infrared spectroscopy and atomic force microscopy (AFM) to verify the structure and the morphology of lysozyme aggregates formed in bulk solution.

In our study, we found that HEWL aggregates with different molecular structures, such as small unordered aggregates, and larger aggregates with a parallel and antiparallel β-sheet structure were adsorbed to both interfaces. We identified that the main driving force for adsorption to the Air/Water interface is hydrophobicity. Meanwhile, adsorption to the Lipid/Water interface is mainly determined by electrostatic interaction between the lipid's headgroups and the charged protein groups, though it is also influenced by hydrophobicity. Moreover, we demonstrate that varying the pH of the solution has a substantial effect on the intensity of VSFG spectra at Lipid/Water, which we attributed to changes in the vibrational dipole orientation of adsorbates.

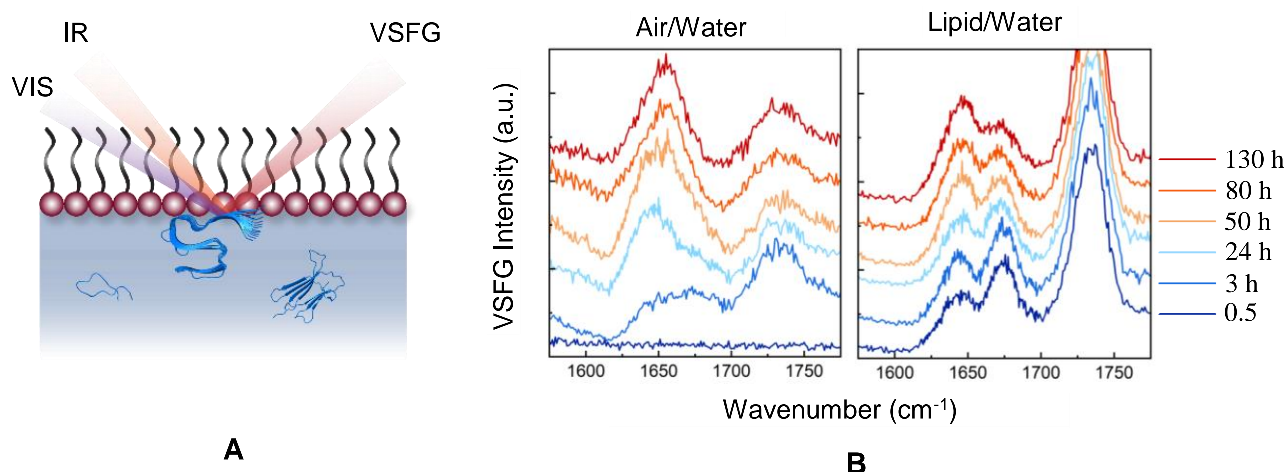

Fig. 1 (A) Schematics of the VSFG experiment **(B)** The VSFG spectra of HEWL and its aggregates adsorbed at different interfaces in Amide I vibrational region. Different spectra correspond to aliquots that were heated for various times (see the legend).

O25

Antimicrobial photodynamic therapy: an alternative to overcome the biofilm resistance.

Wanessa Melo[1], Viktorija Juscenko[1] and Arunas Stirke[1]

[1]*Laboratory of Bioelectric, State Research Institute, Department of Functional Materials and Electronics, Center for Physical Sciences and Technology, Vilnius, Lithuania*

.

Email: wanessa.melo@ftmc.lt.

Currently, the microbial biofilms are responsible for a wide variety of infections in the human body, reaching 80% of all bacterial and fungal infections [1]. The biofilms presents specific properties which increase the resistance to antimicrobial treatments. Thus, the development of new approaches is urgent, and antimicrobial photodynamic therapy (aPDT) have been shown as a promising candidate. aPDT basically involves the synergistic combination of a photosensitizer (PS), molecular oxygen and visible light of appropriate wavelength in order to produce highly reactive oxygen species (ROS), which leads to the oxidation of several cellular components (Fig. 1) [2]. Several studies have demonstrated a substantial biofilm inactivation once the aPDT promotes damage to non-specific target [3-5]. This therapy attack many components of the biofilm, including proteins, lipids, and nucleic acids present within the biofilm matrix; causing the inhibition even in the cells that are inside the extracellular polymeric substance (EPS) [6]. So, the presentation aims to show the progress of aPDT against the biofilms and the several applications of this therapy.

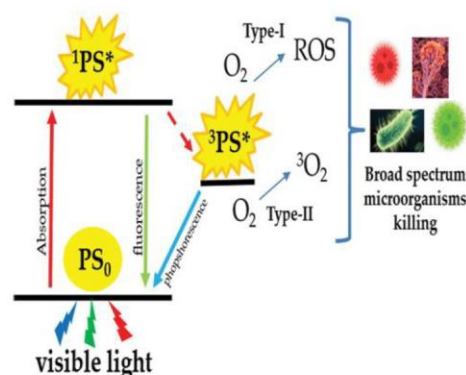

Fig. 1. aPDT mechanism of action

REFERENCES

1. Del Pozo, J.L., *Biofilm-related disease.* Expert Rev Anti Infect Ther, 2018. **16**(1): p. 51-65.
2. Mahmoudi, H., et al., *Antimicrobial Photodynamic Therapy: An Effective Alternative Approach to Control Bacterial Infections.* Journal of lasers in medical sciences, 2018. **9**(3): p. 154-160.
3. Abrahamse, H. and M.R. Hamblin, *New photosensitizers for photodynamic therapy.* Biochem J, 2016. **473**(4): p. 347-64.
4. Rajesh, S., et al., *Antimicrobial photodynamic therapy: An overview.* J Indian Soc Periodontol, 2011. **15**(4): p. 323-7.
5. Hu, X., et al., *Antimicrobial Photodynamic Therapy to Control Clinically Relevant Biofilm Infections.* Frontiers in Microbiology, 2018. **9**(1299).
6. Pinto, R.M., et al., *Innovative Strategies Toward the Disassembly of the EPS Matrix in Bacterial Biofilms.* Frontiers in microbiology, 2020. **11**: p. 952-952.

O26

Ultrafast X-ray techniques applied to solar-cell characterization

Sophie E. Canton[1]

[1]ELI-ALPS, Wolfgang Sandner utca 3, H-6728 Szeged, Hungary.
Email: sophie.canton@eli-alps.hu.

Visualizing on the atomic scale the full extent of the electronic and structural changes that are triggered by charge separation and subsequent charge transport is crucial for developing the rational design of next-generation solar cells. The rapid progress of ultrafast X-ray techniques, both at synchrotrons (100 ps) and at X-ray free electron laser facilities (sub-ps) have equipped the scientific community with novel analytical tools that are capable of delivering unique feedback with spin and elemental sensitivity about the highly-correlated nonadiabatic dynamics that follow photoabsorption. The present talk will review the technical state-of-the art and the ongoing developments that are currently taking place. The talk will also highlight several of the recent results that have been obtained for intramolecular and interfacial processes of relevance for the function and optimization of solar cells.

O27

Luminescent properties of GaAsBi quantum wells

E. Dudutienė[1], A. Jasinskas[1], S. Stanionytė[1] and R. Butkutė[1]

[1]*Department of Optoelectronics, SRI Center for Physical Sciences and Technology, Saulėtekis ave. 3, Vilnius, Lithuania*

Email: evelina.dudutiene@ftmc.lt

Bismide-based material systems are an attractive candidate to develop GaAs-based applications for long wavelength optoelectronics, such as infrared lasers [1], photodetectors [2], solar cells [3], terahertz devices [4] etc. In order, to design and optimize these devices it is essential to know their optical properties, electronic structure, nature of defects, the emission channels, and the efficiency of carrier recombination. In recent years, luminescent properties of GaAsBi quantum wells (QW) are extensively studied. Though, not all questions are clearly answered.

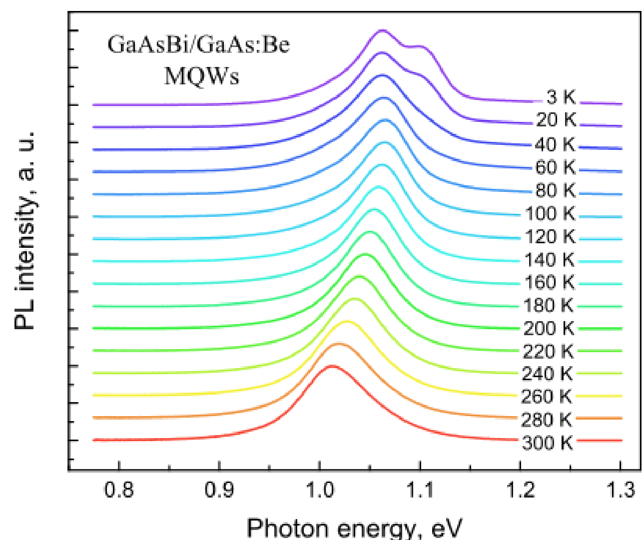

Fig. 1 Temperature-depenedent photoluminescence spectra of GaAsBi/GaAs:Be multiple quantum wells.

This work presents a temperature- and excitation- dependent photoluminescence (PL) study of GaAsBi/GaAs, GaAsBi/AlGaAs and GaAsBi/AlAs QWs grown by molecular beam epitaxy (MBE) and migration enhanced epitaxy (MEE).

Temperature-dependent PL measurements revealed that PL band associated with radiative transitions in GaAsBi QWs has an inner structure, which for some samples can be clearly seen at low-temperatures (Fig. 1). Moreover, temperature-dependence of PL peak energy position was analysed using Varshni expression [5]. A broad PL peak at room temperature together with S-shape character of PL peak position variation with temperature indicated effect of carrier localisation. As further matter, activation energies derived from PL measurements provided insight into thermal quenching of luminescence processes. Finally, the influence of the barrier layer on the optical emission from electronic states in the GaAsBi QWs are also presented in this work.

REFERENCES

[1] X. Wu, et al.; *ACS Photonics* **4**(6) (2018) pp. 1322-1326.

[2] Y. Gu, R. D. Richards, J. P. David, and Y. Zhang; *Dilute Bismide Photodetectors*. In Bismuth-Containing Alloys and Nanostructures, Springer (2019) pp. 299-318.

[3] A. Muhammetgulyyev, O. G. Erbas, B. Kinaci, O. Donmez, Y. G. Celebi and A. Erol; *Semiconductor Science and Technology* **34**(8) (2019) pp. 085001.

[4] M. Karaliūnas, A. Udal and G. Valušis; *Lithuanian Journal of Physics* **60(**2) (2020).

[5] Y. P. Varshni; *Physica* **34**(1) (1967) pp. 149-154.

Poster presentations

P1

Optically pumped semiconductor lasers based on InGaAs/GaAs and GaAsBi/GaAs quantum wells

Algirdas Jasinskas, Simona Pūkienė, Lukas Jočionis, Bronislovas Čechavičius and Renata Butkutė

Center for Physical Sciences and Technology, Saulėtekio av. 3, LT-10257 Vilnius, Lithuania
algirdas.jasinskas@ftmc.lt

Low cost, reliable and compact electrically injected laser diodes have become irreplaceable in fields such as laser pumping, communications, medicine and more [1]. However, for some applications it is more convenient to have laser irradiation come out vertically from the device, rather than from its edge as in the case of laser diodes. More complex vertical cavity lasers exhibit this feature. Moreover, optical pumping of vertical external cavity surface emitting lasers (VECSELs) allows achieving much greater output powers and beam quality while still maintaining wavelength versatility [2]. Essentially, these lasers combine advantages of both semiconductor and solid-state lasers, therefore they are very attractive and in great demand.

In this work, VECSELs of two semiconductor compounds were developed: lasers consisting of multiple InGaAs and GaAsBi quantum well (QW) active regions, both designed for 1.0 - 1.2 μm wavelengths. The structures were optimized for chosen wavelengths by varying the width, number of QWs, as well as barrier and other layer thicknesses. The structures were grown using MBE technology on semi-insulating GaAs substrates with 28.5 period Bragg mirrors pre-deposited on top. All grown laser structures were characterized by reflectivity and room temperature photoluminescence (PL) measurements.

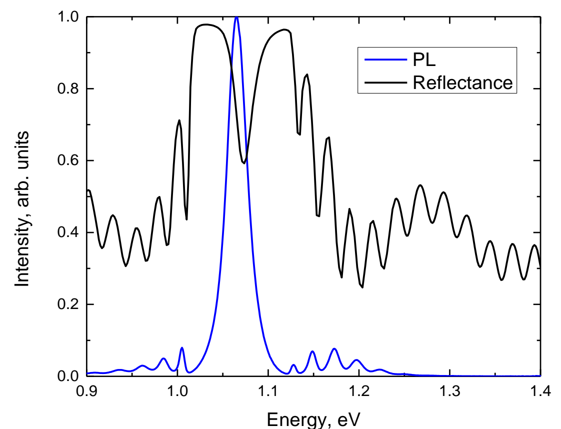

Fig. 1 Reflectance and PL spectra of VECSEL structure with 12 GaAsBi quantum wells.

In the PL spectra (Fig. 1) very intense QW emission lines amplified by the resonant periodic structure of the lasers were observed. Absorption dip at the center of Bragg mirror reflectance spectrum indicated standing electromagnetic wave well-matched with target lasing wavelength from the quantum wells. Structures based on multiple InGaAs/GaAs quantum wells exhibited much higher PL intensities and were found to be much more reliable, however, bismide based structures have the potential to reach longer wavelengths while still using GaAs technological platform.

REFERENCES

[1] D. Patil; *Semiconductor laser diode: technology and applications*, Intech (2012) pp. 217-219.
[2] M. Guina et al., *Journal of Physics D: Applied Physics* **50** (2017).

Optically pumped semiconductor lasers based on InGaAs/GaAs and GaAsBi/GaAs quantum wells

FIZINIŲ IR TECHNOLOGIJOS MOKSLŲ CENTRAS

Algirdas Jasinskas, Simona Pūkienė, Lukas Jočionis, Bronislovas Čechavičius, Ada Gajauskaitė and Renata Butkutė
Center for Physical Sciences and Technology, Saulėtekio av. 3, LT-10257 Vilnius, Lithuania

Apropos 17
2020 September 30 – October 1, Vilnius, Lithuania
algirdas.jasinskas@ftmc.lt

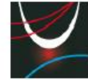

Motivation

Low cost, reliable and compact electrically injected laser diodes have become irreplaceable in fields such as laser pumping, communications, medicine and more [1]. However, for some applications it is more convenient to have laser irradiation come out vertically from the device, rather than from its edge as in the case of laser diodes. More complex vertical cavity lasers exhibit this feature. Additionally, as in the case of vertical external cavity surface emitting lasers (VECSELS) – optical pumping allows achieving much greater output powers and beam quality while still maintaining wavelength versatility [2]. Essentially, these lasers combine advantages of both semiconductor and solid-state lasers, therefore they are very attractive and in great demand.

The goal of this work was to produce and characterize NIR region (1-1.2 µm) optically pumped lasers based on two different gain materials – GaAsBi and InGaAs. The working principle of a VECSEL is shown in Fig. 1. Semiconductor chip with quantum well gain section is mounted on a heatsink and pumped by a diode laser. The resonator cavity is formed by using an external mirror.

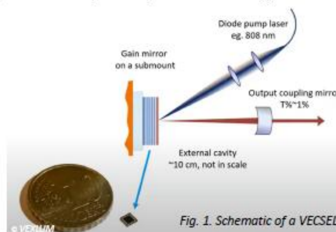

Fig. 1. Schematic of a VECSEL

Sample preparation and characterization

Resonant Periodic Gain (RPG) design (Fig. 2) was used in which a standing electromagnetic wave is formed at lasing wavelength which stimulates quantum well emission. QWs were placed in groups of 2-4 to reduce the overall thickness of the structure and improve thermal properties. Molecular Beam Epitaxy (MBE) equipment was used for growth of the samples. 28.5 period GaAs/AlAs DBR was grown on GaAs substrate, followed by the gain region (QWs and spacers), window layer and capping layer. Photoluminescence (PL), Reflectance and Atomic Force Microscopy (AFM) measurements were performed to characterize the grown lasers.

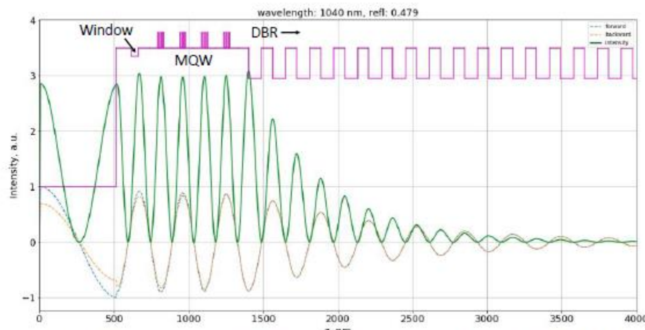

Fig. 2. RPG design of one of the grown VECSEL structures. Purple line represents refractive index profile and green curve – electromagnetic field intensity.

GaAsBi VECSELs

Lasers based on GaAsBi QWs have shown PL in longer wavelengths than InGaAs QWs, however, due to technological challenges associated with GaAsBi MBE growth, it was often difficult to control Bi incorporation precisely and match the QW emission peak with resonant cavity wavelength (sample VGA0385).

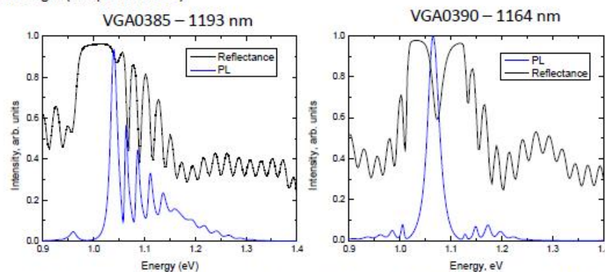

Fig. 3. Reflectance (black curve) and room temperature PL (blue curve) measurements of GaAsBi MQW VECSELS. The central wavelengths of these lasers are 1193 and 1164 nm.

After many growth runs, sample VGA0390 exhibited PL peak at around 1164 nm well matched with the reflectivity dip of cavity resonance.

InGaAs VECSELs

Very similar laser structures were grown by changing QW material from GaAsBi to InGaAs. While using this compound, PL intensity increased by around 3 orders of magnitude and the results were much more reproducible than in the case of bismides.

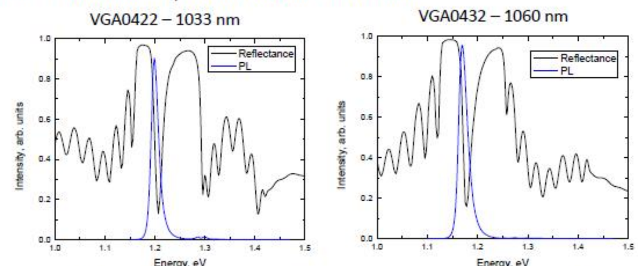

Fig. 3. Reflectance (black curve) and room temperature PL (blue curve) measurements of InGaAs MQW VECSELS. The central wavelengths of these lasers are 1033 and 1060 nm.

Surface quality

AFM measurements have shown dislocations going across all the surface of InGaAs QW samples (VGA0456) due to strain relaxation. While this roughness is very low and gets smoothened as the next VECSEL layers are deposited (VGA0432) this definitely shows, that strain relaxation would be a major issue when trying to reach longer wavelengths with this material.

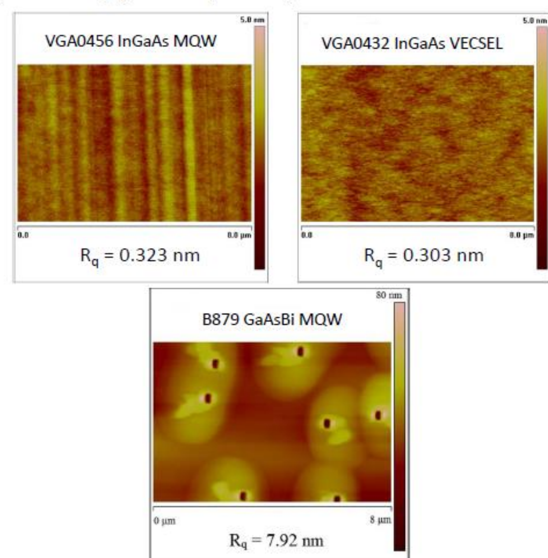

Fig. 9. AFM images and average surface roughness (R_q) of different samples: top left – InGaAs MQW, top right – InGaAs VECSEL, bottom – GaAsBi MQW.

GaAsBi MQW samples, on the other hand, have shown worse overall surface quality (due to extreme growth conditions) which also gets improved as the top VECSEL layers are grown. As expected, no signs of similar dislocations were observed due to more rapid bandgap reduction of bismides.

Conclusions

The grown VECSEL structures are yet to be measured in an optical pumping setup, but the primary characterization revealed high potential of these samples. Reflectivity dip at the center of Bragg mirror indicated standing electromagnetic wave which matched with desired lasing wavelength well and the emission wavelength of the QWs was matched with the resonant wavelength.

Structures based on InGaAs/GaAs quantum wells exhibited much higher intensities and were found to be much more reliable, however, bismide based structures have the potential to reach longer wavelengths while still using GaAs technological platform.

References

[1] D. Patil; Semiconductor laser diode: technology and applications, Intech (2012) pp. 217-219.
[2] M. Guina et al., Journal of Physics D: Applied Physics 50 (2017).

P2

Three components of photovoltage simultaneously induced across GaAs p-n junction

Jonas Gradauskas[1,2], Steponas Ašmontas[1], Algirdas Sužiedėlis[1], Aldis Šilėnas[1], Aurimas Čerškus[1,2], Viktoras Vaičikauskas[1], Oleksandr Masalskyi[2] ,Ovidijus Žalys[1]

[1]*Center for Physical Sciences and Technology, Lithuania.*
[2]*Vilnius Gediminas Technical University, Lithuania.*
jonas.gradauskas@ftmc.lt

In this communication we demonstrate that photovoltage induced by a 1.06 μm laser pulse across GaAs p-n junction is composed of three components resulting from hot carrier, lattice heating, and electron-hole pair generation phenomena. The first one is very fast and shows polarity of thermoelectromotive force of hot carriers. The second one, resulting from thermalisation of hot carriers, has the same polarity and is slower. The third one, respectively, is the classical photovoltage arising due to two photon absorption [1] with polarity opposite to that of the first two. Our model assumes p-n junction as a first-order linear time-invariant (LTI) system, and the time-response of it in a general case is characterized by the differential equation

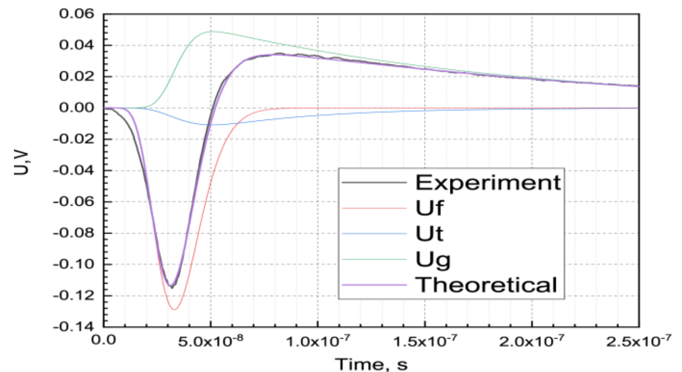

Fig. 1 Experimental photoresponse (black); its components due to hot carriers (red), thermalisation (blue), generation (green), and their sum (violet).

$$\tau\frac{dU}{dt} + U = \bar{U}(t), \qquad (1)$$

where $\bar{U}(t)$ is the forcing function depending on the laser pulse and on the physical phenomenon giving rise to particular photovoltage component, and τ is the experimentally estimated time constant typical of each component. Fig. 1 shows all three components, their sum and the experimental photovoltage trace. Good agreement between the experimental and calculated results is achieved.The components demonstrate different dependencies on the laser intensity and bias voltage.The proposed model enables revealing contribution of each component to the net magnitude of the photovoltage and can open the way in reducing the negative impact of hot carriers into the photovoltage of a solar cell.

REFERENCES

[1] W.C. Hurlbut, Y.-S. Lee, K.L. Vodopyanov, P.S. Kuo, M.M. Fejer. *Opt. Lett.* 32 (2007) pp. 668-670.

CENTER FOR PHYSICAL SCIENCES AND TECHNOLOGY

VILNIUS GEDIMINAS TECHNICAL UNIVERSITY

Three components of photovoltage simultaneously induced across GaAs p-n junction

Jonas Gradauskas[1,2], Steponas Ašmontas[1], Algirdas Sužiedėlis[1], Aldis Šilėnas[1], Aurimas Čerškus[1,2], Viktoras Vaičikauskas[1], Edmundas Širmulis[1], Ovidijus Žalys[1], Oleksandr Masalskyi[2]

jonas@pfi.lt

[1]*Center for Physical Sciences and Technology, Vilnius, Lithuania*

[2]*Vilnius Gediminas Technical University, Vilnius, Lithuania*

Apropos 17 Advanced Properties and Processes in Optoelectronic Materials and Systems

INTRODUCTION

According to the Shockley-Queisser theory, only photons having energy hν close to a semiconductor forbidden energy gap E_g are used effectively for electrical power generation. Lower energy photons are assumed as not absorbed at all, while the residual extra energy of higher energy photons is reckoned in only through the process of carrier thermalization.

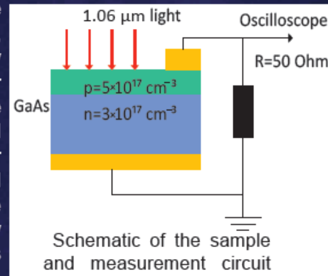

Schematic of the sample and measurement circuit

There again, hot carriers can be generated by the infrared radiation ("not absorbed at all") as well as by the photons supplying the mentioned extra residual energy. And the intraband light absorption has been demonstrated to rise a hot carrier photoemf across a semiconductor p-n junction illuminated with a CO_2 laser (hν=1.17 meV) radiation [1,2]. The photoemf had polarity opposite to that of the classical carrier generation-induced emf.

We present experimental evidence of direct hot carrier influence on the net photovoltage formation across a semiconductor p-n junction. As an object of investigation, GaAs (E_g=1.42 eV) p-n junction was illuminated with 25 ns-long laser pulses of 1.06 μm wavelength (hν=1.17 eV).Such experimental assortment allowed to investigate simultaneous rise of the hot carrier photovoltage andthe classical photovoltage resulting from carrier generation due to two-photon absorption [3,4].

RESULTS. THREE PHOTOVOLTAGE PULSES

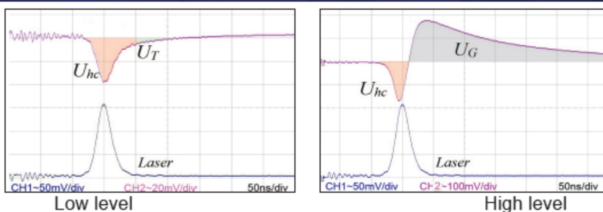

Low level High level

Experimental traces of photovoltage across GaAs p-n junction at different excitation levels. No bias voltage is applied.

Simultaneous rise of hot carrier U_{hc} (reddish area) and carrier generation-induced U_G (bluish area) photovoltages is obvious. Thermalization-caused component U_T (green area) can be seen following the U_{hc} in the case of low excitation level

RESULTS. PHOTORESTONSE

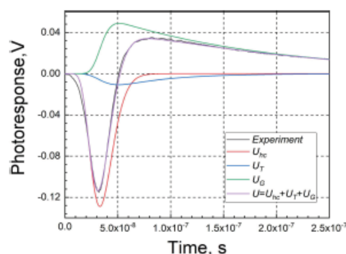

Photoresponse across GaAs p-n junction at moderate excitation level

Experimental photoresponse (black); its components due to hot carriers (red), thermalisation (blue), generation (green), and their sum (violet)

RESULTS. BOTH PHOTOVOLTAGES vs INTENSITY

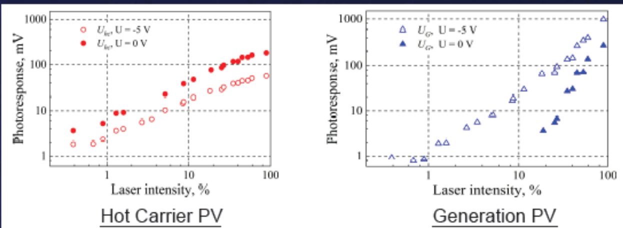

Hot Carrier PV Generation PV

Dependence of hot carrier photovoltage U_{hc} (red dots) and generation-induced photovoltage U_G (blue dots) across GaAs p-n junction on laser intensity at zero bias (solid dots) and -5 V of reverse bias voltage (open dots)

The reverse bias voltage acts against the hot carrier photovoltage formation.

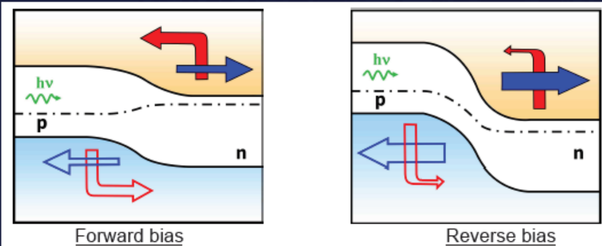

Forward bias Reverse bias

Schematic description of hot carrier (red arrows) and generation-induced (blue arrows) photocurrents as forward and reverse bias voltage is applied. Hollow arrows stand for flows of holes

CONCLUSIONS

- In general, photoresponse in a p-n junction consists of three simultaneous components induced by:
  - ✓ electron-hole pair generation,
  - ✓ hot carriers,
  - ✓ lattice heating after thermalisation.
- Hot carrier photovoltage across a p-n junction
  - ✓ is evidenced experimentally,
  - ✓ rises prior to the thermalization,
  - ✓ opposes the classical generation-induced photovoltage.
- Forward bias voltage increases the input of the hot carrier photovoltage.
(*How does the classical photovoltage bias a p-n junction*?)
- Hot carrier photovoltage may be the reason of still unattainable Schockley-Queisser limit.

ACKNOWLEDGMENT

This work was in part supported by the Research Council of Lithuania (grant No. 01.2.2-LMT-K-718-01-0050).

REFERENCES

1.S. Ašmontas, J. Gradauskas, D. Seliuta, E. Širmulis. Photoelectric properties of nonuniform semiconductor under infrared laser radiation. Proc. SPIE4423, 18–27 (2001).
2.F. Encinas-Sanz, J.M. Guerra. Laser-induced hot carrier photovoltaic effects in semiconductor junctions. Progress in Quantum Electronics 27, 267 (2003).
3.S. Ašmontas, J. Gradauskas, A. Sužiedėlis, A. Šilėnas, E. Širmulis, V. Švedas, V. Vaičikauskas, and O. Žalys, Appl. Phys. Lett. 113, 071103 (2018).
4.J. Gradauskas, S. Ašmontas, A. Sužiedėlis, A. Šilėnas, V. Vaičikauskas, A. Čerškus, O. Žalys, O. Masalskyi.Unfolding hot carrier impact in photovoltage across a p-n junction. Journal of Appl. Phys. (in press)

P3

Bismide-based Intersubband devices for Mid-Infrared Applications

Karolis Stašys[1], Ričardas Norkus[1], Sandra Stanionytė[1] and Jan Devenson[1]

[1]*Center for Physical Sciences and Technology, Sauletekio av. 3, LT-10257, Vilnius, Lithuania.*
Email: karolis.stasys@ftmc.lt.

Intersubband devices such as Quantum cascade lasers (QCLs) are considered now as standard light sources for many chemical sensing applications in the mid-infrared above 4 µm. Performances of diode lasers rapidly degrade below 3 µm due to fundamental limitations such as increasing influence of nonradiative Auger recombination. But this obstacle can be resolved by using bismides materials such as InAsBi/Al(As)Sb and InGaAsBi/AlAsSb in QCL superlattices structure [1,2].

To achieve functional bismide-based intersubband devices, first of all the development of molecular beam epitaxy (MBE) procedure for the growth of InAsBi/Al(As)Sb and InGaAsBi/AlAsSb superlattices, which will be suitable for integration as active quantum wells into InAs/Al(As)Sb and InGaAs/AlAsSb injectors in Quantum Cascade Laser structures must be developed. As a first step, in order to find appropriate growth conditions for $In_{0.7}Ga_{0.3}As_{1-x}Bi_x$ layers a set of samples have been grown on InP substrates at different growth temperatures varying As/Ga and As/Bi flux ratios. All grown samples had smooth surface and exhibited decent incorporation of bismuth. X-Ray measurement results are shown in Figure 1.

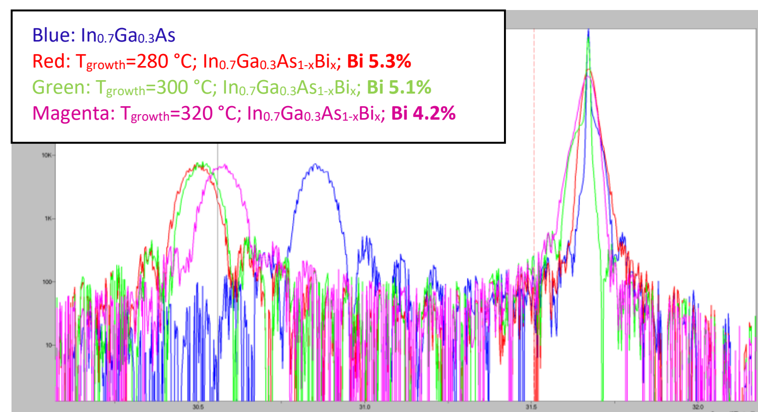

Fig. 1. Measured high resolution X-Ray diffraction curves of InGaAsBi samples grown at different.

The MBE growth technique for the epitaxy of InAsBi/Al(As)Sb and InGaAs/AlAsSb quantum wells has been developed. Bismuth containing superlattices exhibited excellent interface contrast and crystalline quality. Obtained growth conditions can be considered as suitable for the growth of Bismide-based intersubband devices.

REFERENCES

[1] R Butkute, A Geižutis, V Pačebutas. B Čechavičius, V Bukauskas, V Kondrotas, P Ludewig, K Volz, A Krotkus; Electronics Letters. 50. 1155–1157. 10.1049/el.2014.1741, 2014

[2] K. Alberi, J. Wu, W. Walukiewicz, K. M. Yu, O. D. Dubon, S. P. Watkins, C. X. Wang, X. Liu, Y.- J. Cho, and J. Furdyna.;. Phys. Rev. B, 75:045203, 2007

Bismide-based Intersubband devices for Mid-Infrared Applications

Karolis Stašys[1], Ričardas Norkus[1], Sandra Stanionytė[1] and Jan Devenson[1]
[1]*Center for Physical Sciences and Technology, Sauletekio av. 3, LT-10257, Vilnius, Lithuania.*
Email: karolis.stasys@ftmc.lt

FIZINIŲ IR TECHNOLOGIJOS MOKSLŲ CENTRAS

Abstract:
Intersubband devices such as Quantum cascade lasers (QCLs) are considered now as standard light sources for many chemical sensing applications in the mid-infrared above 4 μm. Performances of diode lasers rapidly degrade below 3 μm due to fundamental limitations such as increasing influence of nonradiative Auger recombination. But this obstacle can be resolved by using bismides materials such as InAsBi/Al(As)Sb and InGaAsBi/AlAsSb in QCL superlattices structure [1,2]. In this work the MBE growth technique for the epitaxy of InAsBi/Al(As)Sb and InGaAs/AlAsSb quantum wells has been developed. Bismuth containing superlattices exhibited excellent interface contrast and crystalline quality. Obtained growth conditions can be considered as suitable for the growth of Bismide-based intersubband devices.

Main goal and challenges:
The main goal is the development of molecular beam epitaxy (MBE) procedure for the growth of InAsBi/Al(As)Sb and InGaAsBi/AlAsSb superlattices, which will be suitable for integration as active quantum wells into InAs/Al(As)Sb and InGaAs/AlAsSb injectors in Quantum Cascade Laser structures. There are two steps for each material system associated with the growth of such structures: 1) epitaxy of low temperature grown bismuth containing superlattices and 2) integration of low temperature grown bismide superlattices into high temperature grown superlattices – 4 stages in overall.
The challenge is that the main difference between these two material systems is that despite compositional similarity these two material systems are dedicated for the growth on different substrates – InAsBi/Al(As)Sb on InAs substrates, while InGaAsBi/AlAsSb on InP substrates. InAs/Al(As)Sb can be considered as lattice matched system while InGaAsBi/AlAsSb is strain balanced and more complicated for the growth. Advantage of the InAs-based system is that it has larger conduction band offset, thus, better carrier confinement, slightly lower electron effective mass, and also entire laser structure can be grown in the same process as no overgrowth is needed. InP based system mainly takes an advantage of better InP thermal conductivity. [3]

MBE growth of InGaAsBi/AlAsSb on (100) InP substrates:
As a first step, in order to find appropriate growth conditions for $In_{0.7}Ga_{0.3}As_{1-x}Bi_x$ layers a set of samples have been grown on InP substrates at different growth temperatures varying As/Ga and As/Bi flux ratios. All samples were grown using solid source Veeco GEN Xplor molecular beam epitaxy (MBE) system, equipped with SUMMO group III element sources, Veeco As and Sb valved cracker sources and conventional Dual Filament bismuth source. The substrate temperature was controlled by a thermocouple (TC) and kSA BandIT broadband pyrometry module. The kSA 400 Reflection High-Energy Electron Diffraction (RHEED) system was used for in-situ surface characterisation. Each substrate prior to be loaded into the growth chamber has been outgassed at 200 °C in the load lock and later at 300 °C in the buffer chamber. The thicknesses of InGaAs buffer layers in samples varied from 100 nm to 270 nm depending on observation of RHEED pattern quality to decide if buffer layers is sufficiently smooth. All the samples were grown at the ~0.5 monolayer/s growth rate. InGaAsBi layers were grown at temperatures, which are commonly used for the growth of ternary bismide alloys: 280 ˚C, 300 ˚C, and 320 ˚C. To ensure that only temperature will have an influence, the Bi/InGa ratio was kept the same. All grown samples had smooth surface and exhibited decent incorporation of bismuth. X-Ray measurement results are shown in Figure 1.
Samples grown at lower temperature have higher amount of incorporated bismuth. However, samples grown at temperatures 280 ˚C (5.3% Bi) and 300 ˚C (5.1% Bi) have difference of only 0.2% while the amount of incorporated bismuth in sample grown at 280 ˚C dropped to 4.2%. Moreover, it seems that the layer grown at 300 ˚C has better crystalline quality, as it has sharper main peak and visible fringes around bismide corresponding peak. Therefore, the temperature of 300 ˚C was stated to be the optimal temperature for the growth of InGaAsBi layers.

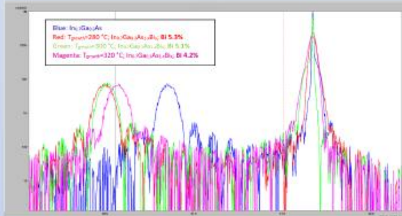

Fig. 1. Measured high resolution X-Ray diffraction curves of InGaAsBi samples grown at different temperatures

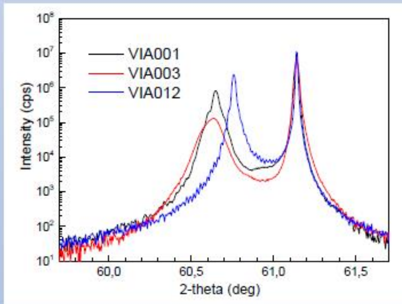

Fig. 2. XRD (004) rocking curves measured on three InAsBi samples VIA001, VIA003, and VIA012.

MBE growth of InAsBi/AlAsSb on (100) InAs substrates:
In difference with InGaAsBi/AlAsSb material system, the InAs/Al(As)Sb system is considered as nearly lattice matched to the substrate. Hence easier calibration and adjustment procedures are needed. On the other hand, this material system quite close in composition to the first one. Hence, in similarity, initial bismide growth conditions were found in the same way. The optimal growth temperature of InAsBi material has been determined by the As cap desorption temperature, which occurs at nearly 300 ˚C. Each substrate prior to be loaded into the growth chamber has been outgassed at 200 °C in the load lock and later at 300 °C in the buffer chamber. The native oxide removal was performed at 525 – 530 °C temperature according to the pyrometer readings and under ~1×105 Torr beam equivalent pressure (BEP) As_2 flux. After that the substrate temperature was decreased to 500 – 515 °C for InAs buffer layer growth. RHEED oscillation measurements were performed to estimate the growth rate of InAs and III/V ratios prior to the growth of InAsBi layers. InAsBi layers in all samples were grown at 320 °C temperature according to the thermocouple readings. Thicknesses of below presented grown InAsBi layers in samples VIA001, VIA003, VIA012 are respectively 390 nm, 400 nm, and 500 nm. All the samples were grown at the 0.5 monolayer/s growth rate. The bismuth content in InAsBi layers was determined from the X-ray diffraction (XRD) (004) rocking curves. XRD traces obtained on all three InAsBi samples are presented in Figure 5. Flattened top of InAsBi peak of VIA012 suggests the possible layer relaxation due to higher bismuth concentration. To prove that (115) Reciprocal Space Maps (RSM) of two InAsBi samples with the largest 2θ shifts from the substrate were registered and are presented in Figure 6. Two strong peaks can be clearly distinguished on these maps: the upper peak can be associated with the InP substrate, the lower one with the InAsBi layer, red lines on the maps correspond to fully strained and fully relaxed states and the blue line shows different relaxation states with the same Bi content. It can be seen from this figure that InAsBi layer with lower Bi content (Fig. 6a) grown on InAs substrate is strained, whereas InAsBi layers with higher Bi content have a relaxation level of 40%. The composition of all InAsBi layers and other parameters are given in Table 1.

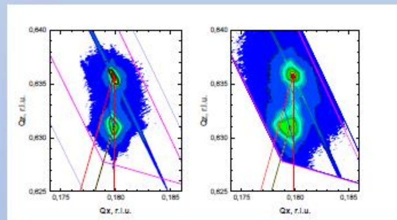

Fig. 3. Reciprocal Space Maps (RSM) of two InAsBi samples: VIA003 (a) and VIA012 (b). The red lines on the maps correspond to fully strained and fully relaxed lattice states and the blue line indicates the states with the same Bi content and different relaxation levels.

Sample	Bi concentration, %	Relaxation, %	Thickness, nm
VIA012	2.7	0%	390
VIA001	3.6	0%	400
VIA003	4.55	40%	480

Table 1. Main parameters of the investigated samples.

Conclusions:
The MBE growth technique for the epitaxy of InAsBi/Al(As)Sb and InGaAs/AlAsSb quantum wells has been developed. Bismuth containing superlattices exhibited excellent interface contrast and crystalline quality. Obtained growth conditions can be considered as suitable for the growth of Bismide-based intersubband devices. Measured intervalley scattering confirmed that incorporation of Bi into the quantum well can reduce carrier escape to lateral valley.
Using developed growth technique and optimized growth conditions the InAsBi/AlAsSb intersubband emission structure has been grown. The electroluminescence spectrum has been obtained from fabricated EL structure. Emission wavelength peak in vicinity of 3.3 μm has been recorded. This confirmed that there is no degradation in performance associated with insertion of Bi and further design modifications are possible to exploit advantage of Bi in quantum wells for development of short wavelength intersubband devices.

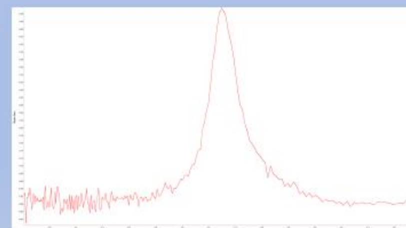

Fig. 4. EL emission spectrum obtained from InAsBi/Al(As)Sb sample.

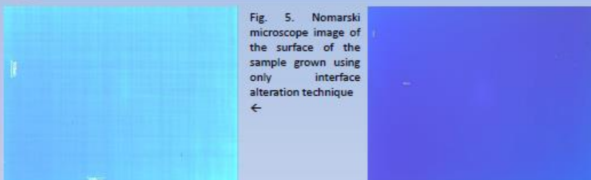

Fig. 5. Nomarski microscope image of the surface of the sample grown using only interface alteration technique ←

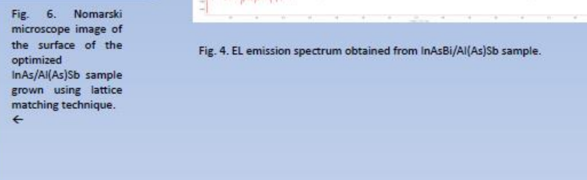

Fig. 6. Nomarski microscope image of the surface of the optimized InAs/Al(As)Sb sample grown using lattice matching technique. ←

Sources:
[1] R Butkute, A Geižutis, V Pačebutas. B Čechavičius, V Bukauskas, V Kondrotas, P Ludewig, K Volz, A Krotkus; Electronics Letters. 50. 1155–1157. 10.1049/el.2014.1741, 2014
[2] K. Alberi, J. Wu, W. Walukiewicz, K. M. Yu, O. D. Dubon, S. P. Watkins, C. X. Wang, X. Liu, Y.- J. Cho, and J. Furdyna.;. Phys. Rev. B, 75:045203, 2007
[3] J. Devenson. InAs/AlSb SHORT WAVELENGTH QUANTUM CASCADE LASERS. Dissertation, 2010.

P4

Determination of electron drift velocity from hot-electron effect in ZnO epilayers and AlGaN/GaN heterostuctures

Oleg Kiprijanovič[1] and Linas Ardaravičius[2]

[1]Department of Functional Materials and Electronics, [2]Department of Fundamental Research, Center for Physical Sciences and Technology, Saulėtekio av. 3, Vilnius LT-10257, Lithuania.
Email: linas.ardaravicius@ftmc.lt.

Zinc oxide (ZnO) and Gallium nitride (GaN) are semiconductors with a direct and relatively wide bandgap. A high expected electron velocity saturation in ZnO and GaN [1] is promising to field-effect transistors for high-frequency and high-power operations. High experimental electron drift velocity (~2.7x10^7 cm/s at 320 kV/cm) was reported at room temperature in undoped ZnO epilayers [2].

In this work, the investigated ZnO epilayers and AlGaN/GaN heterostructures were grown at Virginia Commonwealth University (USA). The electron transport measurements up to high electric fields were carried out on the two-electrode samples selected from the transmission line measurement patterns. The employment of few nanosecond voltage pulses allowed us to minimize the channel self-heating effect. Pulsed current–voltage measurements used voltage pulse widths down to 3 ns and achieved electric fields up to 430 kV/cm in undoped ZnO. The densities of charged defects (~10^{17} cm^{-3}) were estimated through comparison of the differential conductivities measured at the low and the moderate electric fields. The experimental data on the current together with the estimated scattering on the charged defects were used for estimation of the electron drift velocity in ZnO in other way: ~2.9x10^7 cm/s at the electric field of 320 kV/cm and the electron density of 1.5x10^{17} cm^{-3} (Fig. 1, stars). The hot-electron effect based method described in Ref. [2] was applied to estimate electron drift velocity in AlGaN/GaN heterostructures. The calculated differential mobility of 180 cm^2/Vs [3] was used for calibration and the highest value of ~3.5x10^7 cm/s at 300 K and 130 kV/cm electric field was obtained (Fig. 1, squares). Similar highest electron velocity in a GaN two-dimensional electron gas channel was obtained by Monte Carlo simulation [4].

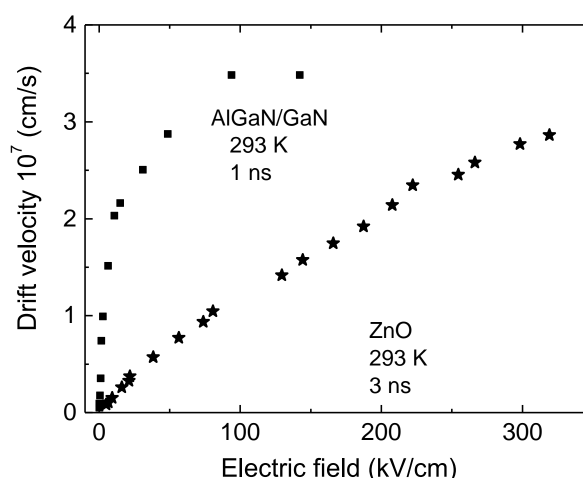

Fig.1. Experimental room temperature electron drift velocity versus the applied electric field in ZnO epilayers (stars) and AlGaN/GaN heterostructures (squares). Voltage pulse duration 1-3 ns. Electron density: 1.5x10^{17} cm^{-3} (stars), 3.1x10^{12} cm^{-2} (squares).

REFERENCES

[1] W. A. Hadi, M. S. Shur, and S. K. O'Leary; *J. Mater. Sci.:Mater. Electron.* **25**, (2014) pp. 4675-4713.

[2] L. Ardaravičius, O. Kiprijanovič, M. Ramonas, E. Šermuksnis, J. Liberis, A. Šimukovic, A. Matulionis, Md. B. Ullah, K. Ding, V. Avrutin, U. Ozgur, and H. Morkoc; *J. Appl. Phys.* **126**, (2019) pp. 185703.

[3] L. Ardaravičius, A. Matulionis, J. Liberis, O. Kiprijanovič, M. Ramonas, L. F. Eastman, J. R. Shealy, and A. Vertiatchikh; *Appl. Phys. Lett.* **83**, (2003) pp. 4038-4040.

[4] T.-H. Yu and K. F. Brennan: *J. Appl. Phys.* **91**, (2002) pp.3730-3736.

Determination of electron drift velocity from hot-electron effect in ZnO epilayers and AlGaN/AlN/GaN heterostructures

Oleg Kiprijanovič and Linas Ardaravičius

Email:linas.ardaravicius@ftmc.lt

APROPOS 17, Vilnius, Lithuania 2020/09/30

Zinc oxide (ZnO) is a semiconductor with a direct and relatively wide bandgap. High electron drift velocity saturation (3.2×10^7 cm/s) was attained from Monte Carlo calculations [1] and recent experimental findings of the drift velocity (~2.7×10^7 cm/s at 320 kV/cm) and electric fields (430 kV/cm) were reported for nominally undoped ZnO epilayers at room temperature [2]. These results are promising to field-effect transistors (FETs) for high-frequency and high-power operations. The dependence of electron drift velocity on the electron density was deduced at room temperature for doped ZnO [3].

The electron low-field mobility in ZnO is mainly determined by scattering on charged defects. There is an experimental evidence that double charged oxygen vacancies act as shallow donors and charged scattering centres. The goal of this work is to examine the electron scattering by charged defects through the study of hot-electron effects in nominally undoped ZnO epilayers at room temperature. The current–voltage dependence is measured up to high electric fields, and the experimental results are fitted with the solution of the Boltzmann kinetic equation [4]. The results are used for the estimation of electron density, drift velocity and low-field mobility. The electron scattering by the double-charged oxygen vacancies and other charged defects is discussed.

As a promising candidate for future high-electron-mobility transistors (HEMTs) used in microwave high-power applications, GaN-based heterostructure two-dimensional electron gas (2DEG) channels have attracted much interest [5]. The insertion of a thin AlN spacer layer prevents electron penetration into adjacent AlGaN layer and simultaneously improves the sheet charge density and mobility compared with the conventional AlGaN/GaN heterostructure having equivalent AlGaN parameters. Our goal is to extract the key transport parameter – the electron drift velocity.

[3] L. Ardaravičius, O. Kiprijanovič, J. Liberis, M. Ramonas, E. Šermukšnis, A. Matulionis, M. Toporkov, V. Avrutin, U. Özgur, and H. Morkoç, *Mater. Res. Express* **4**, 066301 (2017).
[5] A.S.A. Fletcher and D. Nirmal, Superlattices and Microstructures **109**, 519-537 (2017).

Drift velocity, gate length, and cut-off frequency in FET

Effective carrier saturation velocity in a field-effect transistor

L_g – gate length

f_T – current gain cut-off frequency

$$v_s = 2\pi f_T L_g$$

Carrier drift velocity and Pulsed dc technique

$$v_d = \frac{I}{enw}$$

I - current, e – elementary charge, n – carrier density, w- sample cross section area (width)

AlGaN/GaN HEMT: A. Vertiatchikh et al., WOCSDICE (2003) & ISCS (2003) **DOI:** 10.1109/ISCSPC.2003.1354444 v_s = 1.1x10⁷ cm/s; ZnO FET: S. Sasa et al., Phys. Stat. Sol. A **208,** 449 (2011); f_T = 1.75 GHz

Maximum electron drift velocity in ZnO

The highest experimental electron velocity value is close to the peak value obtained by Monte Carlo simulation [1]. Highest experimental room temperature electron drift velocity in nominally undoped ZnO at 320 kV/cm: $v_{drmax} = 2.7 \pm 0.3 \times 10^7$ cm/s [2]. Electrical pulses of few nanoseconds (3 ns) in duration were used. Experimental results up to moderate electric fields are in good agreement with theoretical calculations by spherical harmonics expansion (SHE) method.

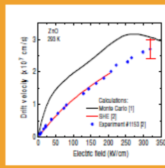

[1] J. D. Albrecht, P. P. Ruden, S. Limpijumnong, W. R. L. Lambrecht, and K. F. Brennan, J. Appl. Phys **86**, 6864 (1999).
[2] L. Ardaravičius, O. Kiprijanovič, M. Ramonas, E. Šermukšnis, J. Liberis, A. Šimukovič, A. Matulionis, Md. B. Ullah, K. Ding, V. Avrutin, Ü. Özgür, and H. Morkoç, J. Appl. Phys. **126**, 185703 (2019).

Electron density $n_0 = \sigma_0/e\mu_0 = 1.9 \times 10^{17}$ cm^{-3} (circles); 1×10^{17} cm^{-3} (solid lines [1]).

Differential mobility, conductivity, and effective defect density

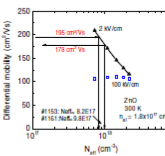

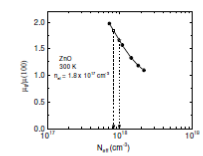

Calculated differential mobility ratio at low (2 kV/cm) and moderate (100 kV/cm) electric fields, $\mu_0/\mu(100)$, versus the total charged defect density N_{eff} is compared with the ratio of conductivities, $\sigma_0/\sigma(E_m)$, obtained from the experiment [4]:

$$\frac{\mu_0}{\mu(E_m)} = \frac{\sigma_0}{\sigma(E_m)} = 1.84$$

Drift velocity in AlGaN/AlN/GaN and ZnO

For higher low-field electron mobility (1880 cm²/(Vs)) AlN-spacer containing structure electron drift velocity saturates and attains the value of 1.6×10^7 at 95 kV/cm. The highest electric field reached is 140 kV/cm. At this particular field, both drift velocity values in epitaxial ZnO and 2DEG GaN channel are similar.

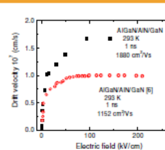

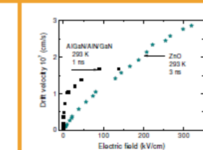

[6] L. Ardaravičius, A. Matulionis, J. Liberis, O. Kiprijanovic, M. Ramonas, L.F. Eastman, X. Chen, Sun Yun-Ju, *Physica Status Solidi (a)*, vol. **202** , 808-811, 2005.

Intentionally undoped ZnO samples

The investigated epitaxial ZnO layers were grown in Virginia Commonwealth university (USA) by (PA-MBE) on highly-resistive GaN prepared by MOCVD on c-plane sapphire. ZnO epilayer width *w* = 300 μm and thickness *d* = 350-375 nm. The transmission line measurement (TLM) patterns were processed with evaporated Ti/Au (25 nm/30 nm) stacks acting as ohmic contacts. The contact resistance (R_c = 23±10Ω) was estimated at low electric fields from the dependence of the sample resistance on the inter-electrode distance (*L* = 1.7-15.8 μm). The channel resistance, the length and the cross section area were used to estimate the low-field conductivity. Electron mobility in the channel was estimated from Hall effect and magnetoresistance measurement data. More oxygen-rich conditions as well as lower substrate temperature during the growth (340° C) gave rise to lower electron density.

Sample	#1153(#1161)
Epilayer conductivity σ_0	4.7(5.5) S/cm
Magnetoresistance electron mobility	188(146) cm²/(Vs)
Electron drift mobility μ_0	195(178) cm²/(Vs)
Electron density n_0	1.5(1.9)x10¹⁷ cm⁻³
Hall electron mobility	53(50) cm²/(Vs)
Oxygen vacancy density	1.6(1.9)x10¹⁷ cm⁻³
Other charged defect density	1.7(2.0)x10¹⁷ cm⁻³

$$n(E_m) = \frac{\sigma(E_m)}{e\mu(E_m)} = n_0 = \frac{\sigma_0}{e\mu_0}$$

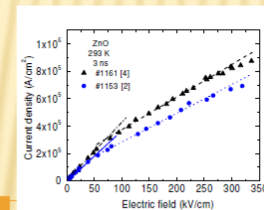

Experimental current density-electric field (*j-E*) results for ZnO can be approximated with lines:

E < 50 kV/cm: A solid line and dashed dotted lines stand for the Ohm's law.

50 kV/cm < *E* = E_m < 250 kV/cm: Dashed and dotted lines with a lower slope illustrates the second Ohm's law

$\sigma(E_m)$ - differential conductivity at E_m can be found from the slope of *j-E* curve:

$$\sigma(E_m) = \frac{dj}{dE}(E_m)$$

AlGaN/AlN/GaN 2DEG channel

The heterostructures were grown in Virginia Commonwealth university (USA) by MOCVD on c-sapphire substrates. The 2DEG channel formed in the top-most portion of 3.2 μm-thick GaN layer. Transmission-line measurement (TLM) patterns with mesa etching were fabricated with the electrode dimensions of 300x80 μm² and the gaps from 3 to 27 μm. The magnetoresistance measurements were performed on the TLM structures. The contact resistance R_c was evaluated from the TLM length-dependent resistance measurements; the values were found to be much lower compared to the resistance of the 6.9 μm length channel. The Hall mobility and the TLM-evaluated resistance value were also utilized simultaneously for estimation of the sheet 2DEG density.

Sample	#4338
Channel conductivity σ_0	1.6 mS
Magnetoresistance electron mobility	1700 cm²/(Vs)
Hall sheet electron density	8.6x10¹² cm⁻²
TLM sheet electron density	5.2x10¹² cm⁻²
Hall electron mobility	1880 cm²/(Vs)

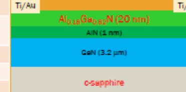

Experimental setup for measurements of sub-nanosecond pulsed current-voltage (I-U) dependence

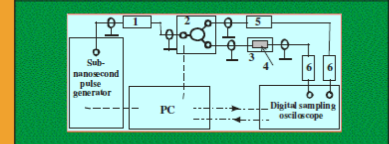

1 - high-voltage attenuator, 2 - wide-band switch, 3 - sample holder, 4 - sample under test, 5 - reference resistor, 6 - tunable wide-band attenuator.

L. Ardaravičius, O. Kiprijanovič, J. Liberis, A. Matulionis, E. Šermukšnis, R. A. Ferreyra, V. Avrutin, Ü. Özgür, and H. Morkoç, *Semicond. Sci. Technol.* **30,** 105016 (2015).

Transient current and electric field measurements

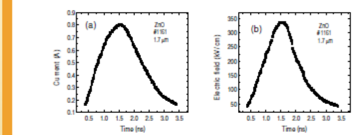

The transmitted current (a) and electric field (b) waveforms for the ZnO sample #1161. The highest current of 0.8 A corresponds to 320 kV/cm peak field at 26 dB attenuation. The current deduced during the rise edge nearly coincides with that available from the falling edge. The coincidence suggests that neither the sample temperature nor the electron density change with time and electric field.

[4] L. Ardaravičius, O. Kiprijanovič, M. Ramonas, E. Šermukšnis, A. Šimukovič, and A. Matulionis, *Lithuanian J. Phys.* **60**, 48-56 (2020).

Drift velocity in ZnO and Zn cell temperature

The highest experimental value for the electron drift velocity of ~2.9×10^7 cm/s (~2.7×10^7 cm/s) is found at 320 kV/cm in the sample #1153 (#1161) with the electron density of 1.5×10^{17} cm^{-3} (1.9×10^{17} cm^{-3}). A correlation with the growth conditions is resolved: a slightly higher drift velocity is estimated for the sample #1153 with a lower density of oxygen vacancies. This wafer has been grown at lower Zn cell temperature (340 °C). The highest drift velocity value is close to that obtained from Monte Carlo calculations [1].

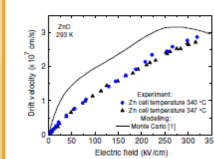

Electron density $n_0 = \sigma_0/e\mu_0 = n(E_m) = \sigma(E_m)/e\mu(E_m) = 1.5(1.9) \times 10^{17}$ cm^{-3} circles(triangles);
1×10^{17} cm^{-3} (solid line [1]).

Acknowledgments

Authors are thankful to Dr. E. Šermukšnis and Prof. A. Matulionis from Center for Physical Sciences and Technology, Lithuania, for discussion and Prof. H. Morkoç group at Virginia Commonwealth University (USA) for ZnO and nitride samples.

P5

Optical properties of GeSi/Si quantum dots in mid- and far-IR range

Roman M. Balagula[1], Anton N. Sofronov[2], Hayk A. Sarkisyan[3], and Dmitry A. Firsov[2]

[1]Optoelectronics Department, Center for Physical Sciences and Technology, Saulėtekio al. 3, LT-10257, Vilnius, Lithuania.

[2]Institue of Physics, Nanotechnology, and Telecommunications, Peter the Great St. Petersburg Polytechnic University, Polytechnicheskaya str., 29, 195251, St.Petersburg, Russia.

[3]Department of General Physics and Quantum Nanostructures, Russian Armenian University, 123 Hovsep Emin Str., Yerevan, 0051, Armenia

Email: roman.balagula@ftmc.lt.

Quantum dots (QDs) are extensively studied owing to their discrete energy spectrum allowing for flexible control of optical and electrical properties and possibility of embedding in various semiconducting media for realization of optical interconnections [1]. Efficient photodetectors and radiation emitters can be realized utilizing either interband or intersubband carrier transitions in these objects [2].

Optical and photoelectric properties of self-organized GeSi quantum dots MBE-grown in a Si matrix were investigated in this study utilizing polarization-resolved equilibrium and photoinduced absorption and photoconductivity measurements in mid- and far-IR regions allowing to determine energy spectrum of localized states in the QDs. The dependence of observed transitions on the doping and external interband excitation was analyzed. The peculiar lack of changes in far-IR absorption spectra with increase in the number of holes localized in the QDs was attributed to the specific QD geometry allowing for the adiabatic description of the confining potential. Thus, the observed effect is deemed to be an experimental confirmation of generalized Kohn's theorem applicability to such objects [3].

Difference in temperature dependence of equilibrium and photoinduced interband absorption was observed. The proposed explanation is based on the difference of carrier diffusion lengths that are limited by the dopant δ-layers and are approximately equal to bipolar carrier diffusion length in silicon in case of doped and undoped samples, respectively.

The temperature dependence of the photoinduced absorption kinetics in undoped QDs is studied experimentally. A model based on rate equations used to describe the underlying processes of carrier relaxation is developed taking into account complex band structure arising owing to the built-in strain.

The obtained results can be applied further for development of quantum dot infrared photodetectotors.

REFERENCES

[1] V. A. Yuryev and L. V. Arapkina, *Nanoscale Res. Lett.* **6** (2011) p. 522.

[2] A. I. Yakimov, *et al.*, *Opt. Express* **25** (2017) pp. 25602-25611.

[3] F. Peeters, *Phys. Rev. B* **42** (1990), pp. 1486–1487.

Optical properties of GeSi/Si quantum dots in mid- and far-IR range

Roman M. Balagula[1], Anton N. Sofronov[2], Hayk A. Sarkisyan[3], and Dmitry A. Firsov[2]

[1] Center for Physical Sciences and Technology, Vilnius, Lithuania
[2] Peter the Great St. Petersburg Polytechnic University, St. Petersburg, Russia
[3] Russian-Armenian University, Yerevan, Armenia

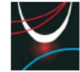

Apropos 17
Advanced Properties and Processes in Optoelectronic Materials and Systems
29 September – 01 October, 2020

1. Samples: high-density array of Ge/Si quantum dots

Sb-mediated MBE-growth

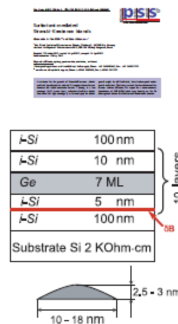

Growth temperature = 600°C
Dot material – Ge_xSi_{1-x} ($x = 0.6 \ldots 0.65$)
Dot surface density = 2×10^{11} cm^{-2}

Doping	Holes per dot
0	0
4×10^{11} cm^{-2}	2
8×10^{11} cm^{-2}	4
1.2×10^{12} cm^{-2}	6

Sample geometry for optical measurements

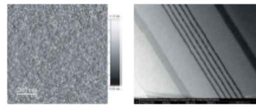

2. Mid-IR optical absorption

Equilibrium

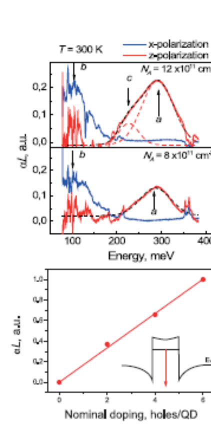

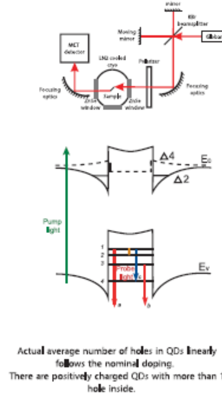

Actual average number of holes in QDs linearly follows the nominal doping.
There are positively charged QDs with more than 1 hole inside.

Photoinduced

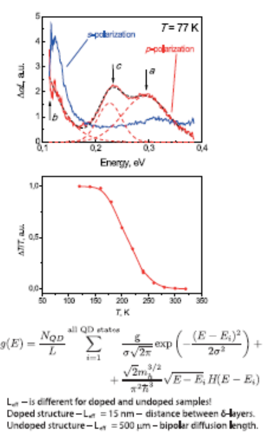

$$g(E) = \frac{N_{QD}}{L} \sum_{i=1}^{\text{all QD states}} \frac{g}{\sigma\sqrt{2\pi}} \exp\left(-\frac{(E-E_i)^2}{2\sigma^2}\right) + \frac{\sqrt{2} m_h^{3/2}}{\pi^2 \hbar^3} \sqrt{E-E_i}\, H(E-E_i)$$

L_{eff} – is different for doped and undoped samples!
Doped structure – L_{eff} = 15 nm – distance between δ-layers.
Undoped structure – L_{eff} = 500 µm – bipolar diffusion length.

3. Far-IR optical absorption

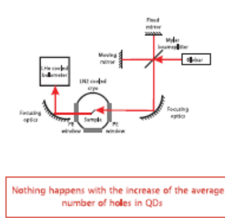

Nothing happens with the increase of the average number of holes in QDs

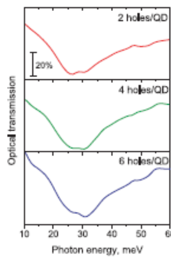

Energy of transitions to low excited levels does not depend on the number of holes in QDs

For multiparticle states this effect is observed in parabolic potential:
In magnetic field W. Kohn Phys. Rev. 123, 1242 (1961)
In "parabolic" QDs – P.A. Maksym, T. Chakraborty Phys. Rev. Lett. 65,108 (1990), F.M. Peeters Phys. Rev. B 42, 1486(R) (1990)

4. Model: Lens-shaped Ge/Si QD

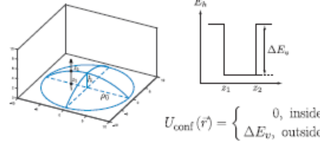

$$U_{\text{conf}}(\vec{r}) = \begin{cases} 0, & \text{inside}, \\ \Delta E_v, & \text{outside}. \end{cases}$$

5. Where is a parabolic potential in "rectangular-band-profile" QD?

Adiabatic separation of hole motion in xy-plane and along z-axis: $\rho_0 >> h$

According to D.B. Hayrapetyan, E.M. Kazaryan, and H.A. Sarkisyan. Physica E, 75, 353 (2016)

$$\hat{H}_0\Psi + U_{\text{conf}}\Psi = \mathcal{E}\Psi \qquad \Psi(\rho,\varphi,z) = f(\vec{\rho})\chi(z(\rho))$$

$$\Delta E_v \gg \hbar\omega:$$

At fixed ρ the hole is confined along z in 1D infinite well of width $z_2 - z_1 = a(\rho)$

$$a(\rho) = \sqrt{R^2-\rho^2} - (R-h)$$

$$\chi_n(z(\rho)) = \sqrt{\frac{2}{a(\rho)}} \sin\left(\frac{\pi n}{a(\rho)} z\right)$$

$$\mathcal{E}_n^{(z)} = \frac{\pi^2\hbar^2 n^2}{2m(a(\rho))^2} = U_n^{\text{eff}}(\rho)$$

if $\rho << \rho_0$: Hole confinement potential in xy–plane

$$U_n^{\text{eff}}(\rho) = \frac{\pi^2\hbar^2 n^2}{2mh^2} + \frac{m\Omega_n^2}{2}\rho^2$$

$$\Omega_n^2 = \frac{\pi^2\hbar^2 n^2}{m^2 h^3 R}$$

6. From single-particle to many-particle problem

$$\hat{H}(1,2,\ldots N) = \sum_{j=1}^{N} \hat{H}_0^j + \sum_{j=1}^{N} U_{\text{conf}}(\vec{r}_j) + V(\vec{r}_1,\ldots \vec{r}_N)$$

Adiabatic separation: $\Psi(\vec{r}_1,\ldots \vec{r}_N) = f(\vec{\rho}_1,\ldots \vec{\rho}_N)\chi_{n_1\ldots n_N}(z_1(\rho_1),\ldots z_N(\rho_N))$

$$n_1 = \ldots = n_N = 1$$

$$V = \frac{1}{2}\sum_{\substack{i,j=1\\ i\neq j}}^{N} \frac{e^2}{\varepsilon|\vec{\rho}_i - \vec{\rho}_j|} \qquad \hat{H}^{2D} = \frac{1}{2m}\sum_{j=1}^{N}\left(\hat{P}_{xj}^2 + \hat{P}_{yj}^2\right) + \frac{m\Omega_1^2}{2}\sum_{j=1}^{N}\rho_j^2 + \frac{1}{2}\sum_{\substack{i,j=1\\ i\neq j}}^{N} \frac{e^2}{\varepsilon|\vec{\rho}_i - \vec{\rho}_j|}$$

Changing variables from ρ_j to CM motion and relative motion of the particles:

$$\vec{R}_{CM} = \frac{1}{\sqrt{N}}\sum_{j=1}^{N}\vec{\rho}_j \qquad \hat{H}^{2D} = \hat{H}_{CM}^{2D} + \hat{H}_{Rel}^{2D} = -\frac{\hbar^2}{2M}\frac{d^2}{dR_{CM}^2} + \frac{M\Omega^2}{2}R_{CM}^2 + \hat{H}_{Rel}^{2D}$$

The EM wave perturbation operator in dipole approximation

$\Delta\hat{H} = e\vec{E}(t)\sum_j \vec{\rho}_j = \sqrt{N}e\vec{E}(t)\vec{R}_{CM}$ depends on only CM coordinate.

Single-particle-like optical transitions in many-particle system are observed.

Optical absorption at the lowest intelevel resonance does not depend on the Coulomb interaction and number of holes inside the QD.

Transition energy $\hbar\Omega = \dfrac{\pi\hbar^2}{m\sqrt{h^3 R}}$

For the largest QDs in ensemble h ≈ 2.95 nm, ρ_0 ≈ 9 nm, and $\hbar\Omega$ ≈ 31 meV

7. Far-IR optical absorption at higher temperatures

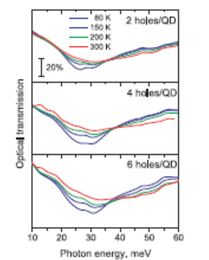

Redistribution of the holes over the smaller QDs in ensemble depends on the nominal doping

8. Mid-IR photoinduced absorption dynamics

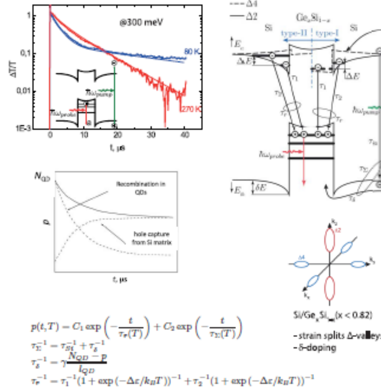

Si/Ge_xSi_{1-x}(x < 0.82)
- strain splits Δ-valleys
- δ-doping

$$p(t,T) = C_1\exp\left(-\frac{t}{\tau_r(T)}\right) + C_2\exp\left(-\frac{t}{\tau_\Sigma(T)}\right)$$

$$\tau_\Sigma^{-1} = \tau_{Si}^{-1} + \tau_s^{-1}$$

$$\tau_s^{-1} = \gamma\frac{N_{QD} - p}{l_{QD}}$$

$$\tau_r^{-1} = \tau_1^{-1}(1+\exp(-\Delta\varepsilon/k_B T))^{-1} + \tau_2^{-1}(1+\exp(-\Delta\varepsilon/k_B T))^{-1}$$

From temperature dependences of characteristic times we find ΔE = 25 meV and δE = 70 meV

Conclusions

1. Equilibrium and photoinduced absorption in GeSi QDs related to intersubband hole transitions are investigated.

2. The effect of thermal depopulation of the GeSi/Si quantum dots at temperatures below 300 K is observed in photoinduced absorption of undoped samples when the bipolar diffusion of charge carriers is not restricted.

2. Equilibrium absorption depends on doping differently in mid-IR and FIR optical regions.

3. Kohn's theorem applicability to such structures was experimentally shown.
- There is a certain energy range where the motion of the holes in Ge/Si quantum dots is equivalent to the motion of 2D particles in parabolic potential.
- The analytical size-quantization theory developed for holes in Ge/Si QDs on the basis of the adiabatic approximation gives good agreement with the experimental energy of the lower intraband resonance.
- The resonance frequency does not depend on the interaction between holes and is of a single-particle character.
- The conditions for generalized Kohn's theorem are satisfied due to the specific geometric shape of the QDs.

4. The existence of potential barrier for holes at the heterointerface and its influence on optical properties was experimentally proven.

5. First investigation of photoinduced absorption dynamics in QD structures was performed. Two stage behavior of absorption relaxation is qualitatively explained.

e-mail:roman.balagula@ftmc.lt

P6

In-situ SHINERS analysis of SAM from thiols with imidazole ring and intrachain amide groups

Agnė Zdaniauskienė[1], Tatjana Charkova[1], Rita Sadzevičienė[1], Gediminas Niaura[1]

[1]*Department of Organic Chemistry, Center for Physical Sciences and Technology, Saulėtekio Ave. 3, LT-10257 Vilnius, Lithuania*

Email: agne.zdaniauskiene@ftmc.lt

The self-assembled monolayers (SAMs) constructed by the adsorbtion of thiols on noble metals are widely used to analyze the interaction of functional groups with adsorbates, study electron transfer processes and develop bioelectronic devices [1].

Introduction of amide functionality in the hydrocarbon chain of adsorbing molecules considerably increases the stability of the formed SAMs due to the formation of hydrogen bonds between the adjacent molecular chains in the monolayer [2]. A terminal histidine (His) ring group containing monolayers provide a possibility to study various interactions of the ring with solution components. The unique structure of His makes it play multiple roles in the molecular interactions - it is an important ligand for metal coordination in peptides and proteins [3].

Shell-isolated nanoparticle-enhanced Raman spectroscopy (SHINERS) method employs the ultrathin shell to isolate the metal nanospheres from the probed object and thus prevents a potentially disturbing interaction. Meanwhile, the very short metal–molecule separation can still result in a significant nanoparticle-enhanced Raman signal [4].

The present work focused on *in situ* SHINERS study of SAM formed from N-(2-(1H-imidazol-4-yl)ethyl)-6-mercaptohexanamide (IMHA) at smooth Au surface in aqueous solutions. SHINERS method employing synthesized spherical Ag nanoparticles with 85 ± 5 nm core size and SiO_2 shell of 3 nm thickness allowed to obtain significantly enhanced SHINERS spectrum of IMHA compared to the Raman spectrum (Fig. 1). Bands from all parts (terminal imidazole ring, hydrocarbon chain, and sulfur group) of IMHA are clearly visible.

Therefore, it was shown that SHINERS is a perspective technique allowing the collection of molecular level information from smooth Au surface for a better understanding of molecular structures and functions.

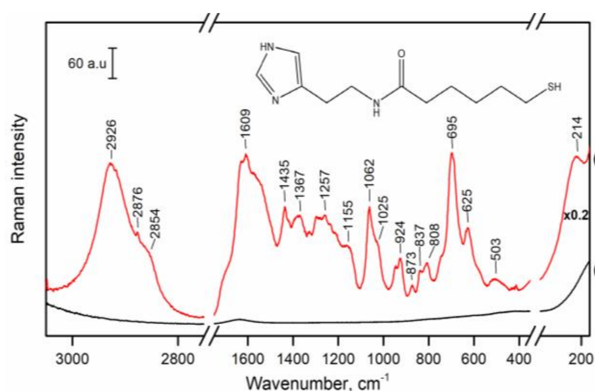

Fig. 1 Raman spectrum of IMHA adsorbed on smooth Au surface **(a)** and SHINERS spectrum from smooth Au surface with adsorbed IMHA **(b).**

REFERENCES

[1] J. C. Love, L. A. Estroff, J. K. Kriebel, R. G. Nuzzo, G. M. Whitesides; *Chem. Rev.* **105** (2005) pp. 1103–1170.

[2] M. Kim, J. N. Hohman, A. C. Serino, P. S. Weiss; *J. Phys. Chem. C* **114** (2010) pp. 19744–19751.

[3] S. M. Liao, Q. S. Du, J. Z. Meng, Z. W. Pang, R. B. Huang; *Chem. Cent. J.* **7** (2013).

[4] J.R. Anema, J.F. Li, Z.L. Yang, Ren B, Z.Q. Tian; *Annu. Rev. Anal. Chem.* **4** (2011) pp. 129–150.

P7

Polarity sensors based on thiophene-substituted BODIPY molecular rotors

Karolina Maleckaitė[1], Jelena Dodonova[2],
Sigitas Tumkevičius[2], Aurimas Vyšniauskas[1]

[1] *Center for Physical Sciences and Technology, Saulėtekio av. 3, Vilnius, Lithuania*
[2] *Institute of Chemistry, Faculty of Chemistry and Geosciences, Vilnius University, Naugarduko str. 24, Vilnius, Lithuania*
Email: karolina.maleckaite@ftmc.lt

Imaging viscosity at a microscopic scale can provide information about the diffusion-controlled processes in biosystems. The changes in viscosity can be an indicator of the development of atherosclerosis, diabetes, and Alzheimer's disease [1]. One of the easiest ways to image viscosity is provided by viscosity-sensitive fluorophores termed 'molecular rotors'. One of the most promising molecular rotors are BODIPY (Fig. 1A). It is possible to achieve longer, more biocompatible wavelengths by adding thiophene group moieties, which increases the conjugated system and shows a larger Stokes shift. [2]

In this work, we investigate two thiophene-substituted BODIPY molecular rotors with (**BP-N**) and without (**BP-T**) $-NO_2$ group (Fig. 1B). In this case, adding thiophene moieties in 2- and 6- BODIPY positions increases molecule's conjugation and redshifts fluorescent spectra to more biologically-friendly wavelengths. The investigation consists of absorption and fluorescence spectra measurements, as well as fluorescence lifetime evaluation in many different solvents. Spectrometry results showed that connecting a nitro group shifts absorbance and fluorescence spectra to lower energies. Moreover, it increases the Stokes shift and shortens the fluorescence lifetime (Fig. 1C).

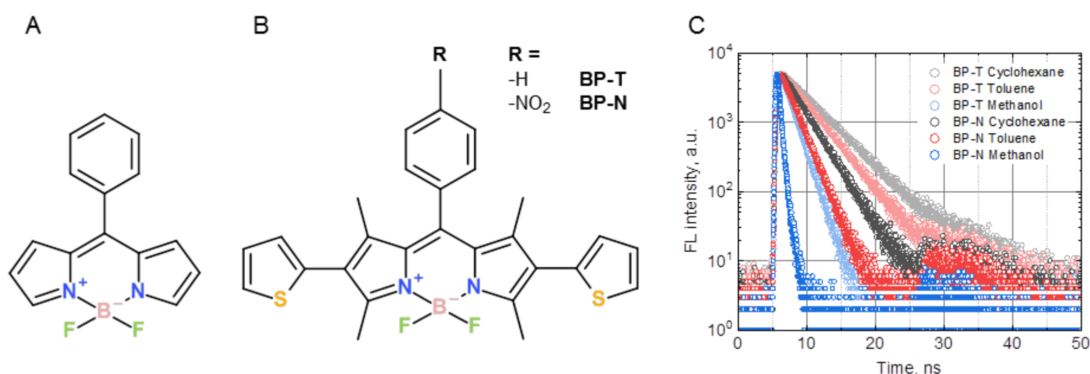

Fig. 1. The molecular structures of the widely used phenyl substituted BODIPY (A) and molecular rotors examined in this work (B). Fluorescent lifetimes of BP-T and BP-N in different solvents (C).

REFERENCES

[1] M. K. Kuimova, Phys. Chem. Chem. Phys. vol 14, no 37, p. 12671, 2012.
[2] Y. Chen et al., J. Org. Chem. vol. 77, 5, p. 2192-2206, 2012.

Polarity sensors based on thiophene-substituted BODIPY molecular rotors

Vilnius University

Karolina Maleckaitė[1], Jelena Dodonova[2], Sigitas Tumkevičius[2], Aurimas Vyšniauskas[1]

karolina.maleckaite@ftmc.lt

Background

- Easy way to image viscosity is provided by viscosity-sensitive fluorophores - **molecular rotors.** [1]
- **BODIPY based** molecular rotors are very promising because of their easy functionalization, high molar extinction coefficients, monoexponential fluorescence lifetime and photostability. [2]
- A recent research has showed that attached **thiophene moieties** to the BODIPY core **can rotate** and this suggests that these derivatives **could be sensitive to viscosity.** [3]
- In this work two **thiophene-substituted** BODIPY molecular rotors with (**BDP-N**) and without (**BDP-T**) -NO_2 group are investigated.

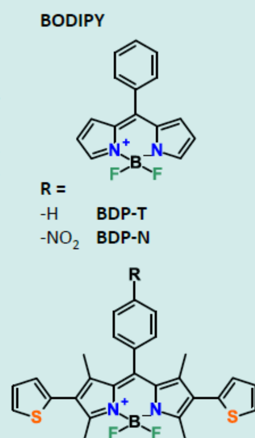

Thiophene impact

- Attaching thiophene moieties to BODIPY increases the conjugated system.
- Longer, **more biocompatible wavelengths** are achieved as well as a **larger Stokes shift** in contrast to BODIPY.

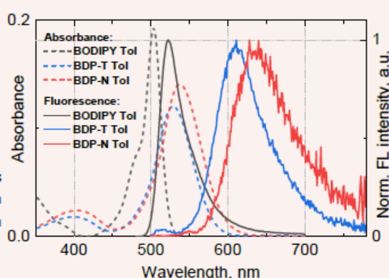

Viscosity impact

- Fluorescence spectroscopy measurements show negligible distinction between lifetimes when solvent viscosity is increased.
- **BDP-T and BDP-N derivatives cannot be used as microviscosity sensors.**

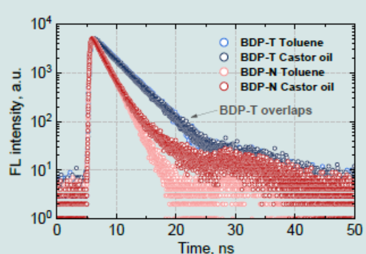

Temperature impact

- **BDP-T** and **BDP-N** dissolved in cyclohexane and **BDP-T** in chloroform showed decreasing FL lifetime with increasing temperature.
- Reverse dependence is seen for **BDP-N** in chloroform.
- **The studied derivatives are not temperature sensors.**

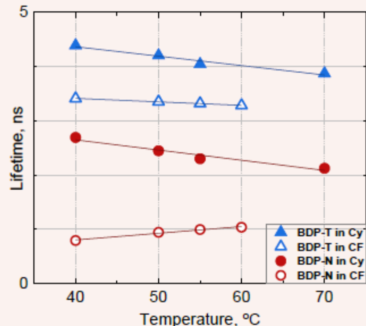

Orientation polarisability

Lippert's equation was used to rank pure solvents by their polarity.

$$\Delta f = \frac{\varepsilon - 1}{2\varepsilon + 1} - \frac{n^2 - 1}{2n^2 + 1}$$

Here ε is a relative permittivity and n is the refractive index of a pure solvent.

Polarity impact

- **Increasing orientation polarization** of the solvent (Δf) **decreases fluorescence's intensity, lifetime and quantum yield** for both studied molecules.
- Sensor sensitivity evaluation (a relative change of FL lifetime, when Δf changes by 0.1) shows that **BDP-N is more sensitive to polarity** than **BDP-T** (31% and 22%, respectively).
- **BDP-T and BDP-N can be used as polarity sensors.**

Sol-vent	Quantum yield	
	BDP-T	BDP-N
Cy	39.26 %	14.18 %
MeOH	8.66 %	1.14 %

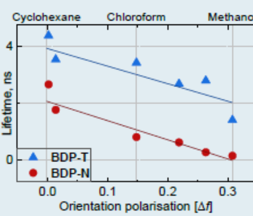

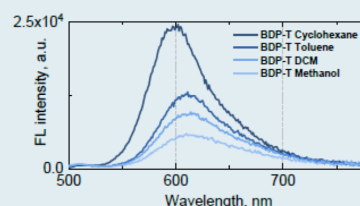

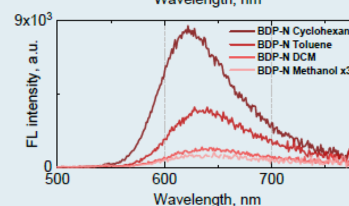

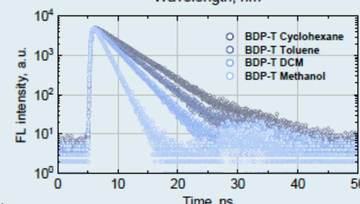

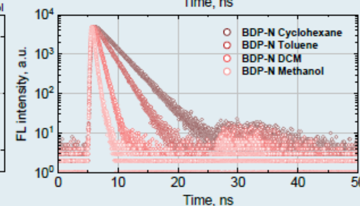

Conclusions

- Adding thiophene moieties in 2- and 6- BODIPY positions increases molecule's conjugation, redshifts fluorescent spectra and enables to achieve large Stokes shift. Furthermore, a transformation of viscosity sensor to polarity sensor is achieved.
- Fluorescence decays of **BDP-T** and **BDP-N** are monoexponential, which simplifies data analysis and reduces photon counts required for measurements.
- It is possible to create a polarity probe based on these molecules, especially **BDP-N**, which is more sensitive to solvent polarity than **BDP-T**.

References

[1] M. K. Kuimova, Phys. Chem. Chem. Phys. vol 14, no 37, p. 12671, 2012.
[2] S. Toliautas et al., Chem. Eur. J., vol. 25, 44, p. 10342-10349, 2019.
[3] Y. Chen et al., J. Org. Chem. vol. 77, 5, p. 2192-2206, 2012.

[1] Center for Physical Sciences and Technology, Saulėtekio av. 3, Vilnius, Lithuania
[2] Institute of Chemistry, Faculty of Chemistry and Geosciences, Vilnius University, Naugarduko str. 24, Vilnius, Lithuania

P8

Energy Barriers in $MAPbI_3$ Perovskite Films

Rokas Gegevičius, Rokas Jasiūnas, Simonas Driukas, Marius Franckevičius, Vidmantas Gulbinas

Department of Molecular Compound Physics. Center for Physical Sciences and Technology. Saulėtekio Avenue 3, Vilnius LT-10257.

rokas.gegevicius@ftmc.lt

Over the last decade, perovskite community have witnessed enormous technology advancement and application diversity of this new extraordinary material, starting from highly efficient solar cells,[1] bright tuneable LED's[2] to fast and sensitive photodetectors.[3] During recent years, the knowledge about fundamental processes in perovskite materials has greatly expanded, however, many aspects of charge carrier behaviour are still poorly understood and demands a deeper investigation.

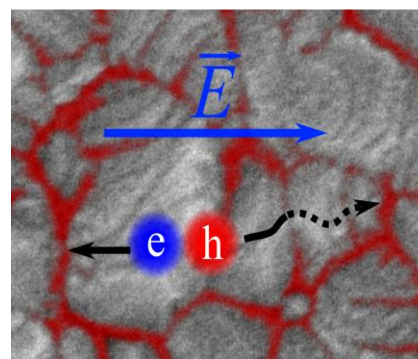

Fig. 1 Energy barriers restrict lateral charge carrier motion

In this work, transient photocurrent, time-delayed collection field and transient fluorescence techniques along with numerical simulations are combined to address charge carrier trapping processes during their lateral motion in prototypical methylammonium lead iodide perovskite films formed on interdigitated comb of electrodes. Carrier mobility decreases on hundreds of ns timescale, and its rate depends on the motion character—it is faster when charge carriers drift in the electric field and slower when the motion is caused by diffusion only. This difference becomes particularly evident at low temperatures. Based on the time-delayed collection field data and carrier motion modelling results, we demonstrate that the rapid charge carrier mobility decay at low temperatures is mainly caused by the energy barriers, most likely formed at crystallite boundaries. Even though these barriers are surmountable at room temperature, they still play a major role in determining carrier mobility and diffusion rates. Suggested concept of the potential barriers moves beyond the conventional understanding of carrier mobility, diffusion, and recombination processes in hybrid halide perovskites.

REFERENCES*:*

1. M. A. Green, Y. Hishikawa, E. D. Dunlop, D. H. Levi, J. Hohl-Ebinger, M. Yoshita, A. W. Y. Ho-Baillie, Prog. Photovoltaics 2019, 27, 3.

2. B. Zhao, S. Bai, V. Kim, R. Lamboll, R. Shivanna, F. Auras, J. M. Richter, L. Yang, L. Dai, M. Alsari, X. J. She, L. Liang, J. Zhang, S. Lilliu, P. Gao, H. J. Snaith, J. Wang, N. C. Greenham, R. H. Friend, D. Di, Nat. Photonics2018, 12, 783.

3. R. Gegevičius, M. Franckevičius, V. Pakštas, R. Augulis, V. Gulbinas, Phys. Status Solidi A 2018, 215, 1700822

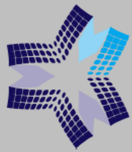

CENTER FOR PHYSICAL SCIENCES AND TECHNOLOGY

Energy Barriers in $MAPbI_3$ Perovskite Films

Rokas Gegevičius, Rokas Jasiūnas, Marius Franckevičius, Vidmantas Gulbinas

Molecular Compound Physics Department, Centre for Physical Sciences and Technology, Saulėtekio Ave. 3, LT-10257 Vilnius, Lithuania.

- In this work, **Transient Photocurrent**, **Time-Delayed Collection Field** and **Transient Fluorescence** techniques are combined to address charge carrier trapping processes during their lateral motion in prototypical methylammonium lead iodide perovskite ($MAPbI_3$) films formed on interdigitated electrodes.
- Carrier mobility decreases on hundreds of ns timescale, and its rate depends on the motion character—it is faster when charge carriers drift in the electric field and slower when the motion is caused by diffusion only. This difference becomes particularly evident at low temperatures. Based on the time-delayed collection field data and carrier motion modelling results, it is demonstrated that the rapid mobility decay at low temperatures is mainly caused by the energy barriers, most likely formed at crystallite boundaries.
- **Suggested concept of the potential barriers moves beyond the conventional understanding of carrier mobility, diffusion, and recombination processes in hybrid perovskites.**

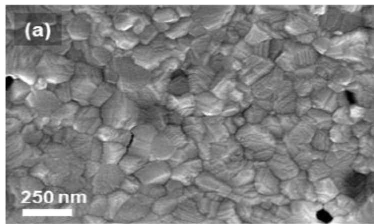

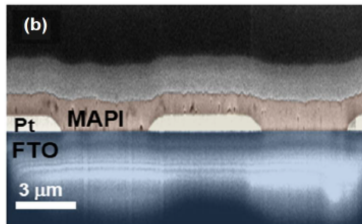

Figure 1. a) Top view scanning electron microscope (SEM) images of $MAPbI_3$ and b) The cross-sectional SEM image demonstrates lateral configurations of the perovskite films deposited on IDE.

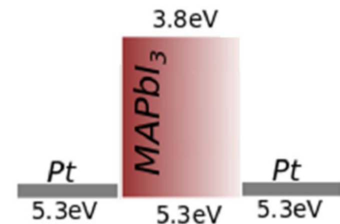

Figure 2. Energy level diagram of used samples

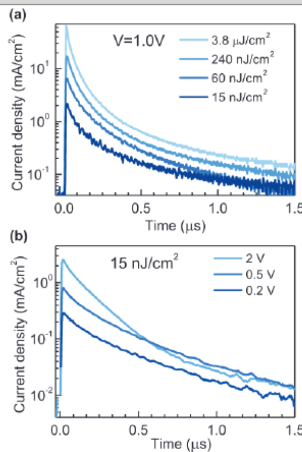

Figure 3. Transient photocurrent kinetics a) at different excitation intensities and b) at constant excitation intensity of 15 nJ cm^{-2}

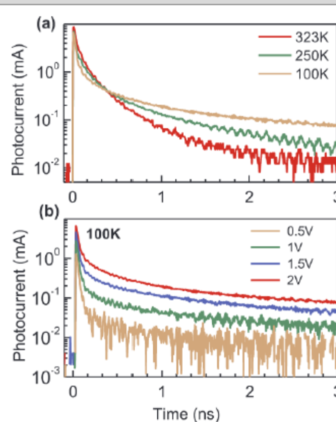

Figure 4. a) Photocurrent kinetics at different temperatures measured at 2 V applied voltage and 15 nJcm^{-2} excitation intensity, b) photocurrent kinetics at 100 K at different applied voltages.

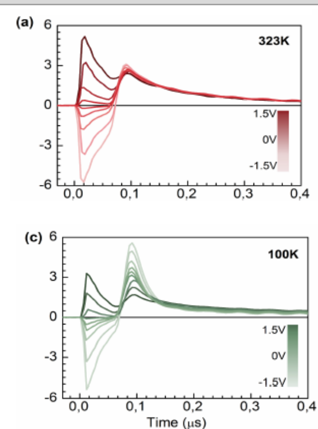

Figure 5. Photocurrent kinetics at different temperatures obtained by modified TDCF measurements under 15 nJ cm^{-2} excitation intensity.

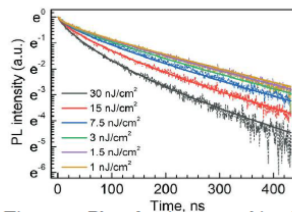

Figure 6. Photoluminescence kinetics of MAPI perovskite at different excitation intensities. λ_{ex} = 470 nm

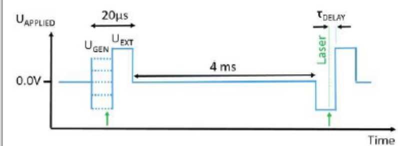

Figure 7. Time chart of the TDCF measurements. Conventional TDCF measurements correspond to Ugen= 0, while flipped field measurements were performed at Ugen< 0.

P9

Benefits of $MAPbI_3$ perovskite doping by Sr^{2+}

Rokas Jasiūnas[1], Rokas Gegevičius[1], Marius Franckevičius[1], Nga Phung[2], Antonio Abate[2] and Vidmantas Gulbinas[1]

[1]Department of Molecular Compound Physics, Center for Physical Sciences and Technology, Saulėtekio Avenue 3, LT-10257 Vilnius, Lithuania.

[2] Helmholtz-Zentrum Berlin für Materialien und Energie GmbH, Kekuléstr. 5, Berlin D-12489, Germany..

Email: rokas.jasiunas@ftmc.lt

Hybrid perovskite materials have witnessed immense development in a range of optoelectronic devices, such as bright tunable LEDs, fast and sensitive photodetectors, and especially efficient solar cells. Chemical doping of perovskites with foreign atoms is a promising way to tailor material properties towards improving performance and stability of solar cells.

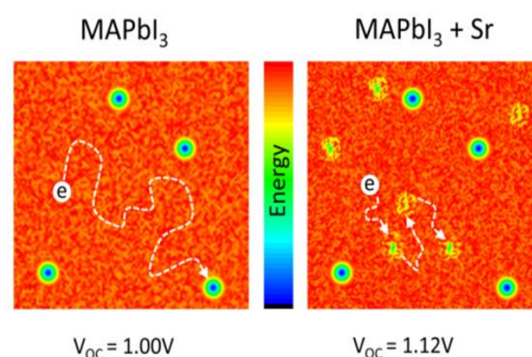

Fig. 1 Energy surface in $MAPbI_3$ film with and without small amount of Sr^{2+} doping

In this work [1], we discuss the efficiency increase in perovskite solar cells based on $MAPbI_3$ active layer, doped with 0.1 to 5 % of Sr2+ agent. A small amount <1 % of Sr^{2+} added to the perovskite improves open-circuit voltage by ~100 mV and consequently enhances the power conversion efficiency from 16.8 % to 17.8 %.

By employing transient photoluminescence, transient photocurrent and time-delayed collection field measurements we show that doping of $MAPbI_3$ by low content of Sr^{2+} additives (≤ 0.4 %) reduces the electron trapping efficiency. Whereas the reduced trapped electron density suppress nonradiative Shockley-Read-Hall recombination, which positively impacts open ciruit voltage of perovskite solar cells.

REFERENCES

[1] R. Jasiūnas, R. Gegevičius, M. Franckevičius, N. Phung, A. Abate and V. Gulbinas, *SOLAR RRL, Submitted*

Benefits of $MAPbI_3$ perovskite doping by Sr^{2+}

Rokas Jasiūnas[1] , Rokas Gegevičius[1], Marius Franckevičius[1], Nga Phung[2], Antonio Abate[2] and Vidmantas Gulbinas[1]

[1]*Department of Molecular Compound Physics, Center for Physical Sciences and Technology, Saulėtekio Avenue 3, LT-10257 Vilnius, Lithuania.*

[2] *Helmholtz-Zentrum Berlin für Materialien und Energie GmbH, Kekuléstr. 5, Berlin D-12489, Germany.*

rokas.jasiunas@ftmc.lt

Introduction

Hybrid perovskite materials have witnessed immense development in a range of optoelectronic devices, such as bright tunable LEDs, fast and sensitive photodetectors, and especially efficient solar cells. Chemical doping of perovskites with foreign atoms is a promising way to tailor material properties towards improving performance and stability of solar cells.

In this work [1], we discuss the efficiency increase in perovskite solar cells based on $MAPbI_3$ active layer, doped with 0.1 to 5 % of Sr^{2+} agent. A small amount <1 % of Sr^{2+} added to the perovskite improves open-circuit voltage by ~100 mV and consequently enhances the power conversion efficiency from 16.8 % to 17.8 %.

By employing transient photoluminescence, transient photocurrent and time-delayed collection field measurements we show that doping of $MAPbI_3$ by low content of Sr^{2+} additives (≤ 0.4 %) reduces the electron trapping efficiency. Whereas the reduced trapped electron density suppress nonradiative Shockley-Read-Hall recombination, which positively impacts open circuit voltage of perovskite solar cells.

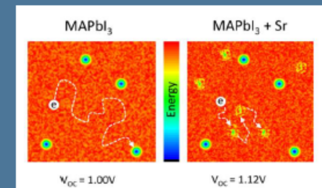

Fig. 1 Energy surface in $MAPbI_3$ film with and without small amount of Sr^{2+} doping

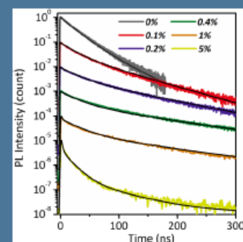

I. Transient Photoluminescence

Figure 2 shows the transient PL dynamics of the investigated $MAPbI_3$ films. The decay kinetics were fitted with multiexponential decay functions, and the relaxation times obtained from the approximations are provided in **Table 1.**

Sr^{2+} content in $MAPbI_3$	A1	τ1 [ns]	A2	τ2 [ns]	A3	τ3 [ns]
0%	0.84	20.2	0.22	37.6	-	-
0.1%	0.67	20.9	0.36	64.2	-	-
0.2%	0.65	26.9	0.35	93.5	-	-
0.4%	0.7	27.8	0.31	125.6	-	-
1.0%	0.59	1.4	0.55	27.8	0.20	128.9
5.0%	1.00	2.32	0.35	15.4	0.03	63.8

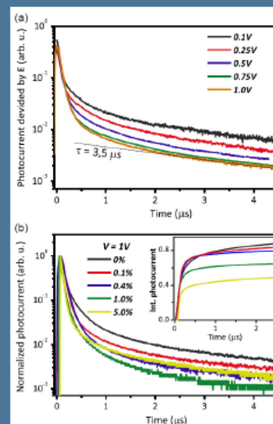

II. Transient Photocurrent

Figure 3 a) Photocurrent kinetics of pristine $MAPbI_3$ at indicated applied voltages and b) normalized photocurrent kinetics in samples with different Sr^{2+} concentrations at 1.0 V applied voltage. The insert in (b) shows integrated photocurrent kinetics (not normalized).

III. Time Delayed Collection Field

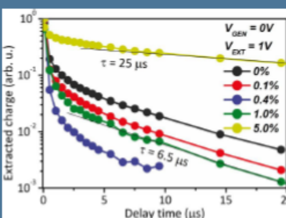

Figure 4. Dependencies of extracted charge value on delay time between the optical excitation pulse and electrical extraction pulse, obtained in different samples with 0 V generation and 1 V extraction voltages. The extracted charge was normalized to the extracted charge at zero delay time.

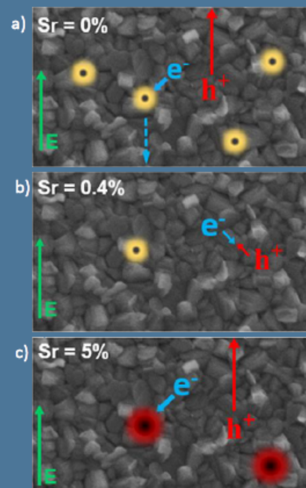

IV. CONCLUSIONS

Figure 5 summarizes results in a simple representative model (note that the SEM image does not correspond to the actual Sr^{2+} concentration sample but is used as a base for the schematic). Here, the green arrow shows the direction of an electric field.

In Figure 5a, the carrier dynamic is shown in a neat $MAPbI_3$ film. After the generation of charge carriers, holes are easily extracted (red arrow), whereas electrons swiftly fall (solid blue arrow) into a trap state (glowing yellow circle), from which they are slowly extracted by the electric field (dotted blue line).

The trap density decreases significantly in the presence of a low amount of Sr^{2+} additives (Figure 5b), which, despite resulting in increased V_{OC}, also enhances bimolecular recombination, as shown in the figure.

Higher Sr^{2+} concentration (Figure 5c), leads to the formation of deep trap states (glowing red circles). Electrons generated in the vicinity of such trap states fall into them and contribute to the slow photocurrent component.

References:

[1] Jasiūnas, R.; Gegevičius, R.; Franckevičius, M.; Phung, N.; Abate, A.; Gulbinas, V. Suppression of Electron Trapping in MAPbI3 Perovskite by Sr2þ Doping. Phys. Status Solidi RRL 2020, 5.

P10

Activity measurements of GMC superfamily flavoenzymes using Amplex Red assay

Rugilė Lukaševičiūtė[1] and Renata Karpicz[1]

[1]Department of Molecular Compound Physics, Center for Physical Sciences and Technology, Lithuania
rugile.lukaseviciute@ftmc.lt

Usage of biosensing systems containing enzymes is the promising and accurate method for detection of various compounds concentration in biological samples. Some of the most important properties describing enzyme are selectivity and enzymatic activity. In order to create and improve biosensor it is necessary to understand the properties of immobilized enzyme related to the influence of the surrounding environment.

The glucose-methanol-choline (GMC) superfamily is large family of oxidoreductases typically containing FAD-binding domain. Some members include oxidases like glucose oxidase (GOx), pyranose oxidase (POx), cholesterol oxidase (ChOx) and alcohol oxidase (AlOx). Electron donor substrates for GMC oxidoreductases range from various sugars and alcohols to cholesterol [1]. Amplex Red (10-acetyl-3,7-dihydroxyphenoxamine) is colorless and nonfluorescent reagent that is widely used as a probe to detect H_2O_2 in various biological samples [2]. In reactions catalysed by GOx, POx, ChOx and AlOx hydrogen peroxide is formed which then reacts with Amplex Red in the presence of horseradish peroxidase (HRP) and forms colored, highly fluorescent compound resorufin. Resorufin has exitation and emission maximum of 571 nm and because of high exitation coefficient enzyme activity can be determined fluorometrically or spectrophotometrically.

The purpose of this research was to evaluate activity of GOx, POx, ChOx and AlOx enzymes in different acidic values using Amplex Red reagent and determine optimal pH values for every enzyme. Our results show that Amplex Red assay can be used in measuring H_2O_2 released after enzymatic reaction. With decreasing acidity of the medium enzyme's activity increases. The amount of formed resorufin during enzymatic reactions increases respectively by reducing pH. At optimal medium acidity formed resorufin amount is largest whitch shows that enzyme's activity there is the highest.

REFERENCES

[1] L. Sutzl, G. Floey, E. J. Gillam, M. Boden, D. Haltrich „The GMC superfamily of oxidoreductases revised: analysis and evaluation of fungal GMC oxidoreductases," Biotechnology for Biofuels, 12, article 118, 2019.

[2] Baozhong Zhao, Fiona A. Summers, Ronald P. Mason „Photooxidation of Amplex red to resorufin: Implications of exposing the Amplex red assay to light," Free Radical Biology and Medicine, 53 1080-1087, 2012.

P11

Structural defect behavior of thermally annealed graphene, directly synthesized on Si(100) substrate using MW-PECVD

Šarūnas Jankauskas[1], Rimantas Gudaitis[1], Andrius Vasiliauskas[1] and Šarūnas Meškinis[1]

[1] *Institute of Materials Science of Kaunas University of Technology, K. Baršausko Str. 59, LT-51423, Kaunas, Lithuania*
Email: sarunas.jankauskas@ktu.lt

Graphene, material with exceptional physical properties, when synthesized using exfoliation, lacks certain qualities when grown directly on semiconducting surfaces. Although, microwave plasma enhanced chemical vapor deposition (MW-PECVD) can increase production rates of graphene, this form of synthesis introduces fair amount of defects [1]. To tackle this issue thermal annealing is rather straight forward method, which usually increases the overall quality of graphene by reducing the number of defects and other structural deformations, however there are other predominant effects, such as doping and strain, which could damage the sample [2]. Graphitic structure examination is usually based on Raman spectroscopy measurements which helps to determine both structure quality and thickness (graphene case).

In this work, four graphene samples were grown on Si(100) substrates, using MW-PECVD system (IPLAS Innovative Plasma Systems GmbH). Samples were thermally annealed using different temperatures (200-800°C) and environments (Ar, N2, vacuum) in order to thoroughly evaluate the changes of graphitic structures. All annealing's were performed for 30 min. The characterization of graphene samples was carried out using Raman spectrometer (Renishaw inVia, 532 nm, 4.5 mW) by analyzing changes in D, 2D and G bands. After annealing in Ar environment at temperatures, lower than 800°C, I_{2D}/I_G ratio changed from 1.04 to 0.47 and I_D/I_G ratio changed from 1.3 to 1.45, suggesting appearance of additional deformations. At higher temperatures (800°C, Ar) the graphitic structure collapses due to difference in thermal expansion coefficients between the graphene sheets and the substrate. Annealing in N_2 environment, I_{2D}/I_G changed from 1.6 to 0.62 and I_D/I_G from 1.56 to 2.02 hinting a huge increase in defective sites and strain development. After investigating changes in Raman spectrum after annealing in vacuum we have found out that I_{2D}/I_G changed from 0.61 to 0.23 and I_D/I_G from 1.53 to 1.71, showing that the dominant effect is rather defect formation than reduction, however values indicate a large number of layers, which could lead to inconclusive estimations.

In conclusion, we can see that our graphene structures are imperfect, which is true for such materials synthesized using MW-PECVD, however we believe that defect reduction could be achieved when samples exhibit more prominent graphene characteristics.

REFERENCES

[1] S. Zheng et al.; *RSC Advances* ***7*** (2017) pp. 33185-33193.
[2] M. Alyobi et al.; *Crystals* ***7*** (2017) pp. 349.

P12

In-situ probing of SAM and tBLM layer formation on nanostructured gold by ATR-SEIRAS

Vaidas Pudžaitis[1], Martynas Talaikis[2], Gediminas Niaura[1]

[1]*Department of Organic chemistry, Center for Physical Sciences and Technology, Sauletekio ave. 3, LT-10257 Vilnius, Lithuania.*

[2]*Institute of Biochemistry, Life Sciences Center, Vilnius University, Sauletekio ave. 7, LT-10257 Vilnius, Lithuania*

Email: vaidas.pudzaitis@ftmc.lt

Attenuated total reflection surface-enhanced infrared reflection absorption spectroscopy (ATR-SEIRAS) is a powerful tool for *in-situ* analysis of molecular phenomena at the nanostructured metal surface. Various processes can be monitored in the water environment and under electrode potential control. Even more, a good signal-to-noise ratio provides the possibility to track the formation process of the self-assembled monolayers (SAMs).

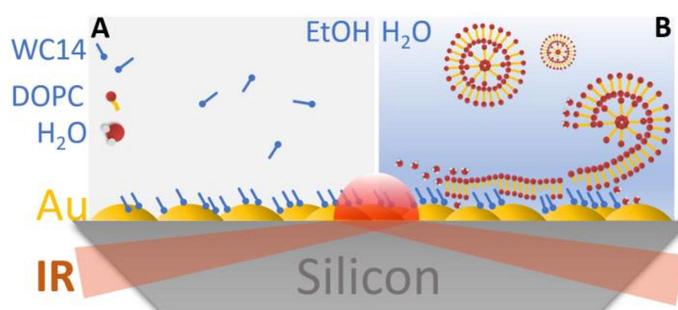

Fig.1 Schematic view of ATR-SEIRAS experiment

We demonstrate the use of ATR-SEIRAS for probing a two-step process of tethered bilayer lipid membrane (tBLM) formation. The tBLMs are living-cell membrane mimicking constructions which are used for biosensing applications, and as a platform for fundamental studies of biological membranes. During the first step (Fig. 1A), lipid bilayer anchoring SAM is formed from lipid-like WC14 [20-tetradecyloxy-3,6,9,12,15,18,22-heptaoxahexatricontane-1-thiol] compound on the nanostructured gold surface [1]. The surface was prepared by a relatively simple electroless plating procedure on silicon [2]. On a second step (Fig. 1B), we conducted the phase exchange to water and deposited the tBLM from multilamellar vesicles (MVCs) prepared from 1,2-dioleoyl-sn-glycero-3-phosphocholine (DOPC) and cholesterol (CHOL) [3]. The acquired spectroscopic information provides the possibility to get insight into the membrane formation timing, phase exchange effect on SAM, and surface processes, such as solvent exchange effects.

In this work, we demonstrated, that ATR-SEIRAS can provide complementary and in some cases unique molecular level information to already widely used methods such as ellipsometry, fluorescence correlation spectroscopy and electrochemical impedance spectroscopy.

REFERENCES

[1] R. Butvidyte et all; Langmuir **29** (2013) pp. 8645−8656.

[2] H. Miyake, S. Ye, M. Osawa; Electrochemistry Communications **4** (2002) pp. 973–977

[3] T. Ragaliauskas, M. Mickevicius, B. Rakovska, T. Penkauskas, D. J. Vanderah, F. Heinrich, G. Valincius; Biochimica et Biophysica Acta **1859** (2017) pp. 669–678.

In-situ probing of SAM and tBLM layer formation on nanostructured gold by ATR-SEIRAS

Vaidas Pudžaitis[1], Martynas Talaikis[2], Gediminas Niaura[1]

[1]Department of Organic chemistry, Center for Physical Sciences and Technology, Sauletekio ave. 3, LT-10257 Vilnius, Lithuania.
[2]Institute of Biochemistry, Life Sciences Center, Vilnius University, Saulėtekio av. 7, LT-10257 Vilnius, Lithuania

INTRODUCTION

Attenuated total reflection surface-enhanced infrared reflection absorption spectroscopy (ATR-SEIRAS) is a powerful tool for in-situ analysis of molecular phenomena at the nanostructured metal surface. Various processes can be monitored in the water environment and under electrode potential control. Even more, a good signal-to-noise ratio provides the possibility to track the formation process of the self-assembled monolayers (SAMs). We demonstrate the use of ATR-SEIRAS for probing a two-step process of tethered bilayer lipid membrane (tBLM) formation. The tBLMs are living-cell membrane mimicking constructions which are used for biosensing applications, and as a platform for fundamental studies of biological membranes.

EXPERIMENT

During the first step (**Fig. 1A**), SAM layer is formed from lipid-like WC14 [20-tetradecyloxy-3,6,9,12,15,18,22-heptaoxahexatricontane-1-thiol] compound mix with β-mercaptoethanol (BME) on the nanostructured gold surface (Picture 1) [1]. Surface was prepared by electroless plating procedure on 0.25 µm polished silicon with 7.5 mM $NaAuCl_4$ solution containing Na_2SO_3, $Na_2S_2O_3$, NH_4Cl and NH_4F salts at room temperature [2].

Picture 1. AFM image of 0.25 µm polished Si prism surface (left) covered with gold by electroless plating (right).

SAM formation was monitored on FT-IR spectrometer equipped with MCT detector (Bruker, Vertex 80v) and VeeMax^{TM} ATR accessory (PIKE technologies) at 4 cm^{-1} resolution (~11 s/spectrum). EtOH solution on gold was used as a reference spectrum. Data representing 1mM WC14:BME (3:7 ratio respectively) SAM formation are shown in figure **1C**. By observing C-H stretching peaks of WC14 (**Fig. 1D**), it can be confirmed – initial SAM formation is complete in ~2-3 min time. On a second step (**Fig. 1B**), ethanol was exchanged with water, which lead to WC14 methyl and ethyl peak shifts of 2 cm^{-1} towards lower energy (data not shown). This step was used as a reference for further FTIR observations. The tBLM was deposited from multilamellar vesicles (MVCs) prepared from 1,2-dioleoyl-sn-glycero-3-phosphocholine (DOPC) and cholesterol (CHOL) by pipetting 100 µl [3]. DOPC tBLM formation in ~15-20 min can be observed by plotting C-H stretch peak intensities against time (**Fig. 1F**). Additionally, water exchange from SAM's surface can be seen occurring concurrently (**Fig. 1E**).

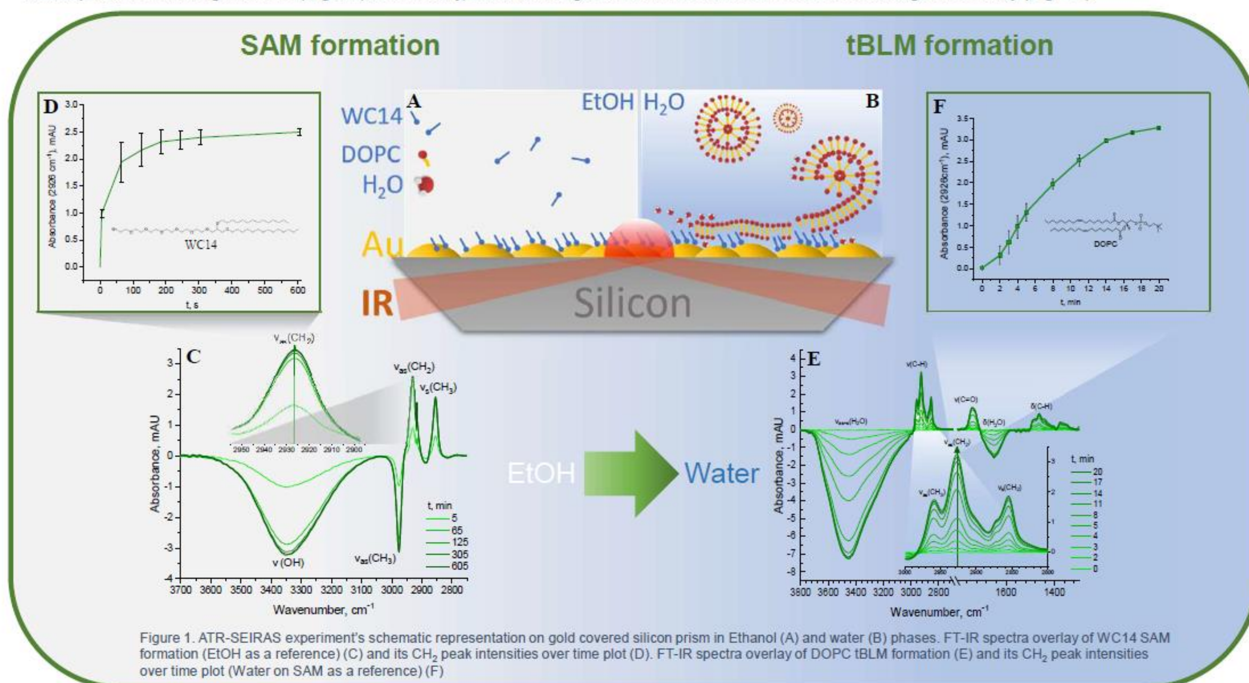

Figure 1. ATR-SEIRAS experiment's schematic representation on gold covered silicon prism in Ethanol (A) and water (B) phases. FT-IR spectra overlay of WC14 SAM formation (EtOH as a reference) (C) and its CH_2 peak intensities over time plot (D). FT-IR spectra overlay of DOPC tBLM formation (E) and its CH_2 peak intensities over time plot (Water on SAM as a reference) (F)

CONCLUSIONS

We demonstrate, that ATR-SEIRAS can provide complementary and in some cases unique molecular level information to already widely used methods. We show, that WC14 based SAM absorbs to the nanostructured gold surface in 2-3 min., while the DOPC based tBLM is formed in 20 min., pushing ethanol and water molecules (for SAM and tBLM respectively) away from the surface at a similar rate. Additionally, we see phase exchange (EtOH to H_2O) effect on C-H stretch vibrations, that confirms tighter SAM ordering.

REFERENCES

[1] R. Butvidyte et all; Langmuir 29 (2013) pp. 8645–8656.

[2] H. Miyake, S. Ye, M. Osawa; Electrochemistry Communications 4 (2002) pp. 973–977

[3] T. Ragaliauskas, M. Mickevicius, B. Rakovska, T. Penkauskas, D. J. Vanderah, F. Heinrich, G. Valincius; Biochimica et Biophysica Acta 1859 (2017) pp. 669–678.

P13

Impact of thin low specific conductivity layer on Fano resonance amplitude in an array of split ring resonators

A. Kamarauskas, G. Šlekas, D. Seliuta, and Ž. Kancleris

[1]*Center for Physical Sciences and Technology, Vilnius, Lithuania.*
Email: andrius.kamarauskas@ftmc.lt

The electromagnetic manifestation of Fano resonance was discovered in metasurface (MS) by Fedotov et al. [1] and later was widely investigated by many other researchers. Usually, it occurs in MS made from asymmetric split-ring resonators, but it was also observed in mirror-symmetric MS made from usual split-rings [2]. In this case, Fano resonance arises due to the interaction of 3rd order plasmonic mode and lattice mode.

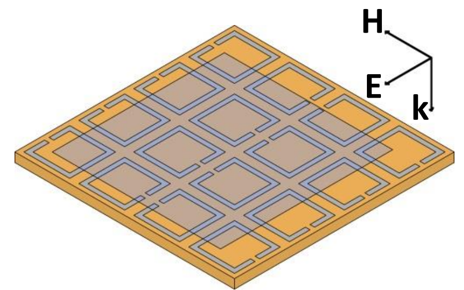

Fig. 1 The array of split-ring resonators with conductive layer on a top. The electric field is perpendicular to resonators' gap.

In this work, we investigate such a mirror-symmetric MS, the unit cell of which is shown in Fig. 1. The MS is made on 125 μm thickness substrate with a dielectric constant 2.2. The dimensions of the unit cell in the lateral plane are 1200 μm and 600 μm. The width of the resonators is 500 μm, the width of the strip and the gap is 50 μm. The resonators are made from 9 μm thickness cooper foil. The 2 μm thick layer with the same dielectric constant, which can be made from conductive polymer, is placed on the front or the back side of the substrate. Numerical modelling was performed using CST Microwave Studio software.

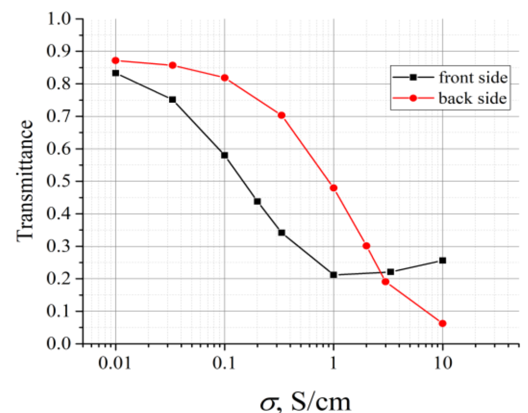

Fig. 2 The transmittance at the maximum amplitude of the Fano resonance versus specific conductivity of the layer. Resonance frequency at front side configuration is 222.9 GHz, at back side - 224.4 GHz.

Calculated dependences of transmittance at the maximum amplitude of the Fano resonance on specific conductivity of the layer situated on the front and back sides of the MS are shown in Fig. 2. It is seen that the difference in the transmitted signal through the MS is observed depending on the layer position when the conductivity of the layer is as low as 0.01 S/cm. On the one hand, the decrease of the transmittance on the conductivity is larger when the layer is placed on the resonator plane. On the other hand, the dynamic range is wider in the back side configuration. High sensitivity of the Fano resonance amplitude in the proposed structure to the low-to-mid conductivity planar sheet could be useful in sensing applications or modulation of electromagnetic waves.

REFERENCES

[1] V. Fedotov et al., *Phys. Rev. Lett.* **99**, (2007) 147401.
[2] D. Seliuta et al., *Optics Letters* **44**, (2019) pp. 759-762.

P14

Black silicon based substrates for surface enhanced Raman spectroscopy

Ieva Matulaitienė[1], Lena Golubewa[1], Renata Karpicz[1], Algirdas Selskis[1] and Polina Kuzhir[2,3]

[1] *Center for Physical Sciences and Technology, Sauletekio Ave. 3, LT-10257 Vilnius, Lithuania.*

[2] *Institute for Nuclear Problems of BSU, Bobruiskaya 11, 220030 Minsk, Belarus.*

[3] *Institute of Photonics, University of Eastern Finland, Yliopistokatu 2, FI-80100 Joensuu, Finland.*

Email: ieva.matulaitiene@ftmc.lt.

The evolution of new technologies brought to humankind not only comfortable environment, but also new treats. The major treat is environmental pollution that leads to various diseases and requires new processes, diagnostic systems. Surface enhanced Raman spectroscopy (SERS) is one of the most sensitive techniques of vibrational spectroscopy that gives information about the material in molecular level. Nowadays there are plenty techniques for SERS substrates fabrication, that must meet three conditions: certain metal surface (Au, Ag, Cu), the surface is rough and sample must be near or adsorbed at the surface [1]. In this study, we represent black silicon based substrates (bSi) for SERS application.

Black silicon based substrates showed outstanding performance to detect monomolecular layer of model compound 4-mercaptobenzoic acid (4-MBA) and living rat glioma cells (Fig. 1). It was defined that enhancement factor for our substrate is 10^8.

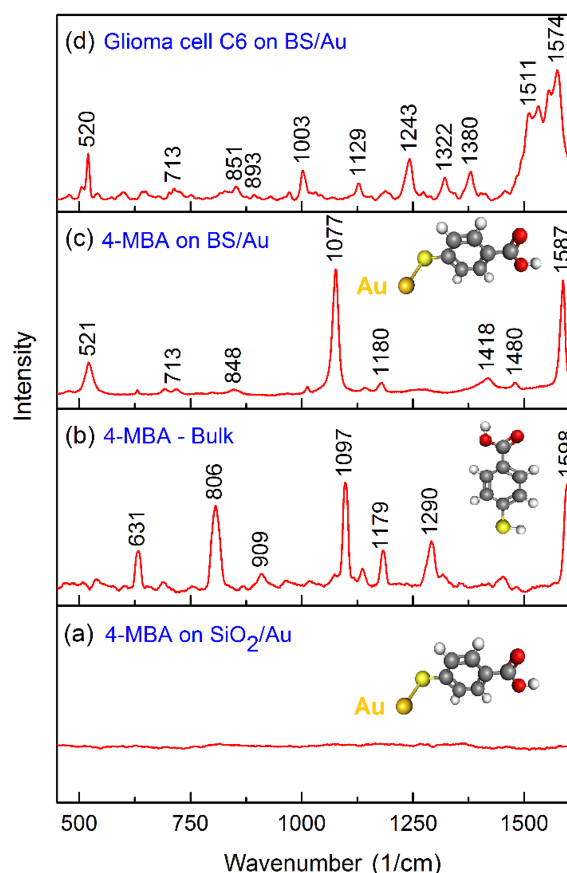

Fig. 1 Raman spectra of 4-MBA monolayer on SiO_2/Au smooth substrate (a), of bulk 4-MBA (b), and SERS spectra of 4-MBA (c) and living rat glioma cell (d) on the bSi/Au substrate. Excitation wavelength is 785 nm.

REFERENCES

[1] S. Schlucker, *Angew. Chem. Int. Ed.* **53** (2014) pp. 4756–4795.

Black silicon based substrates for surface enhanced Raman spectroscopy

Ieva Matulaitienė[1], Lena Golubewa[1], Renata Karpicz[1], Algirdas Selskis[1] and Polina Kuzhir[2,3]

[1] Center for Physical Sciences and Technology, Sauletekio Ave. 3, LT-10257 Vilnius, Lithuania.
[2] Institute for Nuclear Problems of BSU, Bobruiskaya 11, 220030 Minsk, Belarus.
[3] Institute of Photonics, University of Eastern Finland, Yliopistokatu 2, FI-80100 Joensuu, Finland.
Email: ieva.matulaitiene@ftmc.lt.

The evolution of new technologies brought to humankind not only comfortable environment, but also new treats. The major treat is environmental pollution that leads to various diseases and requires new processes, diagnostic systems. Surface enhanced Raman spectroscopy (SERS) is one of the most sensitive techniques of vibrational spectroscopy that gives information about the material in molecular level. Nowadays there are plenty techniques for SERS substrates fabrication, that must meet three conditions: certain metal surface (Au, Ag, Cu), the surface is rough and sample must be near or adsorbed at the surface [1]. In this study, we represent black silicon based substrates (bSi) for SERS application.

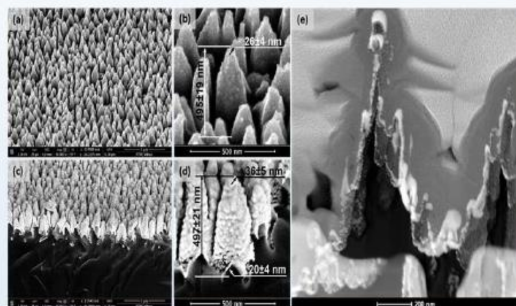

Fig.1. SEM images of bSi (a, b) and bSi/Au (c, d) substrates; (e) TEM image of the silicon cone covered by 25-50 nm thick gold layer.

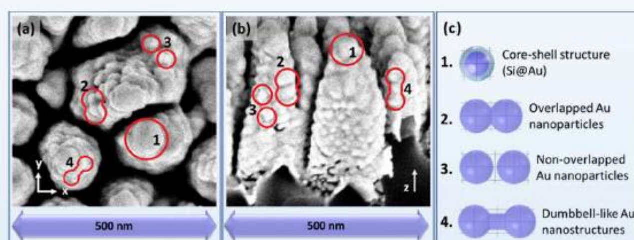

Fig. 3. (a) top-view SEM image of bSi/Au showing horizontally (perpendicular to the wavevector k ⃗) oriented bi-spheres and dumbbell-like particles; (b) side-view SEM image of bSi/Au showing vertically (along the wavevector k ⃗) oriented bi-spheres and dumbbell-like particles; (c) elementary nanostructures selected for numerical simulation of the E-field enhancement.

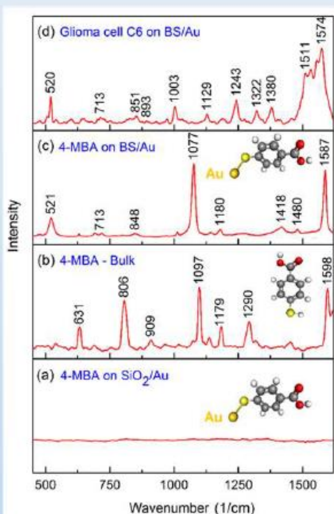

Fig. 2. Raman spectra of 4-MBA monolayer on SiO_2/Au smooth substrate (a), of bulk 4-MBA (b), and SERS spectra of 4-MBA (c) and living rat glioma cell (d) on the bSi/Au substrate. Excitation wavelength is 785 nm.

The enhancement factor of the SERS-active bSi/Au substrate $\approx 2 \times 10^8$.

$$EF = \frac{I_{BSi/Au} / N_{BSi/Au}}{I_{bulk} / N_{bulk}}$$

where $I_{BSi/Au}$ ($N_{BSi/Au}$) and I_{bulk} (N_{bulk}) are Raman intensities (numbers of irradiated molecules) of 4-MBA monolayer on the bSi/Au substrate and bulk 4-MBA on the SiO_2 substrate obtained at the same laser power and time accumulation, respectively.

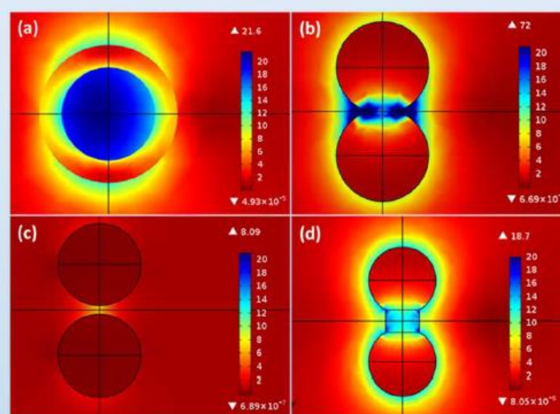

Fig. 4. E-filed enhancement maps at the irradiation wavelength of 790. (a) Si@Au (44nm@21nm), (b) Au bi-sphere (r = 25 nm, distance 47.5nm), (c) Au bi-sphere (r = 25 nm, distance 55 nm), (d) dumbbell-like structure (r_0 = 13.5 nm). Δ and ∇ are maximum and minimum values of the E-filed enhancement, respectively.

Assignments of vibrational bands of 4-MBA in solid and adsorbed

Raman solid state (cm⁻¹)	bSi/Au/ 4-MBA (cm⁻¹)	Calculated Au_1- 4-MBA (cm⁻¹)	Peak assignment
–	521	498	ν(CS)
631	631	642	ν_{6b}
–	693	–	γ(CH) out-of-plane
–	713	–	ν_{4b} + γ(CCC) out-of-plane
806	–	766	ν_{10a}
–	848	–	β(COO⁻)
909	–	–	β(SH)
–	1013	–	in-plane ring breathing, b_2
1097	1077	1059	ν_{12} (a_1) in-plane aromatic ring breathing mode + ν(CS), a_1
–	1142	–	ν_{15} (b_2) δ(CH) deformation
1179	1180	1162	ν_9 (a_1) δ(CH) deformation
1290	–	–	ν_3
–	–	1326	ν (COO⁻) stretching mode
–	1418	–	ν (COO⁻) stretching mode
–	1480	–	ν(CC) + γ(CH)
1598	1587	1585	ν_{8a} (a_1) totally symmetric aromatic ring vibration

We perform a new bSi material possessing the unique properties allowing the use of the bSi sputtered with gold substrate as a highly sensitive stable SERS-active platform for detection of not only trace amounts of small organic molecules, but also living cells. The produced bSi surface due to its significant roughness, submicron regular cone structures evenly distributed over the entire surface, their high density allows to obtain the SERS-active surface with sufficiently good EF of about 108 and to create evenly distributed hot spots through the deposition of only 25÷50 nm gold layer instead of 100-400 nm traditionally used, significantly reducing production costs. Simulation results fully proved high E-field enhancement and revealed the major impact of LSPR in SERS properties of BS/Au substrates. Moreover, it was established that only vertical nanostructures alignment along bSi/Au cones provides appearance of the resonant absorption in NIR and significant E-field enhancement with EF of 10^4-10^8.

The BS/Au substrates may be easily fabricated in a large-scale using existing techniques, with the tune control of specific surface parameters, providing efficient enhancement, stability and reproducibility, and is a promising substrate for biosensor systems.

Acknowledgements This work was financially supported by joint project no. S-LB-19-4 from the Research Council of Lithuania Foundation, the Belarusian Republican Foundation for Fundamental Research (BRFFR) project F19LITG-003.

P15

Terahertz detection and noise properties of $(Cd_{1-x}Zn_x)_3As_2$

I. Yahnyuk[1], D. But[1], D. Yavorskiy[1], G. Grabecki[2], K. Grasza[2], W. Knap[1,3] and S. Rumyantsev[1]

[1] International Research Centre CENTERA, Institute of High Pressure Physics, Polish Academy of Sciences, 01-142 Warsaw, Poland
[2] Institute of Physics PAS, al. Lotników 32/46, PL 02-668 Warsaw, Poland
[3] Laboratoire Charles Coulomb (L2C), UMR CNRS 5221, F-34095 Montpellier, France
Email: ivan.yahniuk@unipress.waw.pl

Although Cd_3As_2 as a semiconductor material is known for almost a century, it has not found wide applications so far. The main reasons are difficulties in technology and doping. However, the large tunability of band gap from 0 eV for Cd_3As_2 to 1 eV for Zn_3As_2 makes it an ideal material for infrared and terahertz applications. Also interests in this material was renewed by the theoretical study [1] showing the presence of a pair of symmetry protected three-dimensional Dirac cones. Indirect proof of this theoretical prediction is the extremely high electron mobility and the strong dependence of the electrons effective mass on their concentration. Extraordinary electronic properties and high mobility make it interesting for terahertz applications.

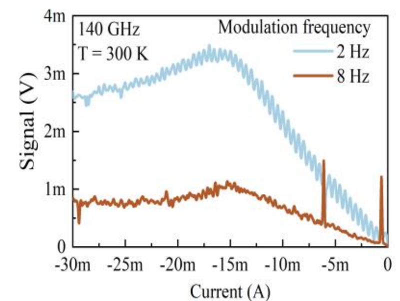

Fig. 1 . Detected signal as a function of current. F=140 GHz,

In this work, we studied electrical, noise, and high frequency properties of the $(Cd_{0.4}Zn_{0.6})_3As_2$ for its possible terahertz applications. The measurements of the resistivity show that at T > 220 K the resistivity is only weakly dependent on temperature. In the range between 180 K and 220 K it grows very fast with temperature decrease. In some cases the change of the resistivity in this temperature range can be as high as four orders of magnitude. S-type of the current voltage characteristic was found at temperatures T < 180 K. We attribute this shape of the characteristic to the presence p- and n – islands and switching between them [2].

The high frequency detection was studied at sub-terahertz frequencies of 100GHz and 140 GHz in two and four probes configuration. Measurements indicated the relatively high amplitude of the response in a few millivolt ranges for an incident power of approximately 35 mW. The current dependence of the response had some signs of the bolometric mechanism, i.e. very slow dynamic, in the range of hundred milliseconds and zero response at zero current (Fig.1). However, the temperature dependence of the response did not indicate its increase within the temperature range 180 – 220 K, as expected. In order to exclude the possible detection by the contacts, the detection was studied in four probe configuration and confirmed their minor role. Measurements of the low frequency noise indicated the 1/f shape of the spectra with the maximum amplitude at T ~ 270 K.

REFERENCES

[1] Z. Wang, H. Weng, Q. Wu, X. Dai, and Z. Fang, Phys. Rev. B 2013, 88, 125427.
[2] G. Grabecki et al., Apparent metal-insulator transition in $(Cd_{0.4}Zn_{0.6})_3As_2$ (in preparation)

Terahertz detection and noise properties of $(Cd_{1-x}Zn_x)_3As_2$

I. Yahnyuk[1], D. But[1], D. Yavorskiy[1], G. Grabecki[2], K. Grasza[2], W. Knap[1,3] and S. Rumyantsev[1]

[1] International Research Centre CENTERA, Institute of High Pressure Physics, Polish Academy of Sciences, 01-142 Warsaw, Poland
[2] Institute of Physics PAS, al. Lotników 32/46, PL 02-668 Warsaw, Poland
[3] Laboratoire Charles Coulomb (L2C), UMR CNRS 5221, F-34095 Montpellier, France

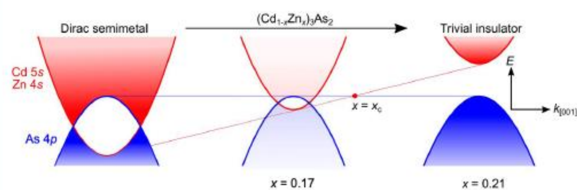

Evolution of the surface transport through topological phase transition. Zn doping-induced topological phase transition from a Dirac semimetal (DSM) to a trivial insulator in $(Cd_{1-x}Zn_x)_3As_2$ [1]

Dirac semimetals

- Dirac dispersion in the touch points
- Valence and conduction band touching in discrete points
- Robust against perturbations

Although Cd_3As_2 as a semiconductor material is known for almost a century, it has not found wide applications so far. The main reasons are difficulties in technology and doping. However, the large tunability of band gap from 0 eV for Cd_3As_2 to 1 eV for Zn_3As_2 makes it an ideal material for infrared and terahertz applications. Also interests in this material was renewed by the theoretical study showing the presence of a pair of symmetry protected three-dimensional Dirac cones [2]. Indirect proof of this theoretical prediction is the extremely high electron mobility and the strong dependence of the electrons effective mass on their concentration. Extraordinary electronic properties and high mobility make it interesting for terahertz applications.

In this work, crystals of $(Cd_{0.4}Zn_{0.6})_3As_2$ were grown by were grown by horizontal Bridgman method [3]. The studied samples of bulk material were in a few millimeters in size with Hall bar geometry and indium contacts.

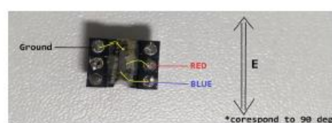

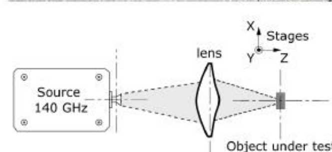

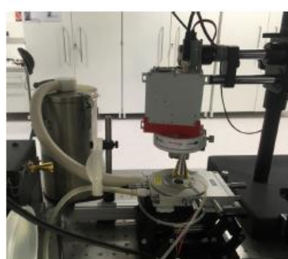

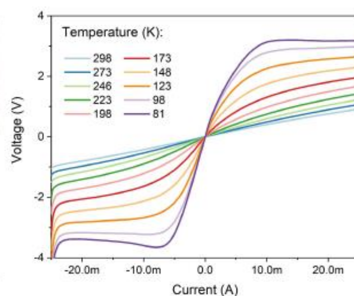

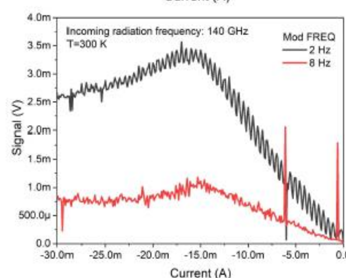

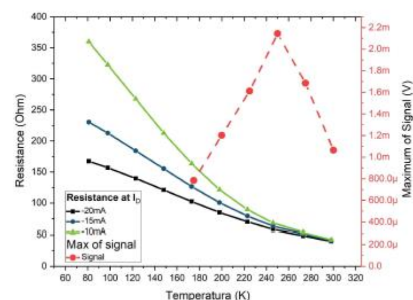

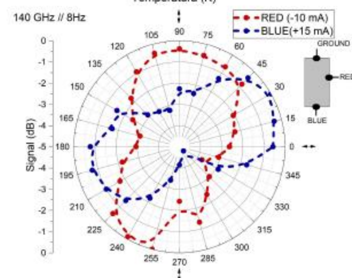

Reference:

[1] Shinichi Nishihaya, et.al, [Nat.Comm. 10, 2564 (2019)]
[2] Z. Wang, H. Weng, Q. Wu, X. Dai, and Z. Fang, Phys. Rev. B 2013, 88, 125427.
[3] G. Grabecki et al., Apparent metal-insulator transition in $(Cd_{0.4}Zn_{0.6})_3As_2$ (in preparation)

Conclusions

- The high frequency detection was studied at sub-terahertz frequencies of 100GHz and 140 GHz.
- Relatively high amplitude of the response in a few millivolt ranges for an incident power of approximately 35 mW.
- The current dependence of the response had some signs of the bolometric mechanism.

Acknowledgements: The „Center for Terahertz Research and Applications (CENTERA)" project is carried out within the 'International Research Agendas' programme of the Foundation for Polish Science co-financed by the European Union under the European Regional Development Fund.

CENTERA (MAB/2018/9) Institute of High Pressure Physics PAS, Sokołowska 29/37 Str, PL-01-142 Warsaw

P16

Enhanced sensitivity AlGaN/GaN HEMT terahertz detector without ungated regions

Juozas Vyšniauskas[1], Kęstutis Ikamas[1,2] and Alvydas Lisauskas[1,3]

[1] *Institute of Applied Electrodynamics and Telecommunications, Vilnius University, Vilnius, Lithuania.*

[2] *Department of Defence Technologies, Military Academy of Lithuania, Vilnius, Lithuania.*

[3] *CENTERA Labs, Institute of High Pressure Physics PAS, Warsaw, Poland.*

Email: juozas.vysniauskas@ff.vu.lt.

AlGaN/GaN HEMTs [1,2] and nMOS [3] transistors are reported as the most sensitive field effect transistor-based terahertz detectors. The advantage of HEMT is high electron mobility (up to 1500 cm^2/Vs) and the disadvantage is the presence of passive ungated regions which introduce additional series impedance contributing to the loss of high-frequency signal. The advantage of nMOS is the absence of ungated regions and the disadvantage is low electron mobility (about 250 cm^2/Vs) due to high acceptor density (about 2e18 cm^{-3}) in the channel.

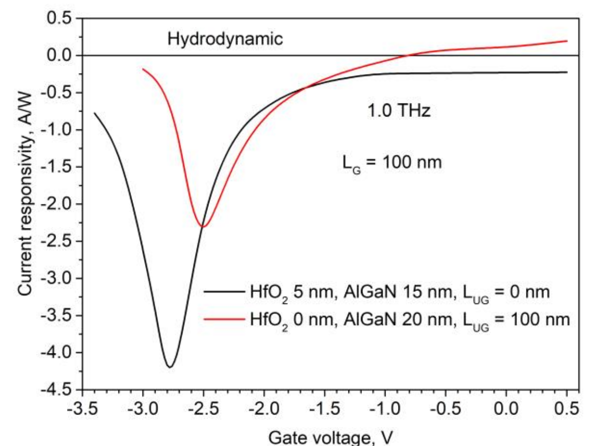

Fig. 1 Current responsivity of the HEMT without and with ungated regions L_{UG} and gate length L_G.

Here, we propose the HEMT-based THz detector with 5 nm HfO_2 dielectric between the gate electrode and the AlGaN layer, which allows to separate the gate from the source and drain terminals without involving ungated regions.

For numerical calculations of detector characteristics, we have employed two-dimensional hydrodynamic modeling performed with Synopsys TCAD Sentaurus program package comprising Poisson's equation, continuity equation, current density equation and energy balance equation for electrons and holes. It accounts for the formation of spontaneous and piezoelectric polarization charges in GaN and AlGaN layers, as well as the dependence of carrier mobility on doping density and carrier temperature.

The comparison of current responsivity of the HEMT with and without ungated regions and the gate length L_G = 100 nm is shown in Fig. 1. The results clearly indicate that the presence of ungated regions with the length L_{UG} = 100 nm reduces the maximum of the current responsivity at 1 THz by about 2 times. The minimum NEP at 1 THz is about 3 times lower in the HEMT without ungated regions.

REFERENCES

[1] M. Bauer at al; IEEE Transactions on Terahertz Science and Technology **9,** 430 (2019).
[2] J. Sun at al; Applied Physics Letters **116**, 161109 (2020).
[3] K. Ikamas at al; IEEE Electron Device Letters **39**, 1413 (2018).

Enhanced sensitivity AlGaN/GaN HEMT terahertz detector without ungated regions

Juozas Vyšniauskas[1], Kęstutis Ikamas[1,2], Alvydas Lisauskas[1,3]

[1] *Institute of Applied Electrodynamics and Telecommunications, Vilnius University, Vilnius, Lithuania*

[2] *Research Group on Logistics and Defense Technology Management, Military Academy of Lithuania, Vilnius, Lithuania*

[3] *CENTERA Labs, Institute of High Pressure Physics PAS, Warsaw, Poland*

Introduction

AlGaN/GaN HEMTs [1,2] and nMOS [3] transistors are reported as the most sensitive field effect transistor-based terahertz detectors. The advantage of HEMT is high electron mobility (up to 1500 cm^2/Vs) and the disadvantage is the presence of passive ungated regions which introduce additional series impedance contributing to the loss of high-frequency signal. The advantage of nMOS is the absence of ungated regions and the disadvantage is low electron mobility (about 250 cm^2/Vs) due to high acceptor density (about 2e18 cm^{-3}) in the channel. Here, we propose the HEMT-based THz detector with 5 nm HfO_2 dielectric between the gate electrode and the AlGaN layer, which allows to separate the gate from the source and drain terminals without involving ungated regions.

HEMT model

For numerical calculations of detector characteristics, we have employed two-dimensional hydrodynamic modeling performed with Synopsys TCAD Sentaurus program package comprising Poisson's equation, continuity equation, current density equation and energy balance equation for electrons and holes. It accounts for the formation of spontaneous and piezoelectric polarization charges in GaN and AlGaN layers, as well as the dependence of carrier mobility on doping density and carrier temperature.

HEMT structures

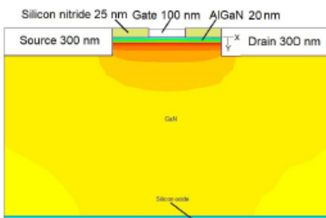

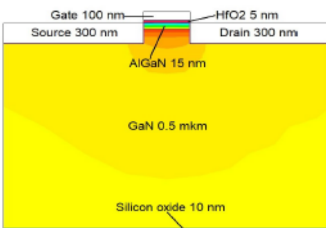

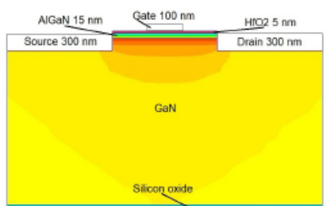

Static characteristics

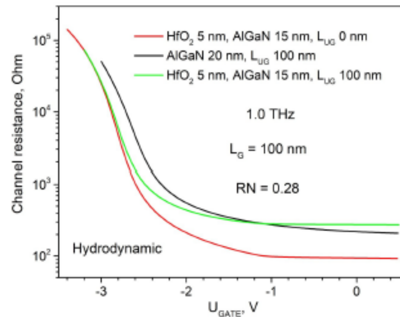

Current responsivity at 1.0 THz

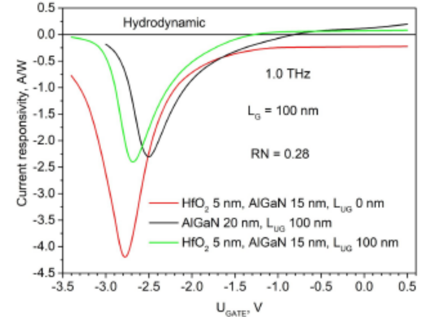

Current responsivity at 0.01 THz

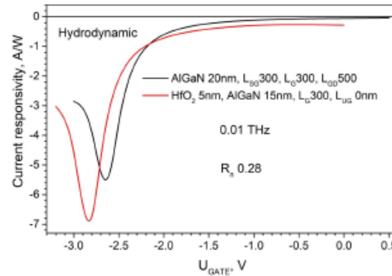

Noise equivalent power at 1.0 THz

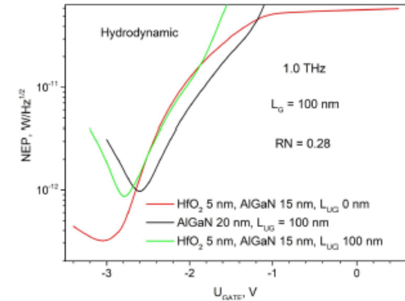

Real part of HEMT impedance at 1.0 THz

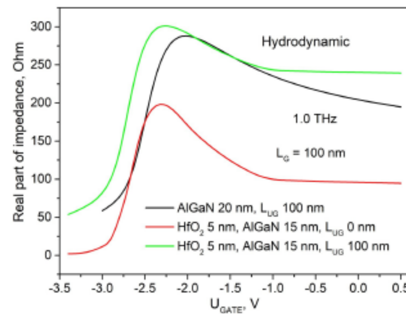

Current rsponsivity of the HEMT with various gate length L_G

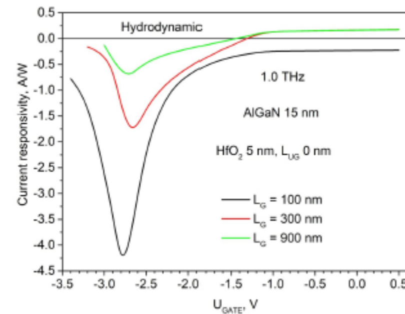

Imaginary part of HEMT impedance at 1.0 THz

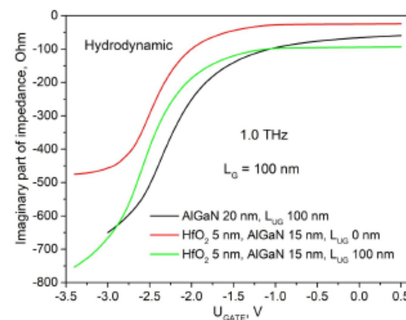

Conclusions

1. The results clearly indicate that the presence of ungated regions with the length L_{UG} = 100 nm reduces the maximum of the current responsivity at 1 THz by about 2 times.
2. The minimum NEP at 1.0 THz is about 3 times lower in the HEMT without ungated regions.
3. The change of detected current sign at high gate voltage (-1.0 +0.5 V) depends on gated and ungated regions length.
4. HEMT with HfO_2 dielectric and with ungated regions show almost the same current responsivity and NEP results as the HEMT without dielectric.

References

[1] M. Bauer at al; IEEE Transactions on Terahertz Science and Technology **9**, 430 (2019).

[2] J. Sun at al; Applied Physics Letters **116**, 161109 (2020).

[3] K. Ikamas at al; IEEE Electron Device Letters **39**, 1413 (2018).

P17

Performance of Titanium-based Microbolometers for Monitoring of Spatial Beam Profile in Terahertz Time-Domain Systems

Liang Qi[1], Linas Minkevičius[1], Andrzej Urbanowicz[1], Andrej Švigelj[2], Janez Trontelj[2] Domas Jokubauskis[1] and Gintaras Valušis[1]

[1] *Center for Physical Sciences and Technology, Saulėtekio Ave. 3, LT-10257 Vilnius, Lithuania*
[2] *Laboratory for Microelectronics, Faculty of Electrical Engineering, University of Ljubljana, Tržaška 25, 1000 Ljubljana, Slovenia*
Email: liang.qi@ftmc.lt

Spatial mode profile and its control in terahertz (THz) imaging and spectroscopic systems is one of the most important constituents to enable high measurement data quality. Moreover, convenience in use and abilities for precise optical alignment without additional optical components would be attractive advantage in practical implementation of the systems.

In this communication, convenient and easy-to-use both resonant and broadband antenna coupled ultrasensitive titanium-based microbolometers are demonstrated for fine adjustment and control spatial mode profiles in THz time-domain systems. The devices were found well-suited for implementation for medical imaging aims [1].

Three types of microbolometers [2] with the narrow band dipole antenna of 0.3 THz, 0.7 THz and a log-periodic broadband antenna [3] were explored. Femtosecond laser with a wavelength of 780nm, pulse duration of 90 fs and output power of 150 mW at 80 MHz pulse repetition rate was used for optical excitation. The photoconductive antennas were fabricated from LT-GaAs to offer wide emission spectrum from 0 to 5 THz. Figure 1 presents spatial mode profile in a focus plane and beam evolution illustrated via fourteen cross sections in interval of 10 mm. As one can see, all three different antennas-coupled microbolometers display well features of beam profiles without usage of additional focusing optical components.

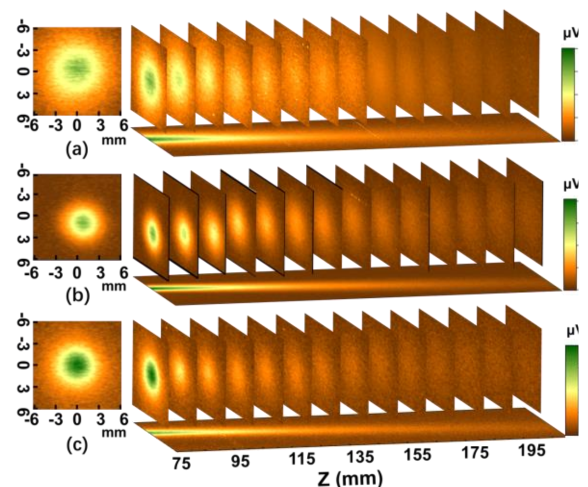

Fig. 1 Beam profiles in focus plane and along the beam propagation recorded.
(a) by 0.3 THz antenna-coupled microbolometer,
(b) by 0.7 THz antenna-coupled microbolometer,
(c) by broadband antenna-coupled

Microbolometer design features and ability to resolve polarization properties will be presented and discussed as well.

REFERENCES

[1] I. Kašalynas, R. Venckevičius, L. Minkevičius, A. Sešek, F. Wahaia, V. Tamošiūnas, B. Voisiat, D. Seliuta, G. Valušis, A. Švigelj, and J. Trontelj, Sensors 16, (2016,) 432.

[2] J. Trontelj, G. Valušis, R. Venckevičius, I. Kašalynas, A. Sešek and A. Švigelj; *Terahertz Emit. Receiv. Appl. V* **9199**(2014) pp. 91990K.

[3] L. Minkevičius, L. Qi, A. Siemion, D. Jokubauskis, A. Sešek, A. Švigelj, J. Trontelj, D. Seliuta, I. Kašalynas and G. Valušis*; Appl. Sci.***10**(2020) pp.3400.

CENTER FOR PHYSICAL SCIENCES AND TECHNOLOGY

Performance of Titanium-based Microbolometers for Monitoring of Spatial Beam Profile in Terahertz Time-Domain Systems

Liang Qi[1], Linas Minkevičius[1], Andrzej Urbanowicz[1], Andrej Švigelj[2], Janez Trontelj[2], Domas Jokubauskis[1] and Gintaras Valušis[1]

1 Center for Physical Sciences and Technology, Saulėtekio Ave. 3, LT-10257 Vilnius, Lithuania

2 Laboratory for Microelectronics, Faculty of Electrical Engineering, University of Ljubljana, Tržaška 25, 1000 Ljubljana, Slovenia

Email: liang.qi@ftmc.lt

Spatial mode profile and its control in terahertz (THz) imaging and spectroscopic systems is one of the most important constituents to enable high data quality. Moreover, convenience in use and abilities for precise optical alignment without additional optical components would be attractive advantage in practical implementation of the systems.

In this communication, convenient and easy-to-use both resonant and broadband antenna coupled ultrasensitive titanium-based microbolometers are demonstrated for fine adjustment and control spatial mode profiles in THz time-domain systems. The devices were found well-suited for implementation for medical imaging aims [1].

Three types of microbolometers [2] with the narrow band dipole antenna of 0.3 THz, 0.7 THz and a log-periodic broadband antenna [3] were explored. Femtosecond laser with a wavelength of 780nm, pulse duration of 90 fs and output power of 150mW at 80 MHz pulse repetition rate was used for optical excitation. The photoconductive antennas made from LT-GaAs offers a wide transmission spectrum from 0 to 5THz in the experiment.

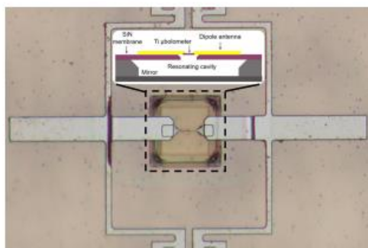

Fig. 1. The scheme of THz titanium-based microbolometer with dipole antenna.

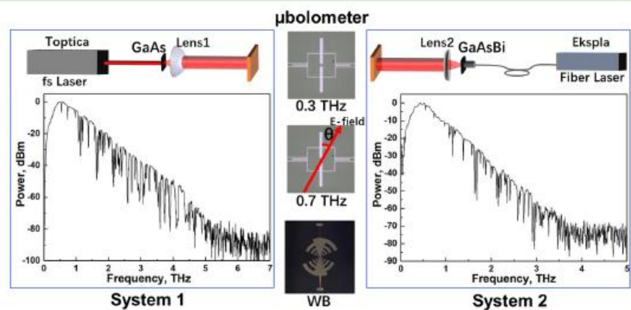

Fig. 2. The schematic diagrams and parameters of TDS setups in **System 1** and **System 2**, photos of three microbolometers. The angle θ is defined on the photo of 0.7THz detector.

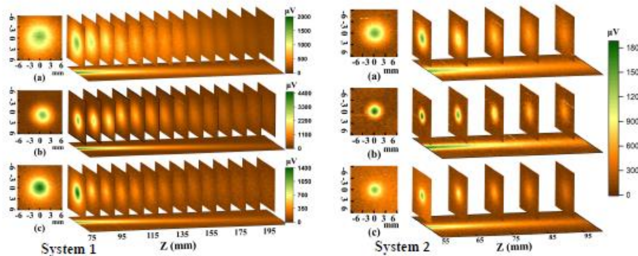

Fig. 3. The beam profile evolution of System 1 and System 2, separately recovered by three different detectors. (a) recorded by 0.3THz detector, (b) recorded by 0.7THz detector, (c) recorded by broadband detector.

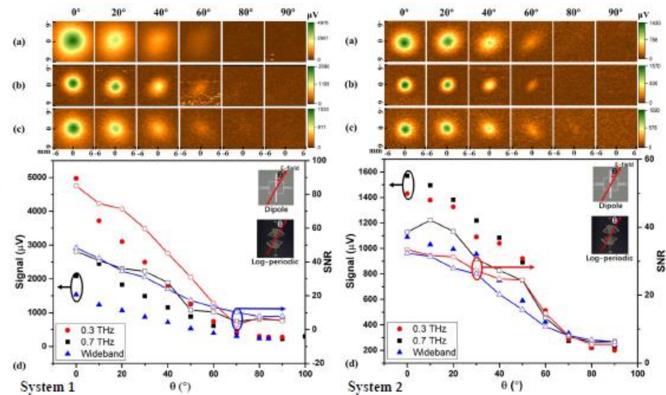

Fig. 4. The evolution of beam profile, peak power and SNR with different polarization in System 1 and System 2.

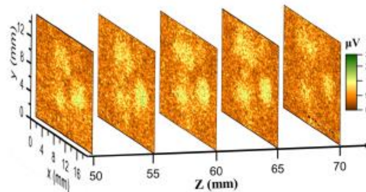

Fig. 5. The spatial characteristic of System 1 without Lens1 along z- axis detected by 0.7 THz microbolometer.

CONCLUSIONS

Spatial mode profiles and polarization-resolved mode structures are recorded by titanium-based microbolometers in two THz time-domain systems. It is found that three microbolometers reproduce well the spatial mode profile of time-domain spectrometer. Polarization-sensitive mode control possibilities are also examined in details.

REFERENCES

[1] I. Kašalynas, R. Venckevičius, L. Minkevičius, A. Sešek, F. Wahaia, V. Tamošiūnas, B. Voisiat, D. Seliuta, G. Valušis, A. Švigelj, and J. Trontelj, Sensors 16, (2016) 432.

[2] J. Trontelj, G. Valušis, R. Venckevičius, I. Kašalynas, A. Sešek and A. Švigelj; Terahertz Emit. Receiv. Appl. V 9199(2014) pp. 91990K.

[3] L. Minkevičius, L. Qi, A. Siemion, D. Jokubauskis, A. Sešek, A. Švigelj, J. Trontelj, D. Seliuta, I. Kašalynas and G. Valušis; Appl. Sci.10(2020) pp.3400.

P18

Laser system for pumping THz and coherent X-ray sources of secondary radiation

Paulius Mackonis, Augustinas Petrulenas, Vytenis Girdauskas, Aleksej Rodin

Solid State Laser laboratory, Center for Physical Sciences and Technology
Savanoriu 231, LT-02300 Vilnius, Lithuania.
Email: paulius.mackonis@ftmc.lt

The progress of natural science as well as a paradigm shift in the economy became inconceivable without the implementation of superstrong electromagnetic fields. However, the commissioning of high-intensity lasers within ELI framework is more a form of budget redistribution than a solution, because the cumbersome and time-consuming laser architecture is doomed to downtime, while scientists and technologists remain on the waiting list.

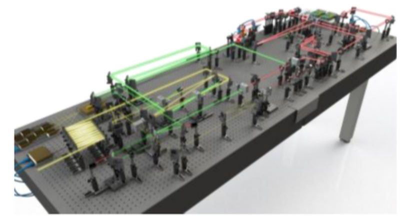

Fig. 1 Layout of high peak power laser system at FTMC.

On the contrary, a cost-effective laser system built on two 1.5 m^2 breadboards (Fig. 1) by the efforts of one graduate and 1-2 students provides a choice of output pulses: >20 mJ, 1 ps with M^2<1.1 at 1030 nm [1] or >2 mJ, <20 fs with M^2~1.2 at 790 nm [2], as well as probe supercontinuum (SC) at 600 – 2500 nm [3]. Using more pump diodes or increasing their power allows to further scale the peak power over 1 TW. Laser is based on easily reproducible modules: fiber laser front-end, two-stage double-pass Yb:YAG chirped pulse amplifier (CPA), grating compressor, SC generation, two cascades of second harmonic generation (SHG), three stages of noncollinear optical parametric chirped pulse amplifier (OPCPA), and chirped mirrors compressor. Using the same pump source for OPCPA and SC provides inherent synchronization and greatly simplifies the scheme. The energy conversion efficiency was improved due to the reuse of pump pulses depleted in SHG [1], and the maintenance of a wide OPCPA bandwidth due to their temporal shaping [2]. The solutions developed during the project were implemented at Ekspla Ltd in technological and scientific lasers. The obtained ultrashort high-energy laser pulses are ideally suited for the generation of highly efficient THz [4] and coherent X-ray radiation.

The demonstration of a multi-octave SC in the range up to 2500 nm [3] allows the use of a similar OPCPA architecture to develop a sub-TW laser in the 2 μm spectral range for the high order harmonics generation or remote sensing of gases by filamentation. However, to eliminate the need for expensive periodically poled nonlinear crystals, we are developing an alternative concept for broadband Transient Stimulated Raman Chirped Pulse Amplification (TSRCPA).

Two of the co-authors are grateful to Eksma Ltd for providing student scholarships. This research was sponsored in part by the NATO SPS Programme under grant G5734.

REFERENCES

[1] P. Mackonis, A.M. Rodin; *Opt. Express* **28** (2020) pp.1261–1268.
[2] P. Mackonis, A.M. Rodin; *Opt. Express* **28** (2020) pp.12020–12027.
[3] P. Mackonis, A. Petrulenas, V. Girdauskas, A.M. Rodin; CLEO/Europe-2019, CA-P.43 MON.
[4] J.A.Fülöp, L. Pálfalvi, S. Klingebiel, G. Almási, F. Krausz, S. Karsch, J. Hebling; *Opt. Lett* **37** (2012) pp.557–559.

Laser system for pumping THz and coherent X-ray sources of secondary radiation

CENTER FOR PHYSICAL SCIENCES AND TECHNOLOGY

Paulius Mackonis, Augustinas Petrulėnas, Vytenis Girdauskas and Aleksej Rodin

Solid State Laser Laboratory, Center for Physical Sciences and Technology, Savanoriu 231, LT-02300 Vilnius, Lithuania.

We demonstrate compact TW-class VIS-NIR wavelength range Noncollinear Optical Parametrical Chirped Pulse Amplifier (NOPCPA) with an almost lossless spectral bandwidth due to the formation of "M"-shaped picosecond pumping pulses after the SHG-conversion. Moreover, the reuse of depleted pulses after the first SHG cascade increases the overall efficiency.

Compact TW-class VIS – NIR wavelength range laser system

The progress of natural science as well as a paradigm shift in the economy became inconceivable without the implementation of superstrong electromagnetic fields. However, the commissioning of high-intensity lasers within ELI framework is more a form of budget redistribution than a solution, because the cumbersome and time-consuming laser architecture is doomed to downtime, while scientists and technologists remain on the waiting list.

Ultrashort, high energy, tunable wavelength laser pulses are in demand for a wide range of applications in ultrafast and strong field physics. Of great interest is their use for driving secondary radiation sources, such as the generation of THz and attosecond X-ray pulses. In addition, filamentation of ultrahigh intensity laser pulses in air opens up unprecedented opportunities for remote gas sensing. Recent studies have shown that an increase in the wavelength of the driving laser radiation makes it possible to generate higher photon energy attosecond X-ray pulses [1], as well as improve the efficiency of THz generation [2]. Furthermore, filamentation in air also benefits from longer driving wavelength because the wavelength scaling of the critical power of self-focusing allows more energy to be contained in a single filament.

In this work we present a cost-effective laser system that provides a choice of output pulses: >20 mJ, 1.2 ps with M^2<1.1 at 1030 nm [3] or >2 mJ, <20 fs with M^2~1.2 at 790 nm [4], as well as probe supercontinuum (SC) at 500 – 2400 nm [5]. A multi-octave SC in the range up to 2400 nm allows the use of a similar OPCPA architecture to develop a sub-TW laser in the 2 µm spectral range for the high order harmonics generation or remote sensing of gases by filamentation. However, to eliminate the need for expensive periodically poled nonlinear crystals, we are developing an alternative concept for broadband Transient Stimulated Raman Chirped Pulse Amplification (TSRCPA) [6].

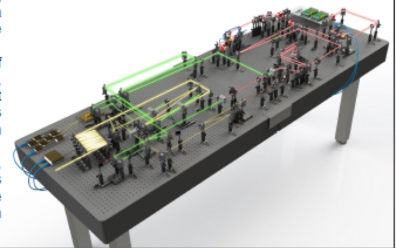

PUMPING SOURCE
Yb:YAG CPA and Pulse Compresssor

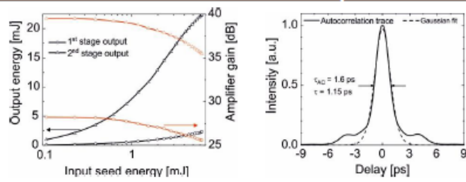

Fig. 1 The output energy (black) and gain (red) of CPA versus the seed energy (left) and autocorrelation trace of amplified pulses after compression (right).

- ✓ Amplified pulses with a total gain of ~3.500, an output energy of up to **22 mJ**.
- ✓ Pulses energy stability better than 1 %.
- ✓ Pulse compression up to ~**1.2 ps**.
- ✓ Excellent beam quality ***M²* < 1.1**.

OPCPA SEED AND PUMP PULSES
Supercontinuum and Second Harmonic Generation

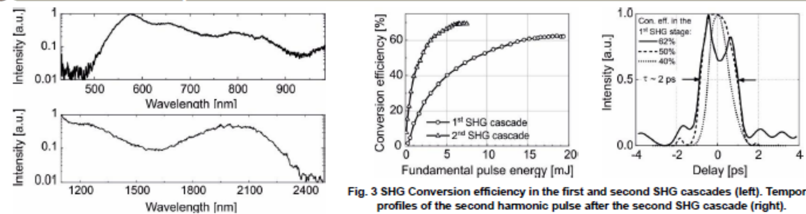

Fig. 2 Supercontinuum spectra in 15 mm YAG crystal.

- ✓ Stable single-filament supercontinnum spanning **~500 nm to ~2400 nm** in YAG rod of **15 mm** length.
- ✓ SC shows an energy stability exceeding the pumping laser.

Fig. 3 SHG Conversion efficiency in the first and second SHG cascades (left). Temporal profiles of the second harmonic pulse after the second SHG cascade (right).

- ✓ Compressed pulses converted to the second harmonics in LBO and BBO crystals with **62%** and **70%** efficiency: overall ~85% efficiently.
- ✓ After the first SHG cascade: **12 mJ** output energy at 515nm and ~ **1.2 ps** pulsewidth.
- ✓ Further frequency doubling of depleted pulses in BBO provides "M"-shaped pump pulses at 515 nm with **5 mJ** output energy and ~**2 ps** pulsewidth.

IN PROGRESS: compact femtosecond VIS – NIR – SWIR laser system

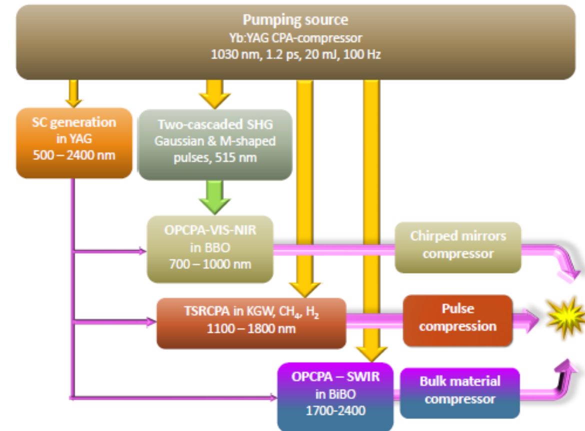

Fig. 4 Layout of a compact femtosecond VIS – NIR – SWIR laser system.

OPCPA – VIS-NIR

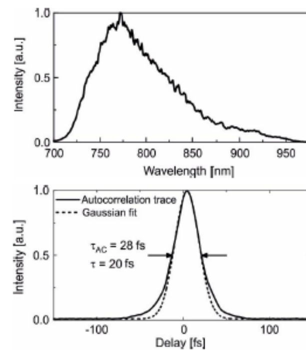

Fig. 5 Spectrum of amplified pulses after three OPCPA stage (top) and autocorrelation trace after comression (bottom).

- ✓ The pump-to-signal efficiency of ~20% and the pulse energy of **~2.1 mJ** after the third OPCPA stage was reached.
- ✓ Amplified spectrum corresponding to Fourier-limited pulsewidth of **~8.6 fs**.
- ✓ Pulse compression up to **20 fs**.
- ✓ Beam quality ***M²* < 1.25.**

Transient Stimulated Raman Chirped Pulse Amplification

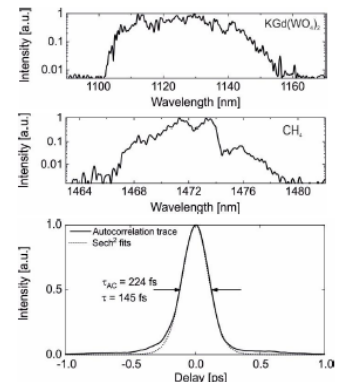

Fig. 6 TSRCPA output spectra in $KGd(WO_4)_2$ (top) and CH_4 (middle). Autocorrelation trace of compressed pulse after TSRCPA in $KGd(WO_4)_2$ crystal (bottom).

- ✓ Frequency shift during amplification of chirped SC pulses in a stimulated Raman amplifier based on solids or gases.
- ✓ Possible pulse compression.

Conclutions & future work

- Recycling of depleted pulses at fundamental wavelength after the first SHG stage improves the overall harmonics conversion efficiency up to 85%.
- The use of "M"-shaped pump pulses made it possible to maintain a wide spectral bandwidth of amplified pulses in OPCPA stages with a high gain, while Gaussian pump pulses provided efficient energy extraction at the last stage.
- Laser system was built with an output energy of 2.1 mJ at a repetition rate of 100 Hz with support of a spectral bandwidth corresponding to a transform-limited pulsewidth of 8.6 fs. Pulse compression up to 20 fs at 790 nm was demonstrated.
- Transient Stimulated Raman Chirped Pulse Amplification shows a potential as an alternative to OPCPA or a complimentary method for developing intense femtosecond laser pulse source with frequency conversion.

Acknowledgment

- Two of the co-authors are grateful to Eksma Ltd for providing student scholarships.
- This research was sponsored in part by the NATO SPS Programme under grant G5734.
- The solutions developed during the project were implemented at Ekspla Ltd in technological and scientific lasers.

References

[1] M.C.Chen, P.Arpin, T.Popmintchev, M.Gerrity, B.Zhang, M.Seaberg, D.Popmintchev, M.M.Murnane and H.C.Kapteyn, "Bright, Coherent, Ultrafast Soft X-Ray Harmonics Spanning the Water Window from a Tabletop Light Source," Phys. Rev. Lett. 105, 173901 (2010).
[2] M.Clerici, M.Peccianti, B.E.Schmidt, L.Caspani, M.Shalaby, M.Giguere, A.Lotti, A.Couairon, F.Legare, T.Ozaki, D.Faccio and R.Morandotti, "Wavelength Scaling of Terahertz Generation by Gas Ionization," Phys. Rev. Lett. 110, 253901 (2013).
[3] P.Mackonis, A.Rodin, "Laser with 1.2 ps, 20 mJ pulses at 100 Hz based on CPA with a low doping level Yb:YAG rods for seeding and pumping of OPCPA," Opt. Express 28(2), 1261-1268 (2020).
[4] P.Mackonis, A.Rodin, "OPCPA investigation with control over the temporal shape of 1.2 ps pump pulses," Opt. Express 28(8), 12020-12027 (2020).
[5] P.Mackonis, A.Petrulenas, V.Girdauskas, and A.M.Rodin, "Stable 1100 - 2400 nm supercontinuum in YAG with picosecond pumping for simplified OPCPA," in 2019 Conference on Lasers and Electro-Optics Europe and European Quantum Electronics Conference, OSA Technical Digest (Optical Society of America, 2019), paper ca_p_43.
[6] P.Mackonis, A.Rodin, A.Petrulenas, V.Girdauskas and A.Michailovas, "Two-stage transient stimulated Raman chirped pulse amplification in $KGd(WO_4)_2$ with compression to 145 fs," (to be published).

Author index

Name	Presentation	Page
Abate Antonio	P9	67
Adomavičius Ramūnas	O19	42
Agafonov Vladimir	O12	32
Aleksiejūnas Ramūnas	Inv2	16
Alexeeva Natalia V.	O2, O21	20, 44
Alekseev Kirill N.	O21	44
Alkauskas Audrius	O8	27
Ardaravičius Linas	P4	58
Ašmontas Steponas	P2	54
Badokas Kazimieras	Inv6	28
Bakute Neringa	O23	46
Balagula Roman M.	O10, P5	30, 60
Banevičius Dovydas	Inv4	19
Bartosewicz B.	O4	22
Bičiūnas Andrius	O12	32
Bogucki A.	Inv8	34
Bożek Rafał	O1, Inv8	17, 34
Bukauskas Virginijus	O12	32
But Dmytro B.	O4, O13, O14, O16, O18, O20, P15	22, 35, 36, 38, 41, 43, 76
Butkutė Renata	O11, O12, O27, P1	31, 32, 50, 52
Buyanova Irina A.	O10	30
Chebotarev Valentin S.	O18	41
Canton Sophie E.	O26	49
Charkova Tatjana	P6	62
Chen Weimin M.	O10	30
Cherniadiev Aleksander	O16	38
Cywinski Grzegorz	O4, O9, O13, O20	22, 29, 35, 43
Čechavičius Bronislovas	O11, O12, P1	31, 32, 52

Čerškus Aurimas	P2	54
Čižas Vladislovas	O21	44
Demchenko Petr S.	O18	41
Devenson Jan	P3	56
Dietl T.	O9	29
Dodonova Jelena	P7	63
Driukas Simonas	P8	65
Dub M.	O13, O20	35, 43
Dudutienė Evelina	O11, O27	31, 50
Dvoretsky S. A.	O9, O14	29, 36
Firsov Dmitry A.	P5	60
Franckevičius Marius	P8, P9	65, 67
Gaidys Mantas	O19	42
Gavrilenko V. I.	O14	36
Gedvilas Mindaugas	O19	42
Gegevičius Rokas	P8, P9	65, 67
Girdauskas Vytenis	P18	82
Golubewa Lena	O3, P14	21, 74
Grabecki G.	O9, P15	29, 76
Gradauskas Jonas	P2	54
Grasza K.	P15	76
Gryglas-Borysiewicz Marta	O1	17
Grinys Tomas	Inv6	28
Grzeszczyk M.	Inv8	34
Gudaitis Rimantas	Inv3, P11	18, 70
Gulbinas Vidmantas	P8, P9	65, 67
Guobienė Asta	Inv3	18
Ikamas Kestutis	O16, P16	38, 78
Indrišiūnas Simonas	Inv1	15
Ishikawa Fumitaro	O10	30
Ivaškevičiūtė-Povilauskienė Rusnė	O2	20
Jankauskas Šarūnas	Inv3, P11	18, 70
Jansson Mattias	O10	30

Jasinskas Algirdas	O11, O12, O27, P1	31, 32, 50, 52
Jasiūnas Rokas	P8, P9	65, 67
Javadi Elham	O16	38
Javorskis Tomas	Inv4	19
Jočionis Lukas	O11, P1	31, 52
Jokubauskis Domas	Inv1, O2, O17, P17	15, 20, 39, 80
Jovaišaitė Justina	Inv4	19
Juršėnas Saulius	Inv4	19
Juscenko Viktorija	O25	48
Kadys Arūnas	Inv6	28
Kamarauskas Andrius	P13	73
Kamarauskas Mindaugas	O12	32
Kancleris Žilvinas Andrius	O2, P13	20, 73
Karpicz Renata	O3, P10, P14	21, 69, 74
Kašalynas Irmantas	Inv1, O7	15, 26
Kazakov A.	O9	29
Kazimierczuk T.	Inv8	34
Kazlauskas Karolis	Inv4	19
Khodzitsky Mikhail K.	O18	41
Kiauleikis Mykolas	Inv11	40
Kiprijanovič Oleg	P4	58
Knap Wojciech	O4, O9, O13, O14, O18, O20, P15	22, 29, 35, 36, 41, 43, 76
Kolenda Marek	Inv6	28
Komorowski Paweł	O15	37
Konishi Kuniaki	O22	45
Korotyeyev Vadym	O7	26
Kossacki P.	Inv8	34
Krajewska Aleksandra	O4, O13, O18	22, 35, 41
Kravcov Oleg	Inv2	16
Kreiza Gediminas	Inv4	19
Kret Sławomir	O1, Inv8	17, 34
Krishtopenko S. S.	O9	29
Krotkus Arūnas	O6, O19	25, 42

Kucharek J.	Inv8	34
Kulahava Tatsiana	O3	21
Kuritzky Leah	Inv2	16
Kuzhir Polina	O3, P14	21, 74
Lynsky Cheyenne	Inv2	16
Lioubtchenko Dmitri V.	O4, O18	22, 41
Liszewska M.	O4	22
Lisauskas Alvydas	O16, O18, P16	38, 41, 78
Lukaševičiūtė Rugilė	P10	69
Lukša Algimantas	O12	32
Łusakowski J.	O14, O20	36, 43
Maciaszek Marek	O8	27
Mackoit-Sinkevičienė Mažena	O8	27
Mackonis Paulius	P18	82
Majewicz M.	O9	29
Maleckaitė Karolina	P7	63
Malinauskas Tadas	Inv6	28
Masalskyi Oleksandr	P2	54
Matulaitienė Ieva	O2, P14	20, 74
Melo Wanessa	O25	48
Meškinis Šarūnas	Inv3, P11	18, 70
Mickevičius Jūras	Inv6	28
Mikhailov N. N.	O9, O14	29, 36
Minkevičius Linas	Inv1, O2, O17, Inv11, P17	15, 20, 39, 40, 80
Nakamura Shuji	Inv2	16
Nargelas Saulius	Inv2	16
Navakauskas Edvinas	O24	47
Nefedova Irina	O18	41
Nefedov Igor S.	O18	41
Nevinskas Ignas	O6	25
Niaura Gediminas	P6, P12	62, 71
Nogajewski K.	Inv8	34
Nomeika Kazimieras	Inv2	16

Norkus Ričardas	O6, P3	25, 56
Oberhammer Joachim	O18	41
Obraztsov Petr	O22	45
Ogorzałek Zuzanna	O1	17
Orentas Edvinas	Inv4	19
Oreszczuk K.	Inv8	34
Orlov Sergej	Inv1	15
Pacuski Wojciech	O1, Inv8	17, 34
Pashnev Daniil	O7	26
Pasternak I.	O13	35
Pavilonis Dainius	Inv7	33
Pavlov K.	O4	22
Petrulėnas Augustinas	P18	82
Phung Nga	P9	67
Piramidowicz Ryszard	O15	37
Plaušinaitienė Valentina	Inv7	33
Poceviciute Ernesta	O23	46
Połczyńska K.E.	Inv8	34
Ponseca, Jr. Carlito S.	Inv5	23
Potemski M.	Inv8	34
Prystawko P.	O20	43
Przewłoka Aleksandra	O13, O18	35, 41
Pudžaitis Vaidas	P12	71
Pūkienė Simona	O11, O12, P1	31, 32, 52
Qi Liang	O17, P17	39, 80
Račiukaitis Gediminas	Inv1, O19	15, 42
Razinkovas Lukas	O8	27
Rehman Adil	O4	22
Rodek R.	Inv8	34
Rodin Aleksej	P18	82
Rudokas Vakaris	Inv7	33
Rumyantsev S.	O4, O13, O20, P15	22, 35, 43, 76
Sadowski Janusz	O1, Inv8	17, 34

Sadzevičienė Rita	P6	62
Sai Pavlo	O13, O20	35, 43
Sakowicz M.	O13, O20	35, 43
Sarkisyan Hayk A.	P5	60
Seliuta Dalius	O2, O21, P13	20, 44, 73
Selskis Algirdas	P14	74
Seredyński Bartłomiej	O1, Inv8	17, 34
Šetkus Arūnas	O12	32
Shuba Mikhail	O3	21
Siemion Agnieszka	O15, O17	37, 39
Šilėnas Aldis	P2	54
Šlekas Gediminas	P13	73
Skapas Martynas	Inv6	28
Smirnov Serguei	O4, O18	22, 41
Sofronov Anton N.	P5	60
Speck James S.	Inv2	16
Stanionytė Sandra	Inv6, O27, P3	28, 50, 56
Stankevič Voitech	Inv7	33
Stašys Karolis	P3	56
Stehr Jan E.	O10	30
Stelmaszczyk Kamil	O18	41
Stirke Arunas	O23, O25	46, 48
Stonio B.	O4	22
Strazdaitė Simona	O24	47
Subačius Liudvikas	O21	44
Surma Mateusz	O15	37
Sužiedėlis Algirdas	P2	54
Švigelj Andrej	P17	80
Svirko Yuri	O22	45
Szoła Maria	O14, O20	36, 43
Talaikis Martynas	P12	71
Tamošiūnas Vincas	Inv1, Inv11	15, 40
Taniguchi T.	Inv8	34

Teppe F.	O9	29
Trontelj Janez	P17	80
Tumkevičius Sigitas	P7	63
Tutkus Marijonas	O23	46
Urbanowicz Andrzej	O7, P17	26, 80
Vaičikauskas Viktoras	P2	54
Vaitkevičius Vytenis	Inv4	19
Valušis Gintaras	Inv1, O2, O17, Inv11, O21, P17	15, 20, 39, 40, 44, 80
Vasiliauskas Andrius	Inv3, P11	18, 70
Vyšniauskas Aurimas	P7	63
Vyšniauskas Juozas	P16	78
Watanabe K.	Inv8	34
Weisbuch Claude	Inv2	16
Yahniuk Ivan	O9, O14, P15	29, 36, 76
Yavorskiy D.	O14, O20, P15	36, 43, 76
Yukimune Mitsuki	O10	30
Žalys Ovidijus	P2	54
Zdaniauskienė Agnė	P6	62
Zelioli Andrea	O11	31
Zheng Kaibo	O5	24
Žičkienė Ieva	O19	42
Zykov Dmitry V.	O18	41
Žurauskienė Nerija	Inv7	33